Methods and Metrics to Characterize Body Surface Activation in Cardiac Resynchronization Therapy Patients

A Thesis
SUBMITTED TO THE FACULTY OF THE
UNIVERSITY OF MINNESOTA
BY

Antonia Eugenia Curtin

IN PARTIAL FULFULLMENT OF THE REQUIREMENTS
FOR THE DEGREE OF
DOCTOR OF PHILOSOPHY

Advisors: Alan J. Bank, MD and Theoden I. Netoff, PhD

May 2018

Acknowledgements

First, I thank my advisors Dr. Alan Bank and Dr. Theoden Netoff, from whose experience and guidance I have benefited throughout my studies. Dr. Bank, you have always supported my research and given me the chance to argue a point. You have also given me many opportunities to grow professionally, and I especially appreciate your flexibility in allowing me to intern elsewhere for a summer. That internship produced an exciting job opportunity that I would not otherwise have, and I am grateful to you for that. Dr. Netoff, your enthusiasm for out-of-the-box thinking has changed how I approach seemingly intractable problems and made me more eager to pursue creative solutions. I appreciate your willingness to meet with me, even though I was not in your main laboratory, and I will certainly miss our discussions and their frequent hilarious tangents.

I thank my committee members Dr. Paul Iaizzo and Dr. Arthur Erdman for all of their advice, support, and contributions to this thesis. I also thank Dr. Kevin Burns for persistently and patiently providing thoughtful feedback on my countless questions over the past few years.

I thank the Biomedical Engineering department and, in particular, Dr. Victor Barocas and Rachel Jorgenson for their support throughout my PhD. I also thank the United Heart and Vascular Clinic research department and clinical staff, especially Terri Proulx, Ryan Gage, Trina Lassi, Lisa Boben, Matt Klimek, and Kaye Lewis. I thank Drs. Peterson, Vatterott, Bagwe, and Underwood for routinely making time to answer my electrophysiology questions. I thank Drs. Bajpai and Ray for letting me use their office and their equipment for the MRI portion of this thesis. Finally, I thank Medtronic scientists Jeff

Gillberg, Subham Ghosh, Ruth Nicholson Klepfer, and Joshua Blauer for their support of this work and their thoughtful feedback.

Friends and family have supported me throughout my studies. My special thanks go to Kelsey Pflepsen (and all of the Pflepsens) for making me a part of her Minnesota family and being the best of friends; to Judy Schaefer for countless care packages, cards, and love; and to Kerianne Steucke and Laura Zitella Verbick for friendship and advice on my dissertation. I thank all of the Drs. Curtin who have encouraged me along the way: my aunt, Elizabeth Curtin, and my sister, Alexandra Curtin, who have inspired me to try to be as successful as they are, and my parents, Elaine and Jeremy Curtin, whose support and love have been constant and without limit. Last, but by no means least, I thank Jeremy Schaefer for his love, patient kindness, and endless support. With you, I have everything I ever wanted.

Finally, I gratefully acknowledge the funding sources that made this work possible. I thank the United Hospital Foundation for grant support and for supporting my travel to scientific conferences. I also thank the Medtronic external research program for their funding support.

Dedication

This thesis is dedicated to my mother. For every phone call, for every card, for every read-through, for every flight to Minneapolis, and for every intangible, wonderful thing that you do so selflessly and lovingly for me. You have a heart full of grace and a soul full of love. Congratulations on completing your fourth and final dissertation.

Abstract

Cardiac resynchronization therapy (CRT) is intended to ameliorate intra- and interventricular electrical dyssynchrony and improve systolic function in heart failure patients. In spite of the success of CRT in many multicenter studies, 30% of CRT patients fail to respond to the therapy. Lack of CRT patient response is linked to the limited sensitivity and spatial resolution of the 12-lead ECG, the current clinical standard for evaluating CRT candidates and patients. A promising alternative to the 12-lead ECG is body surface activation mapping using multichannel electrocardiograms (MECGs). However, in order to be a viable solution to CRT non-response, body surface activation metrics must be not only better correlated with patient CRT outcomes than current 12-lead ECG measures but also readily measurable in a real-time clinical setting. This thesis evaluated an investigational body surface mapping system against these criteria (1) by developing automated QRS complex analysis algorithms for MECGs, (2) by evaluating the reproducibility of body surface activation metrics, and (3) by developing new metrics to predict patient CRT outcomes. This work also explored the use of body surface activation maps to characterize electrical sequences in CRT patients and evaluated the effects of patient geometry on the predictive value of body surface activation metrics.

Table of Contents

List of Figures

List of Tables

List of Abbreviations

AP = anterior-posterior

AP_{REL} = relative AP position

AVD = atrioventricular delay

aCRT = AdaptivCRT

ACE/ARB = angiotensin-converting enzyme inhibitor/angiotensin II receptor blocker

APU = anterior-posterior uncoupling

AUC = area under the curve

AUC_B = Body surface activation area under curve

BSAd = body surface activation duration

BiV = biventricular

BMI = body mass index

CW = chest width

CD = chest depth

CV = coefficient of variation

CRT = cardiac resynchronization therapy

CRT_{CE} = CRT candidate evaluation

CRT_{SS} = CRT setting selection

ECG = electrocardiogram

ECGi = electrocardiographic imaging

EF = ejection fraction

GUI = graphical user interface

HF = heart failure

HRV = heart rate variability

IRB = institutional review board

ICM = ischemic cardiomyopathy

IVCD = nonspecific intraventricular conduction delay

IAED = inter-activation event distance

LVTR = LVEDV thoracic ratio

LBBB = left bundle branch block

LVESV = left ventricular end-systolic volume

LVESD = left ventricular end-diastolic volume

LV = left ventricle

LTAT = left-thorax activation time

MRI = magnetic resonance imaging/images

ML = medial-lateral

ML_{REL} = relative ML position

MECG = multichannel electrocardiogram

NICM = non-ischemic cardiomyopathy

NYHA = New York Heart Association

ΔNCRT = change in (metric value) from native conduction to CRT

OM = outlier morphology

PLSR = partial least squares regression

PM = predominant morphology

PVC = premature ventricular contraction

PP = pseudo-physiologic

QRSd = QRS complex duration

RBBB = right bundle branch block

RV = right ventricle

SDAT = standard deviation of activation times

$\theta_{LV,F}$ = frontal plane LV orientation

$\theta_{LV,T}$ = transverse plane LV orientation

UHVC = United Heart and Vascular Clinic

VCG = vectorcardiography

VIP = variable importance in PLSR

1 Introduction

1.1 Electrical dyssynchrony in heart failure

Heart failure (HF) affects approximately 6 million people and accounts for 10% of all deaths annually in the United States [6]. In 25% to 30% of the HF population, the disease is associated with dyssynchronous cardiac activation (i.e., depolarization), caused by an ischemic event or the progression of other cardiovascular diseases that cause cardiac remodeling [7-14]. The electrical dyssynchrony results in poorly coordinated left ventricular (LV) and right ventricular (RV) contraction during systole, inefficient ejection of blood from the ventricles, a further decrease in functional capacity, and worsening HF [8, 15].

Abnormal ventricular activation may present as left bundle branch block (LBBB), right bundle branch block (RBBB), or a nonspecific intraventricular conduction delay (IVCD). In LBBB, the most common of these pathologies [16], the total time for electrical activation is increased because conduction through the high-velocity fibers of the LV is pathologically prevented, and conduction proceeds slowly from cell to cell [7, 13]. The clinical and functional effects of LBBB are also more severe than those associated with RBBB or IVCD because of the dominant contribution of the LV to cardiac pump function [17, 18]. Figure 1-1 illustrates the paths of normal and LBBB conduction and the effects of LBBB on LV contraction during systole, as measured by echocardiographic speckle-tracking strain (adapted with permission from Cingolani et al. [19] and Gorcsan et al. [20]).

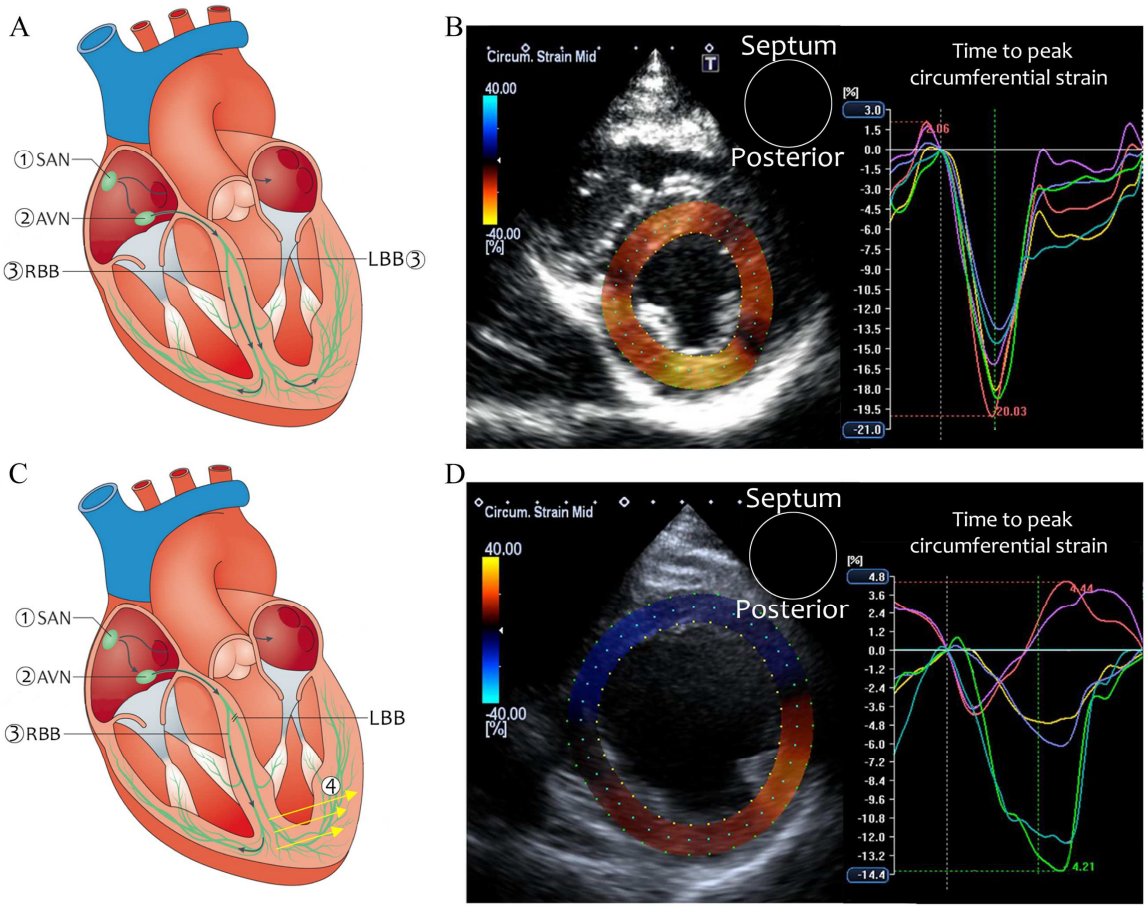

Figure 1-1. Effects of electrical dyssynchrony on systolic contraction
The normal cardiac conduction path (A) and the circumferential LV strain and time to peak strain measured in a healthy patient using 2D echocardiographic speckle tracking (B) are shown. The LBBB conduction path (C) and circumferential LV strain and time to peak strain measured in an LBBB patient (D) are shown. The speckle-tracking images in the healthy patient show coordinated contraction of the LV and synchronous development of peak wall strain. The images from the LBBB patient show that the septal wall is moving away from the posterior LV wall and that development of peak strain is staggered. Panels A and C are adapted with permission from Cingolani et al. [19] and panels B and D are adapted with permission from Gorcsan et al. [20].

1.2 Cardiac resynchronization therapy

The effects of abnormal ventricular activation, and in particular that of LBBB, can be ameliorated by cardiac resynchronization therapy (CRT), which utilizes an LV pacing lead in addition to the right atrial RA and RV leads of a traditional pacemaker to create synchronized biventricular activation wavefronts and improve systolic function [8]. The

effectiveness of CRT has been demonstrated in a number of large, randomized, multicenter studies, and mortality rates in HF patients who receive CRT devices are half those of HF patients on standard-of-care medical (i.e., drug-based) therapy [21]. As a result of this evidence, over 50,000 HF patients now receive a new CRT device each year at an associated annual cost of $20 billion [22, 23]. However, in spite of the broad-spectrum success of CRT, at least 30% of all recipients are non-responders to therapy [24]. These patients, who fail to respond to CRT based on echocardiography and/or clinical criteria, have a 5-year survival probability of 50%, while >90% of responders are likely to survive over the same time frame [25].

Causes for non-response to CRT can be divided based on three different points of patient care: (1) CRT candidate evaluation, (2) CRT device implant, and (3) CRT setting selection. Although the factors associated with successful CRT device implant (patient anatomy and availability of non-apical sites for LV lead placement) are well characterized [26], the appropriate tools and criteria for CRT candidate evaluation and setting selection are much less clear [27-29]. Specifically, the current standard clinical measures for assessment of cardiac dyssynchrony in candidates for and patients with CRT devices, i.e., 12-lead electrocardiogram (ECG) QRS complex duration (QRSd) and morphology, are limited in their ability to predict patient CRT outcomes [30-34].

1.2.1 Evaluation of CRT candidates

The goal of CRT candidate evaluation is to determine, based on data available pre-implant, if a given patient is likely to respond to the therapy. Traditional candidates selected

for CRT are patients with a wide 12-lead ECG QRSd and an LBBB 12-lead ECG morphology [8]. However, QRSd criteria for CRT implant have varied across previous seminal multicenter studies and differ between the European and American guidelines [30, 31, 34, 35]. In addition, the predictive value of the 12-lead ECG QRSd is diminished by extreme interobserver variation [36]. A recent study found, for instance, that 47% of 12-lead ECG QRSd values differed by more than 20 ms, or by >16%, when measured by multiple cardiologists and/or a clinical 12-lead ECG machine [37]. At the same time, the definition of LBBB morphology for CRT candidate evaluation continues to evolve [8, 33, 34], and the impact of more stringent LBBB criteria on patient outcomes has not been consistent [38-40]. The benefit of CRT in the non-LBBB population is even more uncertain and has varied in multicenter studies [39, 41, 42].

1.2.2 CRT setting selection

The goal of CRT setting optimization is to identify the CRT device parameters that create the most synchronized activation wavefronts, which may be accomplished by fusion with or inhibition of the pre-existing native conduction behavior [43]. Although CRT settings can be manipulated noninvasively through the device programmer, identification of the optimal CRT settings requires evaluation of a myriad of device settings, from atrioventricular and interventricular delays to pacing vectors. In addition, CRT setting optimization is only becoming more complicated with the advent of new features such as multipoint pacing [27]. As a result, post-implant optimization of CRT settings is rare even

though the link between suboptimal setting selection and CRT non-response is well established [28, 29, 44].

Although there are a number of setting selection algorithms integrated into current CRT devices, these vary by device manufacturer, are limited to optimization based on timing interval measurements acquired with the implanted pacing leads, and are not available in older devices in chronic CRT patients [29, 45]. In addition, CRT setting selection driven by QRSd reduction is supported by some investigators, but the relationship between changes in QRSd and patient LV reverse remodeling remains uncertain [32, 46, 47]. Moreover, use of 12-lead ECG morphologic criteria for CRT setting selection is complex and, as a result, is seldom done [8, 32, 33, 48, 49].

1.2.3 Alternatives to the 12-lead ECG

The persistence of current 12-lead ECG criteria for CRT patients is driven by (1) ease of use and (2) lack of viable alternative measures [27]. A patient can be prepared for a 12-lead ECG in less than 5 minutes, there are no exclusion criteria, and a 12-lead ECG takes 10 seconds to acquire. The minimal training required and lack of associated imaging also reduce the personnel and equipment costs to acquire a 12-lead ECG.

Echocardiography-based measures of mechanical dyssynchrony for CRT candidate and patient evaluation have been explored by a number of studies because echocardiography is already integrated into standard CRT patient care for quantifying LV systolic function and response to CRT (i.e., improvement in ejection fraction and/or reduction in LV end-systolic volume [LVESV]). Unfortunately, although *post hoc* analyses have shown that responders

to CRT have more dyssynchrony pre-CRT than non-responders, trials using mechanical dyssynchrony markers from echocardiograms as implant criteria in CRT candidates have failed [27, 50, 51]. In addition, use of echocardiograms to serially evaluate CRT settings would be prohibitively time- and resource-intensive for routine clinical practice [29].

To take advantage of the electrical basis for CRT therapy, new noninvasive methods for CRT candidate and patient evaluation have focused on quantifying electrical dyssynchrony. The majority are based either on novel 12-lead ECG metrics, such as the QRS integral [52], or on vectorcardiogram (VCG) metrics, such as QRS area and the QRS vector [53-56]. Although preliminary studies with these metrics show an improved correlation with patient hemodynamic and LV reverse remodeling outcomes over traditional 12-lead ECG metrics, they still capture only a limited view of cardiac activation, which is restricted by the quantity and placement of electrodes used with these systems [57, 58]. In contrast, multichannel ECG (MECG) systems, which utilize ECG arrays with 50 to 250 electrodes and cover a large area of the anterior and posterior torso, provide a more detailed and complete picture of cardiac activation [58]. MECG systems may be grouped into two modalities: (1) electrocardiographic imaging (ECGi) and (2) body surface activation mapping [35, 59-62]. In ECGi, MECGs are combined with a computed tomography scan of a patient's heart in order to back-calculate the activation sequence on the epicardial surface [63]. The level of detail available with ECGi has greatly advanced the understanding of electrophysiologic substrate behavior in CRT patients [63-65], but the associated imaging and computational costs make ECGi ill suited for routine evaluation of CRT candidates and/or patients. Body surface activation mapping is more readily

applicable for clinical use because it relies on the MECGs as a bulk surrogate for the underlying substrate behavior [59-62, 66-68]. Previous body surface activation mapping studies in CRT patients have used either isopotential maps [59, 60, 67, 68] or activation time metrics to describe the therapy's effects on depolarization and repolarization activity [61, 62]. In particular, two measures of body surface activation derived from MECGs acquired with a custom ECG Belt investigational body surface mapping system (see below) have been shown in clinical studies to correlate with hemodynamic changes at different LV lead locations during CRT implant [62] and to correlate with LV reverse remodeling after CRT [61].

1.2.4 Studies with the ECG Belt investigational body surface mapping system

The ECG Belt investigational body surface mapping system consists of a disposable array of 53 unipolar ECG electrodes (see Figure 2-2), a multichannel amplifier, and a monitor (Heartscape, Verathon, Seattle, WA) and customized data acquisition software (Medtronic, PLC, Minneapolis, MN). Data acquisition with this system has been shown to be feasible in an outpatient clinic [61]. Previous studies using the ECG Belt, as well as other body surface activation mapping studies [69, 70], have defined a local body surface activation event as the point of steepest negative slope during the QRS complex in each ECG, based on an extension of contact mapping principles [71]. This definition of local body surface activation has been shown to accurately represent depolarization activity in the underlying myocardium [69]. Local body surface activation times are then calculated with reference to the earliest recorded local activation event and interpolated to create

isochronal activation maps [61, 62]. Last, the dyssynchrony of the activation sequence is quantified based on the standard deviation of the activation times (SDAT) and the average left thorax activation time (LTAT) [61, 62]. Although both SDAT and LTAT were evaluated in the acute hemodynamic outcomes study [62], only SDAT was used in the study of chronic LV reverse remodeling outcomes with CRT [61]. In that study[1], which was performed from mid-2014 to mid-2016, the change in SDAT from native conduction to CRT was better correlated with LVESV outcomes than was change in 12-lead ECG QRSd, but the SDAT correlation with LVESV outcomes was still mild ($r^2 = 0.12$, $p < 0.01$) [61].

1.2.5 Criteria for clinical adoption of body surface mapping for CRT candidate and patient evaluation

In order to be a viable and effective solution to CRT non-response, body surface activation metrics and maps (1) must reflect the underlying electrical substrate behavior and (2) must demonstrate a correlation with patient CRT outcomes that is not only better than current 12-lead ECG measures but also sufficient to allow the accurate prediction of outcomes in most patients. In addition, the associated body surface activation system and MECG analysis software must generate reproducible results in a time frame suitable for clinical use.

[1] Data from this previous prospective study will be used throughout this dissertation. The study in question was initiated and conducted by the research department at United Heart and Vascular Clinic; study funding and equipment were provided by Medtronic, PLC. Initial results from this study were published in Gage et al. [56]

The goal of the work described in this dissertation was to develop new tools and metrics that build upon the existing ECG Belt investigational body surface mapping system to address and/or improve upon the system's performance against these criteria. These aims are addressed as follows. Chapter 2 describes the development and validation of automated QRS complex detection and QRSd measurement algorithms specifically designed for the challenges of MECGs acquired in the CRT population. Chapter 3 investigates the effects of noise on SDAT reproducibility and possible methods to mitigate these effects. Chapter 4 describes a pilot study of the use of mapped body surface activation sequences to identify LBBB-like IVCD patients. Chapter 5 describes seven novel body surface activation metrics and associated models of patient CRT outcomes for CRT candidate evaluation and setting selection. Last, chapters 6 and 7 describe the variation in LV orientation and position in the HF population and a pilot study of the effects of such variation on the models of patient outcomes described in Chapter 5.

2 QRS Complex Detection and Measurement Algorithms for Multichannel ECGs in Cardiac Resynchronization Therapy Patients

This chapter has been accepted for publication in the *IEEE Journal of Translational Engineering in Health and Medicine* and is reprinted with permission.

Antonia E. Curtin, Kevin V. Burns, Alan J. Bank, and Theoden I. Netoff. "QRS Complex Detection and Measurement Algorithms for Multichannel ECGs in Cardiac Resynchronization Therapy Patients." Accepted May 20th, 2018.

2.1 Overview

2.1.1 Introduction

We developed an automated approach for QRS complex detection and QRS duration (QRSd) measurement that can effectively analyze multichannel electrocardiograms (MECGs) acquired during abnormal conduction and pacing in heart failure (HF) and cardiac resynchronization therapy (CRT) patients.

2.1.2 Methods

The algorithms use MECGs acquired with a custom 53-electrode investigational body surface mapping system and were validated using previously collected data from 58 CRT patients. An expert cohort analyzed the same data to determine algorithm accuracy and error. The algorithms (1) detect QRS complexes, (2) identify complexes of the most prevalent morphology and morphologic outliers, and (3) determine the array-specific (i.e., anterior and posterior) and global QRS complex onsets, offsets, and durations for the detected complexes.

2.1.3 Results

The QRS complex detection algorithm had a positive predictivity and sensitivity of ≥96% for complex detection and classification. The absolute QRSd error was 17 ± 14 ms ($p = 0.21$), or 12%, for array-specific QRSd and 12 ± 10 ms ($p < 0.01$), or 8%, for global QRSd. The absolute global QRSd error (12 ms) was less than the interobserver variation in that measurement (15 ± 10 ms).

2.1.4 Conclusions

The QRS complex detection and measurement algorithms performed as well as the current state-of-the-art algorithms designed for and limited to simpler data sets and conduction patterns and within the variation found in current clinical 12-lead electrocardiogram (ECG) QRSd measurement techniques. These new algorithms permit accurate, real-time analysis of QRS complex features in MECGs in patients with conduction disorders and/or pacing and enable the future use of MECGs to improve characterization of cardiac activation in such patients.

2.2 Introduction

QRS complex measured by 12-lead electrocardiogram (ECG) is the main feature in the diagnosis of a number of cardiac pathologies. In the heart failure (HF) population, QRS complex duration (QRSd) and morphology are key criteria for assessing electrical activation in candidates for and patients with cardiac resynchronization therapy (CRT) [30, 31]. However, in spite of the clinical ubiquity of the 12-lead ECG in CRT patient care, its

sensitivity to relevant electrophysiologic substrate behavior in that population is limited [34, 72]. Recently, QRS complex features measured in multichannel electrocardiograms (i.e., ECGs from arrays with 50 to 250 electrodes [MECGs]) have been investigated to describe cardiac activation in CRT patients while addressing the spatial limitations of the 12-lead ECG and with the goal of concomitantly reducing patient non-response, which affects 30% of CRT recipients [35, 59-61]. However, manual evaluation of the requisite QRS complex features would be prohibitively labor-intensive in MECGs and is not even routinely performed using 12-lead ECGs [32, 33, 49]. An automated analysis approach is therefore needed if CRT patients are to benefit from the increased information content of QRS complex features measured in MECGs.

Automated QRS complex detection and measurement algorithms for MECGs are lacking. In body surface mapping studies using MECGs for myocardial infarction detection and for activation mapping, "semi-automated" (i.e., template matching) or completely manual QRS complex detection methods are used in combination with manual QRSd measurement [73-75]. Semi-automated detection strategies require the *a priori* identification of the QRS complex morphology of interest and have difficulty discriminating QRS complexes from T-waves [76]. In the single identified system for automated QRS complex detection in MECGs, the algorithm used was designed to detect QRS complexes during episodes of ventricular tachycardia and relied on specific features associated with that condition [77, 78]. In addition, current 12-lead ECG QRS complex detection and QRSd measurement algorithms are ill suited for translation to MECGs. Although generally characterized by high sensitivity and positive predictivity, these

methods are typically validated using single-channel 12-lead ECG data from the MIT-BIH database and struggle with negative-polarity complexes, very wide complexes, and low-amplitude complexes [79, 80].

ECGs of any type acquired from HF and CRT patients exhibit all of the characteristics that conventional 12-lead ECG algorithms struggle with. The HF and CRT patient populations represent a variety of conduction delay pathologies, each of which is associated with a different QRS complex morphology and polarity. Patients with left bundle branch block (LBBB), who make up the majority of CRT recipients, are characterized by large negative peaks on ECGs because of the anterior-to-posterior direction of cardiac activation [81]. Signal amplitudes in the HF and CRT populations may also vary widely due to the large range of body mass indexes present in this group [82, 83]. In addition, these patients require the analysis of ECGs acquired not only during native conduction but also during pacing. In paced patients, device settings may not uniformly affect the cardiac cycle, and associated QRS complex changes cannot be predicted or described programmatically because of the individual nature of the electrophysiologic substrate response [64]. Furthermore, CRT patients may experience any combination of native conduction breakthrough, premature ventricular contractions, premature atrial contractions, fusion beats, and paced beats during CRT. A successful QRS complex detection algorithm for use with MECGs from CRT patients must correctly identify the electrical substrate behavior (i.e., QRS complex morphology) that the patient experiences most frequently, in spite of these confounding factors.

This study describes the paired development and validation of an automated MECG

QRS complex detection algorithm and MECG QRSd measurement algorithm to address the dual challenges of automated feature detection in MECGs and the idiosyncrasies of electrical substrate behavior in the CRT population. When the algorithms are used in tandem, the QRS complex detection algorithm identifies and classifies all of the QRS complexes associated with the most prevalent conduction pattern (i.e., most prevalent complex morphology) in a given MECG recording and the QRSd measurement algorithm delineates the array-specific (i.e., anterior and posterior) and global start and end points and measures the corresponding QRSd in each complex. Algorithm performance was determined by comparing the QRS classification and QRSd measurement results with those independently acquired from an expert cohort. The algorithm described herein has been submitted for a patent [84].

2.3 Methods

2.3.1 Study population

Algorithm development and validation were performed using data collected for a previous study of advanced systolic HF patients who had received new CRT implants between 2014 and 2017 at United Heart and Vascular Clinic in St. Paul, MN[2]. For that study, written informed consent was obtained from all patients, and the study protocol was approved by an institutional review board (IRB). Both 12-lead ECGs and MECGs were

[2] Data from this previous prospective study will be used throughout this dissertation. The study in question was initiated and conducted by the research department at United Heart and Vascular Clinic; study funding and equipment were provided by Medtronic, PLC. Initial results from this study were published in Gage et al. [56]

used, the latter of which were acquired with a custom ECG Belt investigational body surface mapping system (see below). Data was available from 149 patients during native conduction (CRT off) and with CRT on at a range of device settings.

Algorithm development was performed using training data from 5 patients, and data from an additional 10 patients was used for the validation step while optimizing algorithm parameters. These 15 patients included right bundle branch block, LBBB, nonspecific intraventricular conduction delay, and complete heart block patients. Data from a separate group of 58 patients was used for the final phase of algorithm validation, as described in later sections.

2.3.2 MECG acquisition

The ECG Belt system has been described elsewhere [11, 12]. Briefly, the investigational system consists of a multichannel amplifier, a monitor, and electrode array (Heartscape, Verathon, Seattle, WA) and customized data acquisition software (Medtronic, PLC, Minneapolis, MN). The ECG Belt electrode array is composed of 53 (17 anterior and 36 posterior) unipolar ECG electrodes arranged on the torso as shown in Figure 2-2. MECGs for a given condition were collected in 15- to 20-second recordings at a sampling rate of 1 kHz and bit resolution of 24 bits and saved offline for subsequent analyses.

2.3.3 QRS detection and QRSd measurement algorithms

2.3.3.1 Implementation of algorithms

The following preprocessing method, QRS detection algorithm, and QRSd

measurement algorithm have been implemented in comprehensive stand-alone software[3] written in MATLAB (using MATLAB Release 2017b, The MathWorks, Inc., Natick, MA) that supports the loading and serial analysis of MECGs collected during multiple conditions from one or more patients. The data preprocessing method and both algorithms make use of built-in MATLAB functions, including those provided with the digital signal processing (DSP) system toolbox, the signal processing toolbox, and the statistics and machine learning toolbox.

A complete analysis identifies all of the QRS complexes in a given recording, classifies each complex as predominant or outlier morphology (PM or OM, respectively), delineates the array-specific (i.e., anterior and posterior) and global start and end points of each of the PM complexes, and measures the array-specific and global QRS durations. The software also automatically generates figures for ready visualization of the results of the QRS detection and QRSd measurement algorithms for each recording. In addition, we have created a second version of the software with a graphical user interface (GUI) front end for use by an operator unfamiliar with the MATLAB scripting language.

2.3.3.2 Data preprocessing

Prior to analysis with the QRS complex detection algorithm, each recording underwent filtering, channel redaction, splicing, and baseline correction. Filtering was performed with a 0.5- to 25-Hz passband filter [7, 85-87]. An acceptable absolute (i.e., positive or negative)

[3] The University of Minnesota, Minneapolis, MN, and United Heart and Vascular Clinic, St. Paul, MN

peak amplitude range of 0.10 to 4.0 mV, derived from 12-lead ECG data, was then applied to identify and remove channels of data from non-contacting or poorly contacting electrodes. A power spectrum analysis using the short-time Fourier transform was used to identify, remove, and splice around segments of the recording containing relatively large amounts of high-frequency noise.

2.3.3.3 Automated QRS complex detection algorithm

The QRS complex detection algorithm consists of five main stages designed to identify all of the QRS complexes in a recording and subsequently classify them as PM or OM complexes without the use of template matching or any *a priori* assumptions regarding QRS complex morphology. These stages are (1) channel grouping and averaging, (2) peak detection, (3) definition of QRS complex windows, (4) identification of additional complexes, and (5) classification of QRS complex morphologies. Each main sub-step of the detection algorithm is shown in the flowchart in Figure 2-1. The criteria used to execute each sub-step are presented, as applicable, in Table 2-1. Figures 2-2 and 2-3 illustrate the main results of each stage using data collected in an LBBB patient at AdaptivCRT (aCRT) settings during a point in time when left-ventricle-only pacing with an atrioventricular delay of 90 ms was being delivered by the CRT device. This patient had approximately two premature ventricular contractions (PVCs) per minute and frequent premature atrial contractions, which caused uneven beat-to-beat (i.e., RR) intervals. For easier visualization of signal features, only the first 7.5 seconds of the 15-second recording are used in Figures 2-2 and 2-3.

The purpose of stage 1, channel grouping and averaging, is to create an average signal that is representative of each distinct ECG morphology present in the recording. Channel grouping and subsequent averaging leverage the redundancy of the MECGs to enhance large-amplitude, low-frequency features, which can then be used for peak detection. In order to efficiently and effectively group the channels, a time segment of data with sufficient non-isoelectric content to allow morphologic comparisons between channels must be extracted from the complete recording (see steps 1a and 1b in Figure 2-1). Grouping of channels is independent of source electrode location. Figure 2-2 shows the channel grouping and averaging results for the sample recording. Forty-five of the 53 electrodes were placed into five groups, as shown in the torso diagrams in Figure 2-2. The average signal for each group is shown next to its respective torso diagram.

The purpose of stage 2 is to identify the peaks in each average signal that have features characteristic of QRS complexes and that belong to the PM complexes. QRS complex peaks are assumed to be larger in amplitude and narrower than T-wave peaks. The number of same-polarity peaks with QRS-complex-like features is used to avoid morphologic outliers (i.e., peaks from OM complexes). Peak detection is performed in each average signal separately and based on a threshold specific to that average signal. The QRS complex peaks in each average signal are indicated with blue Xs in Figure 2-2. After the QRS complex peaks are identified in each average signal, peaks belonging to the same QRS complex are identified across the average signals. Figure 2-3 shows the peaks in three consecutive QRS complexes in the same sample recording.

Table 2-1. Criteria for QRS complex detection algorithm steps

Step	Action	Parameter	Value/Criteria [A]
1a.	Relevant time segment selection	Initial length	70-bpm cycle length
		Length options	Cycle length for ± 10 bpm
1b.	Channel grouping	Morphological features	Linear model fit
			Peak polarities, magnitudes, and temporal position
		Grouping over-fits	Too many small groups
		Segment insufficient	Too few groups
		Successful grouping	≥3 Groups of ≥3 channels
2a.	Peak detection	Detection threshold for a given average signal	Maximum minimum peak height identified over 1,000-ms increments
2b.	Peak down-selection	Peak amplitude	Group of peaks within ± 0.1 mV [B]
		Peak width	Group of peaks within ± 20 ms [B]
2c.	Comparison of peaks across average signals	Maximum intra-complex peak-to-peak distance	81 ms [C]
4.	Identification of additional complexes	Section(s) of the recording in which to detect additional peaks	Any interval between PM complexes that is larger than the calculated RR interval
5a.	Comparison of complex morphologies	Morphological features	Cross-correlation
			Complex maximum peak amplitude and sign

[A] Criteria without sources were determined during the development process.
[B] Based on precision of 12-lead ECG grid paper.
[C] Based on difference ($\mu + 2\delta$) between paired global and widest single-lead 12-lead ECG QRSd measurements (n = 149).

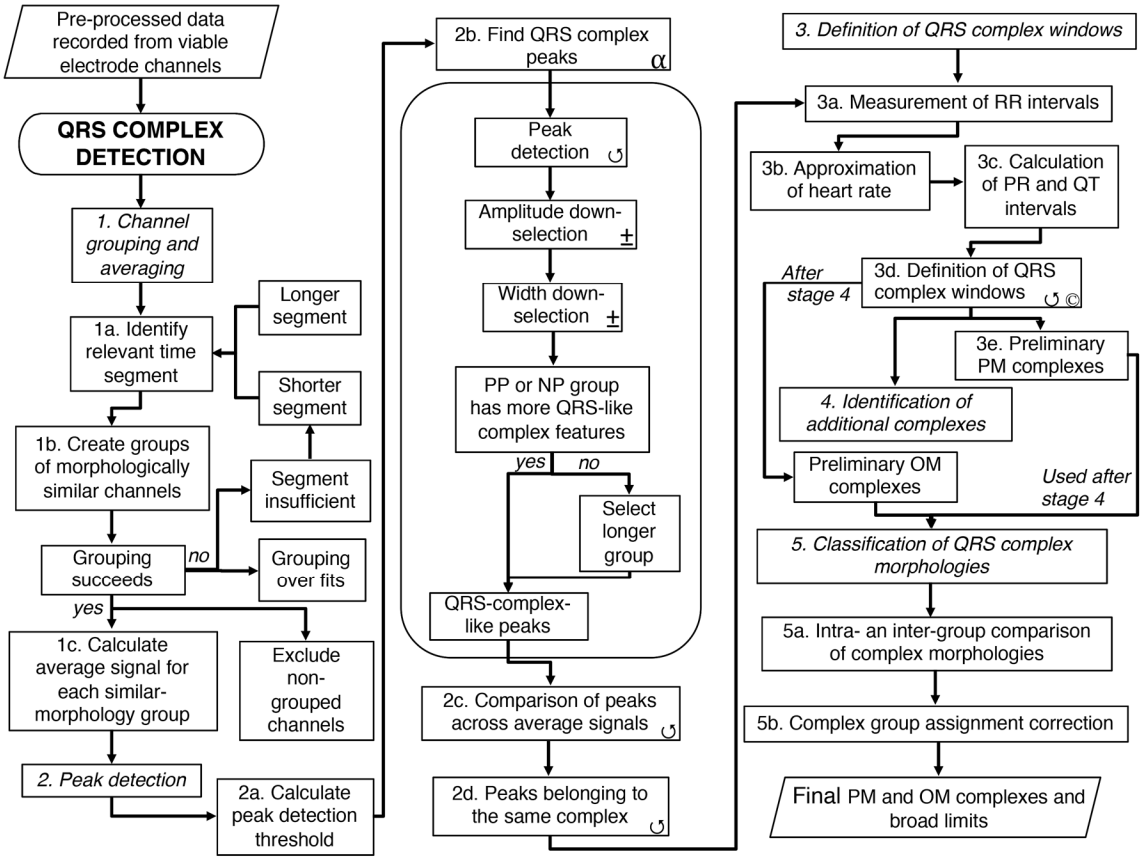

Figure 2-1. QRS detection flowchart

The QRS detection method consists of five main stages. The alpha symbol (α) is used to indicate steps applied to each average signal separately. In stage 2, the steps indicated with the ± symbol are applied to the group of positive peaks (PP) and the group of negative peaks (NP) separately. In addition, the steps inside the rounded rectangle are performed for each average signal separately. In stage 3, the steps indicated with the © symbol are applied to each QRS complex separately. In stage 4, the previous steps indicated with the ↺ are repeated in numerical order. Parallelograms are used to indicate algorithm inputs and outputs.

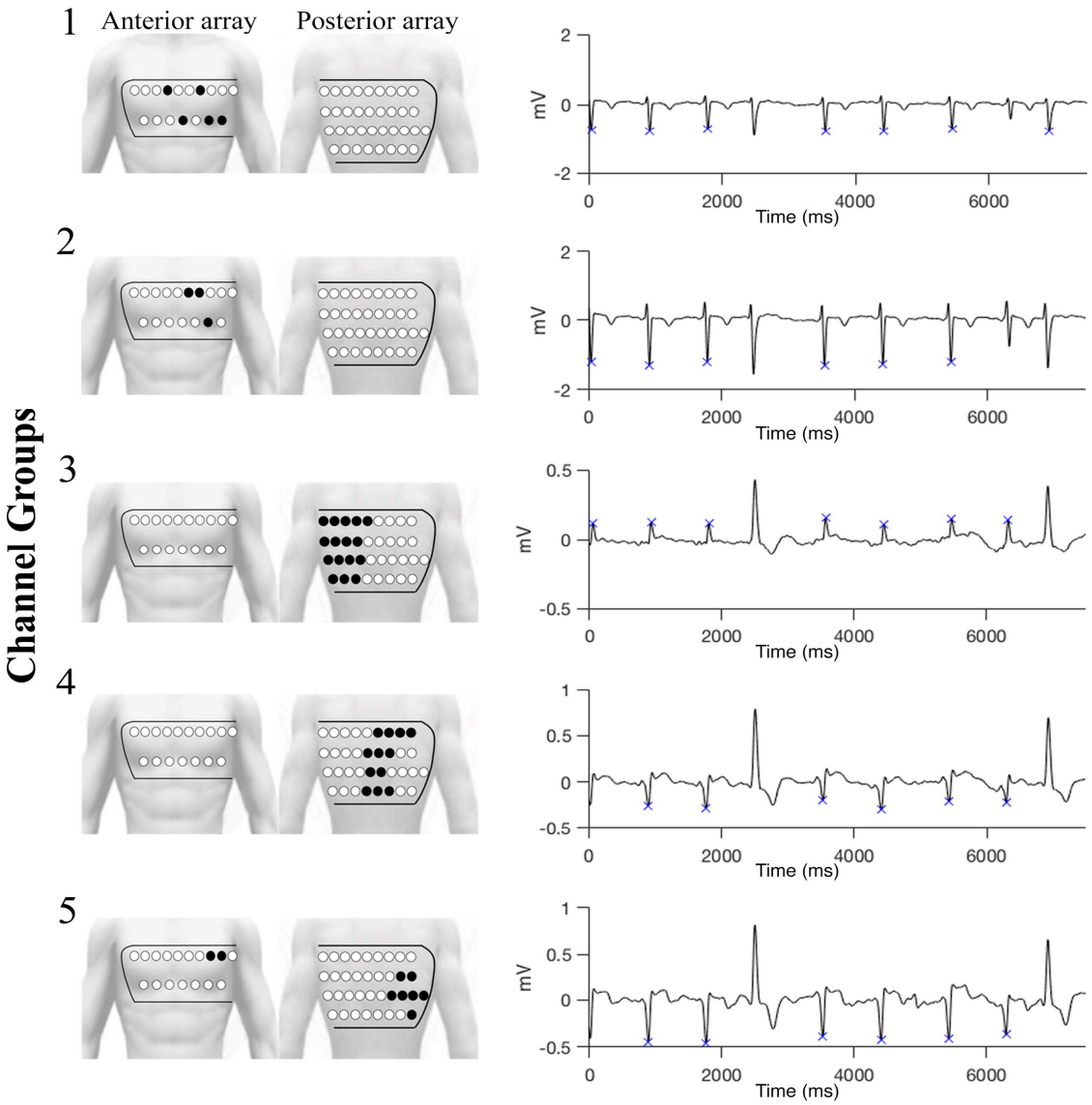

Figure 2-2. Example average signal groups and QRS complex peaks
Five groups of channels with distinct morphologies were identified in the sample recording (see text). The electrodes belonging to each group are shown in black (left). The associated average signals are shown to the right of the respective torso diagram, and the identified QRS complex peaks in each average signal are indicated with blue Xs.

In stage 3, each QRS complex is defined by a window (i.e. broad limits) around it. QRS complex windowing is necessary for subsequent morphological comparisons between complexes. Each QRS complex window is broadly defined to ensure that the leading and trailing edges of the complex are accounted for: the limits of each window are wider than

the complex itself and include an approximated PR interval preceding the first peak in the QRS complex, the interval over which the complex peaks occur, and an approximated QT interval following the last peak in the complex. The complexes thus defined at the end of stage 3 are preliminarily classified as PM complexes. Figure 2-3 also shows the window around each of the three QRS complexes.

The purpose of stage 4 is to identify any QRS complexes present in the recording but not identified in stage 2 and to subsequently define the windows around them. This stage is necessary to ensure that as many PM complexes as possible are identified, and it utilizes the more-informed description of PM complex features available after stage 3 to identify any complexes erroneously excluded on the basis of the information available during stage 2. Any complexes resulting from this stage are preliminarily classified as OM complexes. In stage 5, the morphologies of identified complexes are compared to finalize their classification as either PM or OM. This final comparison uses the complete QRS complex (i.e., not only the peaks) to confirm classifications. Complexes with morphologies that do not match the other complexes in their class are then reassigned as needed.

At the completion of all of the identification and classification steps, all of the QRS complexes associated with the most prevalent electrical substrate behavior have been identified, as have those associated with anomalous or ectopic behavior. This information can subsequently be used to measure the PM-to-OM complex ratio (i.e., OM complex burden), perform other analyses of the electrical substrate behavior, and/or measure the QRSd in each PM complex, as described below.

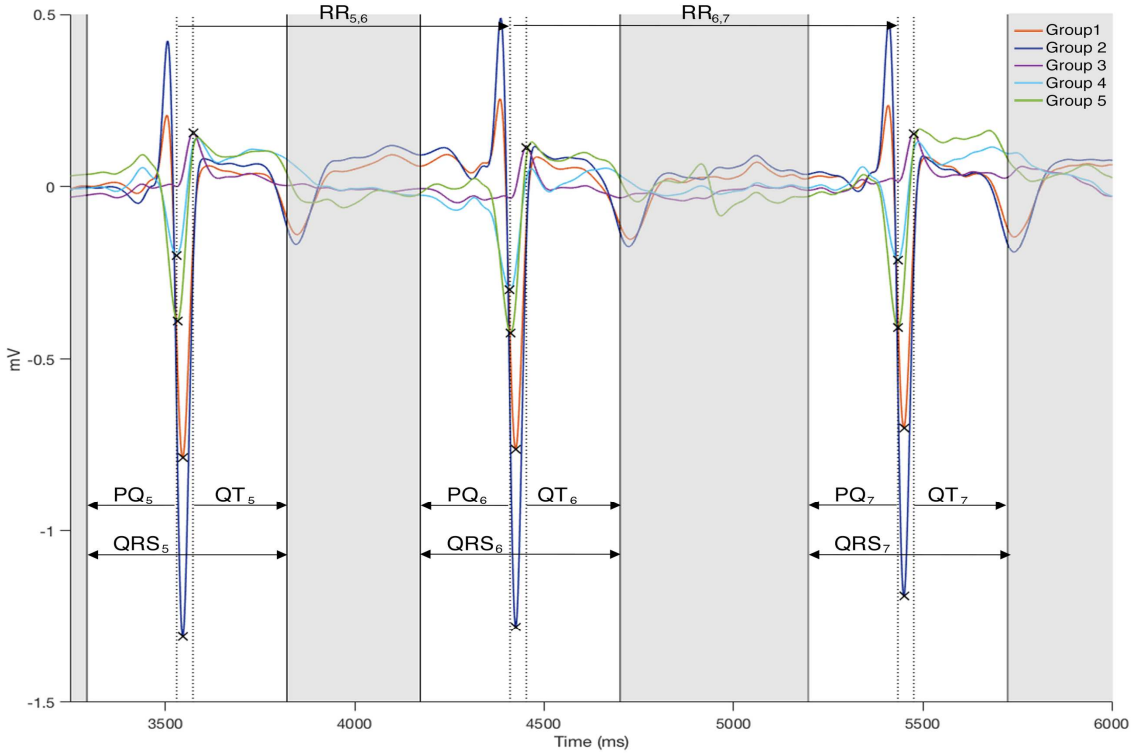

Figure 2-3. Example PM complexes
Three consecutive PM complexes identified in the sample recording (see text). The average signal is shown in a different color for each of the five groups. QRS complex peaks are indicated with black Xs. Vertical dotted lines mark the first and last peak in each complex. The RR interval is the distance (time) between the first peak in each complex and that of the following complex. The PQ and QT intervals are approximated based on previously published equations [88, 89]. The shaded area defines the broad window around each QRS complex, which is designed to encompass the leading and trailing edges of the complex.

2.3.3.4 Automated QRS complex detection algorithm

The QRSd measurement algorithm is designed to delineate and measure the array-specific (i.e., anterior and posterior) and global QRS complex durations in each PM complex identified with the QRS detection algorithm.

Because the QRSd algorithm is designed to measure the QRSd separately in the data collected from the anterior and posterior arrays, array-specific morphologic outliers are identified prior to the application of the algorithm. The algorithm consists of five stages, which will be referred to as stages 6 through 10 for continuity with the QRS detection

algorithm. The stages are (6) the identification of significant peaks in each channel, (7) the formation of array-specific peak groups, (8) the delineation of channel-specific QRS complex borders, (9) the delineation and measurement of array-specific QRS complex borders and durations, and (10) the delineation and measurement of the global QRS complex borders and duration. The sub-steps of the QRSd algorithm are shown in Figures 2-4 and 2-5. The criteria used to execute each sub-step are presented, as applicable, in Table 2-2.

The purpose of stage 6 is to identify in each channel all significant peaks that occur within the QRS complex window, as determined with the QRS detection algorithm, to prevent cropping of important QRS complex features. Stage 6 consists of two parts for each channel (see Figure 2-5): identification of the reference peak and evaluation of other candidate peaks to determine their significance. The reference peak in each channel is the largest-amplitude peak, and the other significant peaks are those that fall on either side of the reference peak and meet the concavity and slope criteria derived from the reference peak. Subsequently, in stage 7, two array-specific peak groups are formed: one consisting of all of the reference and significant peaks in the anterior channels and one consisting of all of the reference and significant peaks in the posterior channels.

Table 2-2. Criteria for QRSd measurement algorithm steps

Step	Action	Parameter	Value/Criteria [A]
N/A	Removal of array-specific outliers	Morphological features	Cross-correlation
			Peak polarities, magnitudes, and temporal position
		Exclusion criteria	Channel a morphologic outlier in the first, middle, and last PM complex
6.	Identification of peak bounds	Leading or trailing peak boundary	Earlier of zero-crossing and concavity change
	Significance assessment	Order of candidate peak evaluation	Ascending proximity to the reference peak
	Peak significance criteria	Peak position	Occurs after preceding significant peak bounds
		Peak amplitude	Opposite polarity of preceding significant peak
		Criteria scaling factor	Ratio of candidate peak height to reference peak height
		Leading and falling phase slope	Reference peak slope × scaling factor
		Leading and falling phase curvature	Reference peak curvature × scaling factor
7.	Removal of array-specific peak outliers	Maximum peak-to-peak spacing	52 ms [B]
8a.	Delineation of channel specific borders	Amplitude	<50% of the closest significant peak's height
		Slope	<2.5 × 10-2 mV/ms [C]
9.	Delineation of array-specific borders	Group of normal array-specific values	Largest group of borders within 20-ms
		Array-specific start	Earliest of array-specific normal start values
		Array-specific end	Latest of array-specific normal start values
10.	Delineation of global borders	Global start	Earlier of the array-specific start values
		Global end	Later of the array-specific end values

[A] Criteria without sources were determined during the development process.
[B] Based on precision of 12-lead ECG grid paper.
[C] Based on difference ($\mu + 1\delta$) between paired global and widest single-lead 12-lead ECG QRSd measurements (n = 149).

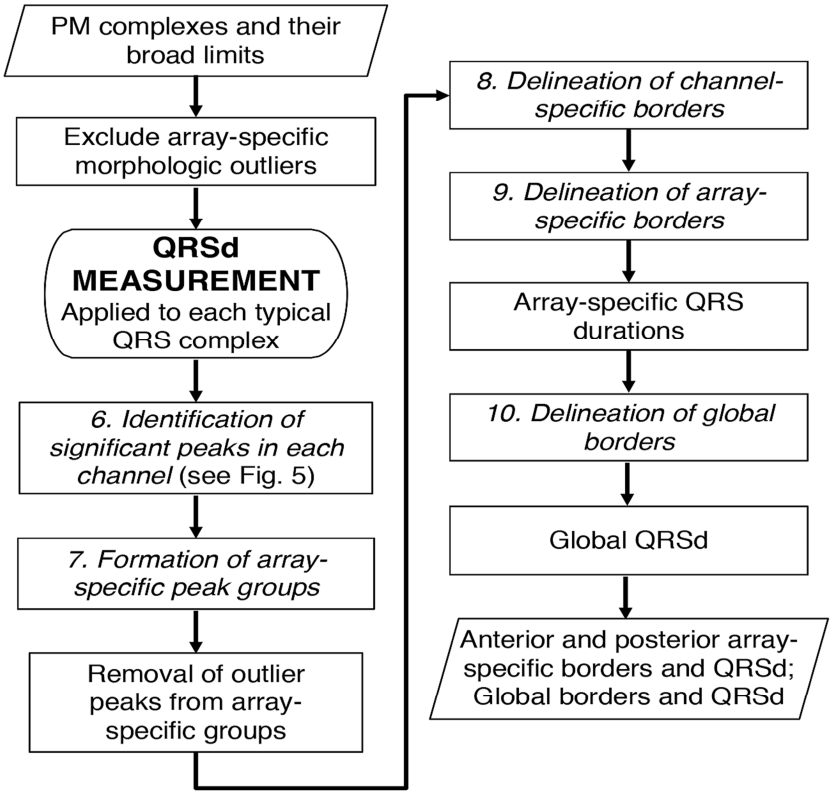

Figure 2-4. QRSd measurement flowchart
The QRSd measurement algorithm consists of five main stages, which are numbered continuously with those of the detection algorithm. Parallelograms are used to indicate algorithm inputs and outputs.

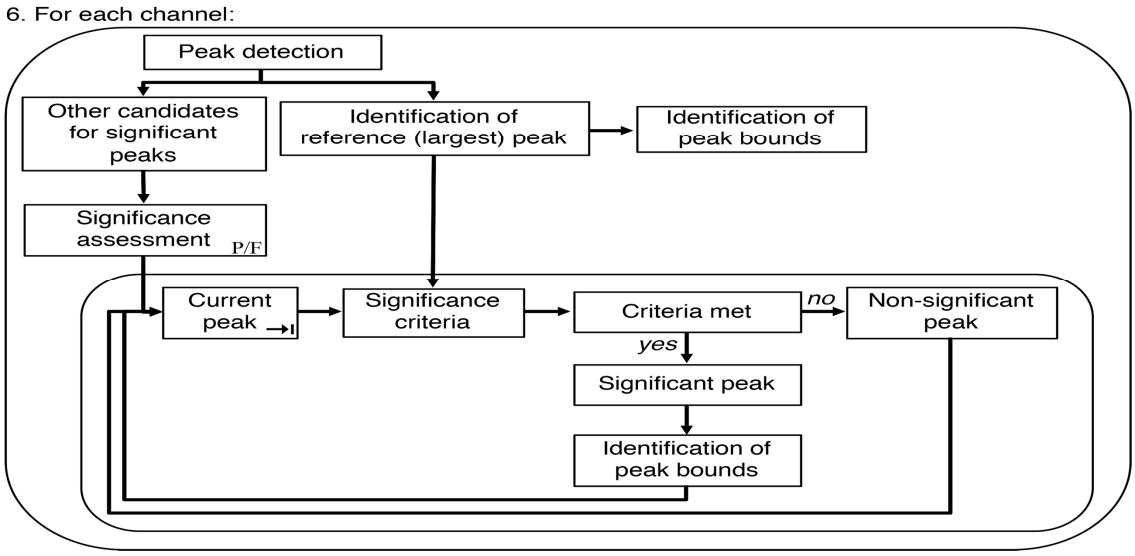

Figure 2-5. Identification of significant peaks in each channel
The identification of significant peaks in each channel is stage 6 of the QRSd measurement algorithm. The "P/F" symbol is used to indicate that the significance assessment is performed separately for the group of candidate peaks preceding the reference peak and the group following the reference peak. The ⇥ symbol is used to indicate that the significance assessment is performed for each candidate peak in turn (see Table 2-3).

In stages 8 to 10, the QRS complex borders (i.e., start and end points) are defined in each channel, the two pairs of array-specific borders are delineated, and the global QRS complex borders are delineated. The array-specific and global QRS durations are also measured. Figure 2-6 illustrates the results of stages 8 and 9 for the anterior channels of a PM complex from the same recording shown in Figures 2-2 and 2-3.

At the completion of the above steps, the array-specific and global QRS complex borders have been delineated, and the corresponding QRS durations have been measured for every PM complex in the recording. In addition to clinical significance of QRSd measurement, the QRS complex borders can be used to facilitate measurement of other QRS complex features, such as the QRS integral.

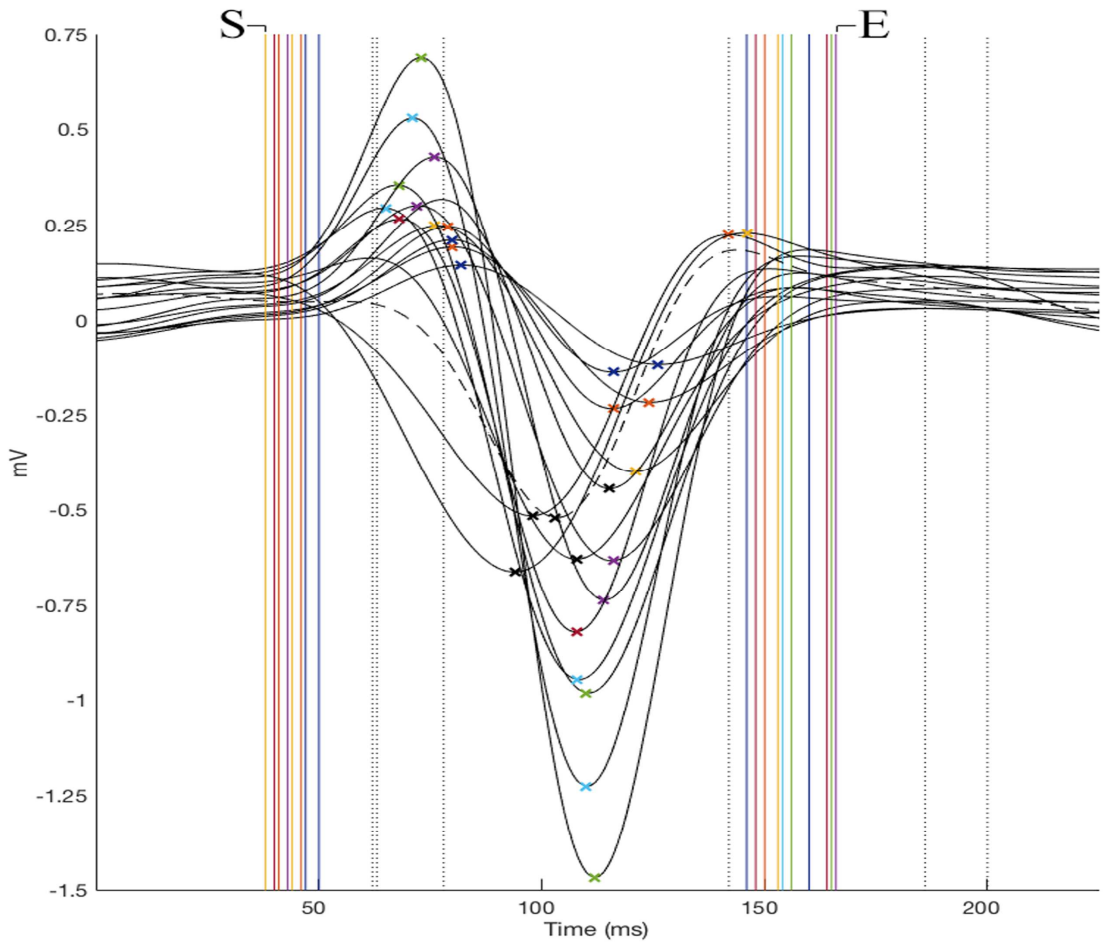

Figure 2-6. Example channel-specific and array-specific QRS complex borders
Data from all viable anterior channels in the sample recording (see text) is shown for part of the QRS complex window. Significant peaks are indicated with Xs. The channel-specific start and end borders are shown with vertical lines. Channel-specific start and end borders that do not belong to the group of normal values are indicated with black dotted vertical lines, while normal borders are indicated in color with solid lines. For channels with an abnormal border, the closest significant peak is indicated with a black X. All other significant peaks are indicated in a color that matches the color of the channel-specific border. In one channel, both the start and end borders were outside those of the normal groups and that channel is shown using a dashed line. The earliest channel-specific start ("S") and latest channel-specific end ("E") are the anterior array-specific borders.

2.3.4 Validation studies

2.3.4.1 QRS detection algorithm validation

Validation studies were selected from patients in the top 20% of the study population based on clinical PVC burden. First, each patient and recording were selected using a

random-number generator. Second, the presence of PVCs or of other QRS complex morphologic variation in the 12-lead ECG collected at the same settings was visually confirmed. Third, the un-analyzed MECGs were visually inspected for the presence of PVCs or other QRS complex morphologic variation. Availability of validation data was limited by two factors: (1) wide-spread anti-arrhythmic use in the study population and (2) optimization of CRT percent pacing prior to 12-lead ECG and MECG collection. Twenty recordings from 8 patients were ultimately selected. The selected validation studies represent native conduction and a range of pacing configurations. Two studies with no PVCs or visible morphologic variation were included as negative controls.

This data was then independently analyzed by an expert cohort. Four cardiac device nurses and one certified cardiac device specialist scientist made up the expert cohort used to evaluate the performance of the QRS detection algorithm. Each expert had more than 5 years of experience clinically evaluating QRS complex morphologies during pacemaker, implanted cardioverter defibrillator, and CRT device interrogations. The experts' responses were acquired using a purpose-made MATLAB GUI and digital calipers. Because of the difficulty of visually distinguishing the morphologies of 53 channels of data and because of the difference between MECGs and the single-lead ECG data used during clinical device interrogations, experts were presented with the average signals resulting from stage 1c (see Figure 2-1) on a single axis for each validation study. The experts were instructed to use the digital calipers (1) to indicate all QRS complexes and (2) to indicate any QRS complexes that appeared to be OM complexes compared to the other complexes in the recording. Respondents were asked to use the same level of precision as they would

during a clinical device interrogation. Respondents had the opportunity to edit their responses for each recording before proceeding to the next validation study. Three of five experts had to concur for a QRS complex to be classified as a PM or OM complex.

The QRS complex detection algorithm was evaluated on two criteria: (1) detection of QRS complexes and (2) classification of QRS complex morphology (i.e., PM or OM). Algorithm detection and classification performance were quantified by sensitivity and positive predictivity, per the Association for the Advancement of Medical Instrumentation guidelines [90]. Classification performance was additionally assessed for accuracy. The average percent concordance for each complex classified as a PM complex in a given validation study was used as a measure of expert uncertainty. The relationships between algorithm performance, the total number of complexes, the proportion of OM complexes (OM complex burden), and the extent of expert PM classification concordance were also investigated. The execution time of the detection algorithm was measured as an indicator of practicality for real-time use.

2.3.4.2 QRSd measurement algorithm validation

A single PM complex from each of 50 recordings during native conduction ($n = 20$) or CRT ($n = 30$) was blindly and randomly selected for QRSd measurement validation studies. Each recording came from a different patient, and the QRS detection and QRSd measurement groups of validation studies did not overlap. Due to the previously described difficulty of visually distinguishing the morphologies of 53 channels of data and the need for all channels to be accounted for in the global QRSd measurement, three research

scientists with extensive backgrounds in cardiac electrophysiology made up the expert cohort used to evaluate the QRSd measurement algorithm. The experts' responses were acquired using a purpose-made MATLAB GUI and digital calipers. For each validation study, each expert was presented with a single QRS complex identified by the algorithm and the 50 ms of data preceding and following the algorithm-determined global QRS complex borders, which were not shown. Due to preprocessing, pacing spikes were not visible in recordings collected during CRT. Data from the anterior and posterior channels was shown in colors from two different MATLAB color maps. The experts were asked to use the calipers to select the array-specific QRS start and end points for the anterior and posterior channels based on the earliest start and latest end point of the waveforms in the array-specific channels [91]. The array-specific and global QRS durations were then calculated automatically. Respondents had the opportunity to edit their responses for each recording before proceeding to the next validation study.

The QRSd measurement algorithm was evaluated for both array-specific and global QRSd delineation and measurement. Algorithm error was quantified with both the signed and absolute paired differences between the algorithm results and the results averaged from the expert cohort, which were calculated for both array-specific and global QRS onset, offset, and duration. The errors of the anterior and posterior array-specific QRSd measurements were also compared. For native conduction validation studies (n = 20), classification of QRSd values as narrow (<120 ms), moderate (120 to 150 ms), or wide (≥150) was evaluated using the global QRSd results. In addition, the influence on algorithm performance of QRS complex peak height (i.e., the average of the maximum anterior

channel peak height and the maximum posterior channel peak height), QRS width, and the proportion of viable channels was investigated. Last, interobserver variations in array-specific and global QRSd values for the expert cohort were measured, and the relationship between interobserver variation and algorithm QRS border and QRSd measurement accuracy were investigated. The execution time of the QRSd algorithm was measured as an indicator of practicality for real-time use.

2.3.5 Statistics

Data are expressed as means ± standard deviations. Student's unpaired *t*-test was used to analyze unpaired data. A paired *t*-test was used to analyze differences between paired measurements. Univariate regression was used to determine the relationships between algorithm performance and individual variables. Multivariate regression using backward stepwise elimination until all variables had a p value of <0.10 was subsequently used to identify significant predictors of QRSd measurement accuracy. For all other analyses, a p value of <0.05 was considered significant. All statistical analyses were performed using MATLAB.

2.4 Results

2.4.1 QRS detection algorithm validation

The total time for data preprocessing and analysis with the QRS complex detection algorithm was, on average, 30% of total recording length. Table 2-3 shows the detection performance of the algorithm for each of the 20 validation studies. The validation studies

contained a total of 267 complexes. The overall detection sensitivity of the algorithm was 99%, and its overall positive predictivity was 99%. Neither detection sensitivity nor positive predictivity was correlated with the number of complexes in the recording.

Table 2-3 also shows the classification performance of the QRS detection algorithm for each of the validation studies. In the studies with complexes of outlier morphology present (n = 18), the average OM complex burden was 16% (range, 7% to 39%). In total, the experts identified 231 complexes as PM complexes and 36 as OM complexes. The average expert classification concordance was 96%. The overall classification accuracy of the algorithm was 94%, with a sensitivity of 96% and a positive predictivity of 97%. The classification accuracy decreased with increasing OM complex burden ($r^2 = 0.23$, $p = 0.04$), while expert classification concordance remained consistent as the ratio of OM to PM complexes increased ($r^2 < 0.01$, $p > 0.1$).

Table 2-3. Performance of QRS detection algorithm

Pt. [A]	Detection [B]			Classification [C]					
	QRS (#)	Se (%)	P+ (%)	PM (#)	OM (#)	C (%)	Se (%)	P+ (%)	Ac (%)
1	11	100	100	10	1	100	100	91	91
2	12	92	100	11	1	90	100	91	91
	13	100	100	8	5	100	100	89	91
3	28	100	97	25	3	91	88	100	89
	14	100	100	14	0	100	100	100	100
	18	94	90	14	4	90	100	100	100
4	13	100	100	12	1	100	100	100	100
	11	100	100	7	4	92	86	100	91
	10	100	100	7	3	84	71	100	80
5	13	100	100	12	1	100	92	100	92
	14	93	100	13	1	99	100	100	100
	13	100	100	12	1	100	100	100	100
	13	100	100	11	2	97	100	92	92
6	12	100	100	11	1	100	100	100	100
	14	100	100	12	2	97	100	100	100
	12	100	100	12	0	95	92	100	92
7	17	100	100	16	1	100	100	100	100
8	7	100	100	5	2	100	100	83	86
	12	92	100	10	2	90	89	100	91
	10	100	100	9	1	92	100	90	90
Tot	267	99	99	231	36	96	96	97	94

[A] Pt. = patient.
[B] Se = sensitivity; P+ = positive predictivity.
[C] PM = predominant morphology; OM = outlier morphology; C = concordance; Ac = accuracy. Undetected and erroneously detected QRS complexes were not included in the calculations of the classification accuracy measures.

2.4.2 QRSd measurement algorithm validation

The total time for data preprocessing, analysis with the QRS detection algorithm, and analysis with the QRSd measurement algorithm was, on average, 90% of total recording length. The algorithm performance results for both array-specific and global QRS complex delineation and measurement are shown in Table 2-4. The average absolute algorithm error

was approximately 10 ms or less for the array-specific and global QRS onsets and offsets. As shown in the histogram in Figure 2-7A, the average absolute array-specific QRSd error was 17 ± 14 ms ($p = 0.21$), or 12% of the result averaged from the expert cohort. As shown in the histogram in Figure 2-7B, the average absolute global QRSd error was 12 ± 10 ms ($p < 0.01$), which was 8% of the result averaged from the expert cohort.

Table 2-4. Performance of the QRS delineation and measurement algorithm

Measurement type	Parameter [A]	QRS onset	QRS offset	QRSd
Array-specific ($n = 100$)	Mean ± Std.	3.2 ± 13.6	0.3 ± 15.6	–2.8 ± 21.7
	|Mean| ± |Std.|	10.0 ± 9.8	10.3 ± 11.7	16.6 ± 14.3
	|Median|	8.5	7.5	14.0
	[|Q1|, |Q3|]	[4.0, 12.0]	[4.0, 12.0]	[7.0, 20.0]
Global ($n = 50$)	Mean ± Std.	6.0 ± 9.9	–3.9 ± 7.5	–8.6 ± 12.4
	|Mean| ± |Std.|	8.0 ± 8.3	7.0 ± 4.7	11.6 ± 9.6
	|Median|	7.0	6.0	10.0
	[|Q1|, |Q3|]	[3.0, 11.0]	[4.0, 9.8]	[5.0, 16.0]

[A] Parameters reported are mean signed or absolute (indicated by | |) error, i.e., the difference between the algorithm result and the averaged result from the expert cohort. Q1 = first quartile; Q3 = third quartile.

Seventy-six percent of algorithm array-specific QRSd values and 88% of algorithm global QRSd values were within 20 ms (half of the smallest precision on a 12-lead ECG grid) of the averaged expert results. The average absolute error for the array-specific QRSd results was significantly less than the error for the global QRSd results ($p = 0.03$). The average absolute errors for anterior and posterior array-specific QRSd results, however, were not significantly different (anterior, 14 ± 12 ms; posterior, 19 ± 15 ms; p = 0.08). The clinical QRSd classifications of the native conduction validation studies as narrow (<120 ms), moderate (120 to 150 ms), or wide (≥150) were the same for the algorithm and the average expert response in 19 of the 20 native conduction validation studies (95%).

QRS complex peak height and expert QRSd were significant predictors of algorithm error for global QRSd ($r2 = 0.21$, $p < 0.01$). Increased complex peak height was associated in the multivariate model with algorithm underestimation of QRSd, while increased average expert QRSd was associated with algorithm overestimation of QRSd.

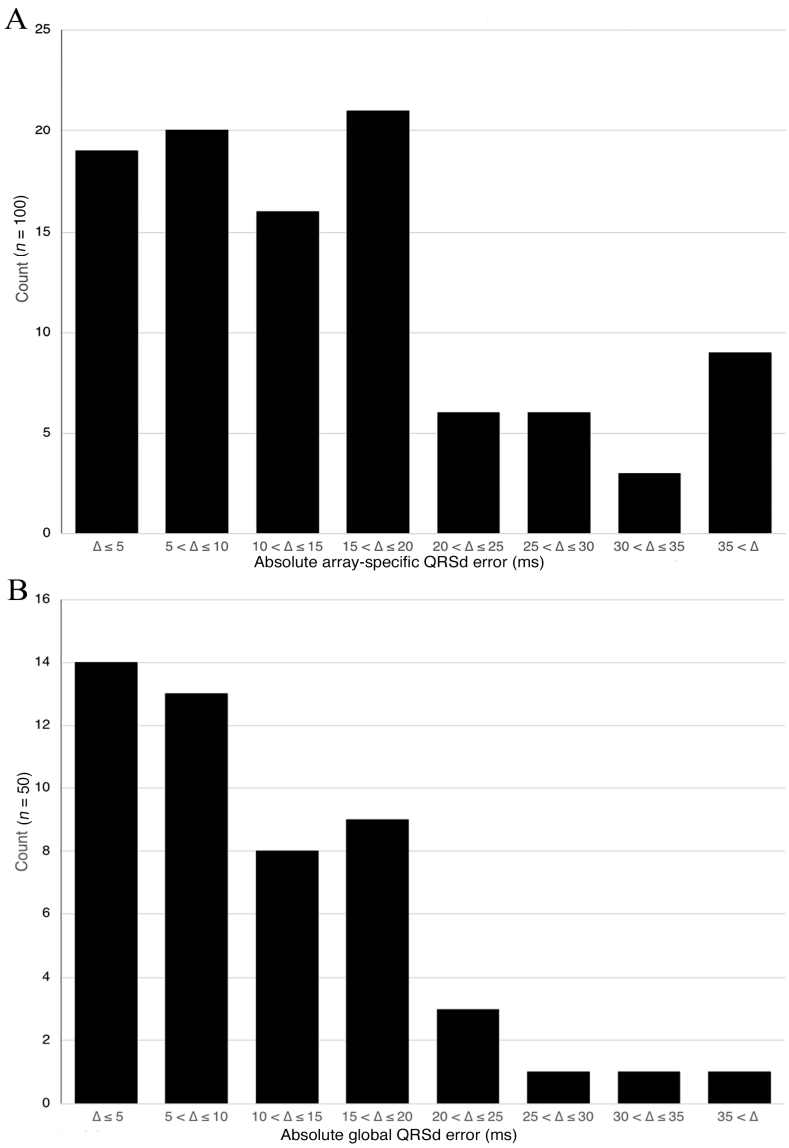

Figure 2-7. Validation study results
Histogram of the absolute error for the algorithm array-specific QRSd values (A) and the algorithm global QRSd values (B). Seventy-six percent of algorithm array-specific QRSd values and 88% of algorithm global QRSd values were within 20 ms of the average expert values.

The interobserver variation data for the experts' responses is shown in Table 2-5. The average standard deviation of the experts' array-specific and global QRS onset and offset results ranged from approximately 6 to 10 ms, while the standard deviations for the array-specific and global QRSd results were both about 15 ms (10%). Increased algorithm error was not associated with increased interobserver differences in the experts' results for either array-specific or global QRSd.

Table 2-5. Performance of the QRS delineation and measurement algorithm

Measurement type	Parameter [A]	QRS onset	QRS offset	QRSd
Array-specific (n = 100)	Mean ± Std.	8.4 ± 7.2	7.9 ± 9.2	15.2 ± 12.0
	Median	5.6	5.4	11.3
	[Q1, Q3]	[3.3, 11.8]	[3.0, 10.1]	[7.0, 19.1]
Global (n = 50)	Mean ± Std.	9.6 ± 7.1	6.4 ± 4.4	15.2 ± 10.1
	Median	7.3	5.3	12.9
	[Q1, Q3]	[3.8, 14.3]	[3.5, 8.6]	[7.5, 19.0]

[A] Parameters reported are mean signed or absolute (indicated by | |) interobserver variation, i.e., the standard deviation of the results of the expert cohort. Q1 = first quartile; Q3 = third quartile.

2.5 Discussion

In this study, we describe a pair of automated real-time algorithms for QRS complex detection and classification and for QRS complex delineation and measurement in MECGs acquired in the HF and/or CRT population, which is characterized (1) by complexes of both negative and positive polarities, large width, and variable amplitudes and (2) by unpredictable and inconsistent variation in complex morphology. We evaluated the performance of these algorithms using MECGs collected in real-world CRT patients and compared the algorithm results with the independently acquired results from two groups of experts. The QRS complex detection algorithm had at least 96% sensitivity and positive

predictivity for QRS complex detection and classification. The accuracy of the QRS delineation and measurement algorithm was close to the interobserver variation in the expert cohort's responses, similar to that of existing single-channel 12-lead ECG algorithms [92], and similar to documented differences in QRSd results between clinical 12-lead ECG machines and manual clinician measurements [93]. The QRSd measurement algorithm clinical classification accuracy was 95% in the 20 native conduction validation studies, which is better than the reported classification agreement between clinical 12-lead ECG machines and doctors [93].

2.5.1 QRS detection algorithm validation

The QRS complex detection algorithm was at least 96% sensitive and had a positive predictivity of at least 97% for both complex detection and classification of PM and OM complexes. No previously published QRS complex detection and/or classification algorithms for MECGs were found in the literature. Reported sensitivity and positive predictivity for single-channel 12-lead ECG algorithms are usually over 99% for QRS complex detection without morphologic classification [76, 92]. Fully automated real-time QRS detectors with morphologic classification (i.e., PVC detectors), however, tend to have positive predictivity and sensitivity values closer to 90% to 95% [76]. These results indicate that our QRS complex detection algorithm performs as well as the current state-of-the-art methods for single-channel 12-lead ECG data in spite of the additional challenges posed by MECGs acquired in the CRT population.

2.5.2 QRSd measurement algorithm validation

As with the QRS complex detection algorithm, no previously developed QRSd measurement algorithms for MECGs were found in the literature. Comparison of algorithm accuracy with the expert cohort's interobserver variation, therefore, may be the best means of assessing the QRSd measurement algorithm's performance. The average absolute algorithm error was approximately 10 ms or less for array-specific and global QRS onset and offset, which is one-fourth of the smallest unit of precision of standard clinical 12-lead ECG grid paper (40 ms). Moreover, the algorithm global QRSd error (11.6 ± 9.6 ms) was substantially less than the interobserver variation in that measurement (15.2 ± 10.1 ms), and the algorithm array-specific QRSd measurement was close to the interobserver variation in that measurement.

Most QRSd measurement algorithms developed for single-channel 12-lead ECG data report QRS onset and offset error. Cesari et al. reported results (absolute average QRS onset difference: 10 ms; absolute average QRS offset difference: 14 ms) similar to ours for an algorithm designed for single-channel 12-lead ECG data and validated with the MIT-BIH database [92]. In addition, our non-absolute average QRS onset and offset errors of 0.3 to 3.2 ms are within the results of other investigators' single-channel 12-lead ECG algorithms, for which the error ranged from 0.1 to 4.6 ms [92].

The QRSd measurement algorithm also performs well when its accuracy is compared with that of current clinical 12-lead ECG machines or the reproducibility of manual QRSd measurements made by clinicians. The average absolute algorithm error of 11.6 ms for our cohort of 20 native conduction and 30 paced MECG recordings is well within the range of

error between a clinical 12-lead ECG machine and a pair of clinicians, as reported by De Pooter et al. (7 ms and 14 ms in native and paced 12-lead ECGs, respectively). De Pooter also reported an 85% or 63% agreement between the expert clinicians and clinical 12-lead ECG machines for the classification of native conduction ECGs as narrow or moderate, respectively. In our study, the agreement between the QRSd measurement algorithm and the average expert result was considerably higher, at 95%. Last, De Guillebon et al. reported that the results of three cardiologists and a clinical 12-lead ECG machine were found to differ by more than 20 ms in 47% of cases [37]. In contrast, 76% of algorithm array-specific QRSd values and 88% of algorithm global QRSd values in our study were within 20 ms of the average expert result.

Ultimately, the QRSd measurement algorithm results are well matched with those of the expert cohort, state-of-the-art single-channel 12-lead ECG algorithms, and variation in current clinical 12-lead ECG measurement techniques.

2.5.3 Limitations

These algorithms have been developed and validated using the ECG Belt investigational body surface mapping system and not validated in another MECG system due to lack of availability. In addition, the QRS complex detection algorithm is designed for dichotomized, and not multi-class, heartbeat classification. This strategy is used to provide as much flexibility as possible in the algorithm and prevent erroneous identification of PM complexes as outliers.

2.5.4 Clinical significance

The paired QRS complex detection and measurement algorithms described herein may be used to accurately identify and analyze the QRS complexes associated with the most prevalent conduction pattern in MECGs acquired in candidates for or patients with CRT pacing. The real-time nature of these algorithms makes them viable for use in a clinical environment. The algorithms described in this paper could be used in the future not only to measure QRS complex duration but also (1) to measure heart rate variability, (2) to evaluate the effectiveness of changes to pacing settings on OM complex burden, (3) to compare the characteristics of the most prevalent conduction pattern with those of anomalous or ectopic behavior, or (4) to measure novel QRS-based metrics of electrical dyssynchrony, such as the QRS integral.

2.6 Conclusions

The paired algorithms described in this study have been specifically designed to overcome the challenges of MECGs and of conduction patterns in the CRT population. The algorithms' QRS complex detection, classification, border delineation, and measurement results have been validated in MECGs against the independently acquired results of an expert cohort and have been found to be within accuracies comparable to those of studies done with clinical 12-lead ECG machines and to the interobserver variation of experts in the field. These methods may be used for real-time analysis and represent a key first step toward implementation of MECG methods for improved characterization of cardiac activation in HF and CRT patients.

2.7 Acknowledgements

This work was supported by funding provided by the Medtronic External Research Program, Medtronic, PLC. Ms. Curtin, Dr. Burns, Dr. Bank, and Dr. Netoff have received funding and consulting payments from Medtronic. Ms. Curtin, Dr. Burns, and Dr. Bank are authors on a patent filing describing this work.

3 Impact of Signal Noise on Body Surface Activation Mapping

3.1 Overview

3.1.1 Introduction

Use of changes in 12-lead electrocardiogram (ECG) QRS duration (QRSd) for cardiac resynchronization therapy (CRT) setting selection has had mixed results, in part because of the extreme interobserver variation in clinical 12-lead ECG QRSd measurements. The standard deviation of body surface activation times (SDAT), calculated from multichannel electrocardiograms (MECGs) acquired with a custom ECG Belt investigational body surface mapping system (see *Methods*) has been shown to be better correlated with patient left ventricular (LV) reverse remodeling outcomes than 12-lead ECG QRSd, and a 10% reduction in SDAT has been successfully used as a cutoff value to classify patients as predicted responders or non-responders to CRT. Previous studies have utilized single-beat SDAT values; and although the SDAT measurement method is not as variable as that of QRSd, there are some factors that may affect the MECGs used to measure SDAT but do not affect 12-lead ECGs. The present study aimed to determine (1) how SDAT reproducibility is affected by loss of electrode-torso contact and (2) if multi-beat averaging can be used to compensate for pseudo-physiologic (PP) noise and physiologic variation in electrical substrate behavior.

3.1.2 Methods

Electrode-loss simulations and multi-beat-averaging analyses used MECGs previously acquired in 20 CRT patients during native conduction and CRT (n = 40). The change in

the viable-electrode subset (i.e., the electrodes with good torso contact) size between recordings acquired in the same patient was measured; loss of up to 10 electrodes from the 53-electrode ECG Belt array was simulated, and the relationships between SDAT reproducibility and (1) viable-electrode subset size and (2) original SDAT value were investigated. The effects of 3-, 5-, and 10-beat averaging on the coefficient of variation (CV) in SDAT were measured, as were any associated increases in analysis time.

3.1.3 Results

The average viable-electrode subset size was 47 electrodes (89% of the total array), which changed by ±8% during data collection. Intra-patient changes in viable-electrode subset size were not correlated with the time between recordings. The change in SDAT with increasing electrode loss was inversely correlated with viable-electrode subset size and original SDAT value. Two recordings had CVs for single-beat SDAT values greater than the previously used 10% SDAT patient classification cutoff value. Ten-beat averaging reduced the average CV in SDAT from 3.0% ± 2.6% with single-beat averaging to 0.4% ± 0.4% and increased analysis time by 10 to 15 seconds, which is the same amount of time required to collect a single standard 12-lead ECG.

3.1.4 Conclusions

Electrode loss and beat-to-beat variability are likely to contribute significantly to observed changes in SDAT values and may confound SDAT-driven CRT setting selection. Electrode loss is unpredictable, affects a large portion of the electrode array, and should be

monitored during MECG acquisition with the ECG Belt; results should be confirmed through repeated recordings. Investigation of the improvement in SDAT reproducibility that may be gained with larger arrays is recommended, and the use of smaller arrays is not supported. Ten-beat averaging is recommended to reduce SDAT variation to an order of magnitude less than the change in SDAT patient classification cutoff value used in previous studies and can be achieved with a negligible increase in analysis time required if recording acquisition protocols are designed accordingly.

3.2 Introduction

This chapter investigates the reproducibility of the standard deviation of body surface activation times (SDAT) derived from multichannel electrocardiograms (MECGs) acquired with a custom ECG Belt investigational body surface mapping system (see *Methods*) and the associated implications for SDAT-driven selection of cardiac resynchronization therapy (CRT) device settings.

In spite of its gold-standard status, use of changes in 12-lead electrocardiogram (ECG) QRS duration (QRSd) to predict patient CRT outcomes has had mixed results, in part because of the extreme interobserver variation in clinical QRSd measurements [36]. A recent study found, for instance, that 47% of 12-lead ECG QRSd values differed by more than 20 ms, or by 16%, when measured by multiple cardiologists and/or a clinical 12-lead ECG machine [37]. The SDAT metric has been investigated as alternative measure of electrical dyssynchrony, and changes in SDAT have been shown to be predictive of CRT patients' chronic left ventricular (LV) reverse remodeling responses to therapy [61, 62]. In

addition, a 10% reduction in SDAT from native conduction to CRT has been used successfully to discriminate predicted responders and non-responders (hereafter the SDAT patient classification cutoff value) [61]. Based on these results, Bank et al. have suggested that identification of the CRT device settings associated with the greatest reduction in electrical dyssynchrony (i.e., SDAT value) may be used to inform CRT device setting optimization and improve patient response [61, 94].

SDAT-driven CRT setting optimization requires reproducible SDAT values to allow inter-setting comparisons. Although, unlike 12-lead ECG QRSd, the calculation of SDAT is based on specific mathematical criteria, MECGs used to calculate SDAT may be affected by a number of factors, some of which are unique. Among these factors is external-source noise, which may be present in unfiltered MECGs but which can readily be removed during preprocessing [95]. Relevant examples of external-source noise are high-frequency electromagnetic interference or low-frequency respiratory noise [95]. Unpredictable alterations to signal amplitude and/or frequency caused by insufficient electrode-torso contact (i.e., electrode loss) during data acquisition can also be identified during data preprocessing; however, these effects cannot be filtered to recover the underlying data. The MECGs may also be affected by noise that falls within the frequency and amplitude ranges of the physiologic activity (i.e., pseudo-physiologic noise [PP noise]), which may be caused by small physical perturbations to the electrode array and which cannot be extracted from the MECGs. Last, there is true physiologic variation in electrical substrate behavior. The appropriate techniques for removing external-source noise are well established. As a

result, this study will focus on how SDAT reproducibility is affected by electrode loss, PP noise, and true physiologic variation.

In CRT and heart failure (HF) patients, electrode loss or PP noise may be caused by patient body habitus or body movement during data acquisition. Patient body habitus may restrict the areas available or suitable for electrode placement because of (1) the lack of circumferential torso surface area in small-framed patients or (2) the lack of level skin surfaces due to the presence of panniculi in patients with high body mass indexes. Patient body movement is often caused by physical ailments that are exacerbated by the supine position that is required for MECG acquisition. Patients with such physical limitations may need to frequently adjust their body positioning, which can cause intermittent variations in the external force on the electrodes as weight is shifted or as a limb makes incidental contact with the electrode array. Electrode loss occurs when the resultant signal disturbances are large, while PP noise is created by smaller fluctuations. Notably, electrode loss is a relatively minor issue for 12-lead ECG acquisition because only 10 electrodes are used, all of which are placed on the patient's anterior, with only 6 electrodes positioned on the torso itself. In addition, electrodes in the ECG Belt array are connected to each other and non-contacting electrodes can pull neighboring electrodes away from the torso.

True physiologic variation in MECGs comes in two forms in CRT patients: large changes in QRS complex morphology due to inconsistent pacing or the presence of ectopic activity and small changes in timing intervals due to heart rate variability (HRV) [95]. Large changes in QRS complex morphology are accounted for and eliminated from SDAT calculations by the QRS complex detection and classification algorithm that is incorporated

in the custom software used for offline analysis of the MECGs acquired with the ECG Belt system [96]. HRV is low during native conduction in HF patients but may be increased by CRT [97]. However, any HRV will be inherently minimized during MECG recording acquisition as a result of the patient's supine position [98].

The effects of electrode loss, PP noise, and HRV on the reproducibility of SDAT have not been investigated; previous studies have utilized single-beat SDAT values [61, 62, 94], and any reproducibility issues affecting SDAT would likely be magnified by the calculation of percent change in SDAT from native conduction to CRT. In addition, although the effects of PP noise or HRV may be mitigated by multi-beat averaging, neither intermittent nor persistent electrode loss can be methodologically compensated for. This study investigates the effects of simulated electrode loss and multi-beat averaging on the reproducibility of SDAT values derived with the investigational ECG Belt body surface mapping system in the context of the previously used SDAT patient classification cutoff value. The results of this study may be used (1) to inform electrode array designs to balance metric reproducibility with resource costs and (2) to inform signal analysis methods to balance metric reproducibility with analysis time and computational costs.

3.3 Methods

3.3.1 Study population

Simulations and analyses were performed using MECGs acquired with a custom ECG Belt investigational body surface mapping system and collected at United Heart and Vascular Clinic in St. Paul, MN, for a previous study of advanced systolic HF patients who

had received new CRT implants between 2014 and 2017[4]. For that study, written informed consent was obtained from all patients, and the study protocol was approved by an institutional review board (IRB). Data was available from 149 patients during native conduction (CRT off) and with CRT on at a range of device settings (i.e., atrioventricular delays, interventricular delays, LV pacing vectors, etc.). MECGs acquired for each patient were collected 5 to 20 minutes apart in a single visit. Patients without intact native conduction were excluded from the analyses in this chapter.

MECGs acquired in 20 randomly selected patients during native conduction and during CRT were used for the electrode-loss simulation studies and multi-beat-averaging analyses.

3.3.2 MECG acquisition

The ECG Belt system has been described elsewhere [61, 62]. Briefly, the investigational system consists of a disposable electrode array, a multichannel amplifier, and a monitor (Heartscape, Verathon, Seattle, WA) and customized data acquisition software (Medtronic, PLC, Minneapolis, MN). The ECG Belt electrode array is composed of 53 unipolar ECG electrodes that wrap around the torso (anterior: 17 electrodes in 2 rows; posterior: 36 electrodes in 4 rows). MECGs for a given condition were collected in a 15- to 20-second recording at a sampling rate of 1 kHz and saved offline for subsequent analyses.

---

[4] Data from this previous prospective study will be used throughout this dissertation. The study in question was initiated and conducted by the research department at United Heart and Vascular Clinic; study funding and equipment were provided by Medtronic, PLC. Initial results from this study were published in Gage et al. [56]

3.3.3 Processing of MECGs

The methods for preprocessing, QRS detection, and SDAT measurement in MECGs have been implemented in comprehensive stand-alone software[5] written in MATLAB (using MATLAB Release 2017b, The MathWorks, Inc., Natick, MA), which is described in detail elsewhere [96] (see Chapter 2). The software supports the loading and serial analysis of data collected during multiple conditions from one or more patients and displays the results with a graphical user interface.

3.3.3.1 Identification of QRS complexes for activation mapping

The QRS complexes associated with the most prevalent conduction pattern ("predominant morphology," or PM complexes) in a given MECG recording are used for the calculation of body surface activation metrics. The method for identifying PM complexes and complexes of outlier morphology (OM complexes) in a recording has been previously explained in great detail [96] (see Chapter 2). For simplicity, heartbeats with PM QRS complexes will be referred to hereafter as PM beats. The body surface activation analyses described below are performed for each PM beat.

3.3.3.2 Definition of viable-electrode subset

After all PM beats have beats have been identified, electrode-torso contact is evaluated over the interval of each associated QRS complex. Electrodes with torso contact that is

[5] The University of Minnesota, Minneapolis, MN, and United Heart and Vascular Clinic, St. Paul, MN

insufficient to maintain signal integrity are removed based on acceptable signal amplitude thresholds, which have been described previously [96]. The viable-electrode subset is then the set of electrodes with sufficient contact across all PM beats in the recording, and their data is used in subsequent analyses. The size of the viable-electrode subset for each MECG recording is reported by the offline MECG analysis software, and electrode with complete loss of torso contact may be identified by flatline signals on the ECG Belt system monitor during data acquisition.

3.3.3.3 Calculation of body surface activation metrics

The methods incorporated into the MECG analysis software for calculating SDAT have been described previously [61, 62]. Briefly, for each ECG, the local body surface activation event is defined, based on an extension of contact mapping principles [71], as the steepest negative slope in the QRS complex. The time associated with the first activation event recorded is designated as time zero, and the delay to each subsequent activation event is the respective local body surface activation time. These activation times are then interpolated to create a pair of anterior and posterior activation maps. Finally, SDAT is the standard deviation of the local body surface activation times. The SDAT metric is calculated using only the local activation times from the viable-electrode subset. The SDAT patient classification cutoff value has been reported previously as the percent change relative to the native-conduction value [61].

3.3.4 Electrode-loss simulations and multi-beat-averaging analyses

The size of the viable-electrode subset was measured for each recording, along with the time between recordings for each patient and any intra-patient change in viable-electrode subset size between recordings. Electrode loss was then simulated by (1) excluding one or more activation times, (2) re-scaling the remaining activation time values to the new minimum activation time, and (3) re-calculating the SDAT. For each case, a total of 200 electrode-loss simulations were performed. The number of randomly excluded activation times ranged from 1 to 10. At each simulated level of loss, the random selection of activation times to be excluded was repeated 20 times.

The percent change and the rate of percent change in SDAT relative to the reference original SDAT value with increasing levels of electrode loss were measured for each recording (averaged across all simulations). The reference original SDAT value was defined as the single-beat SDAT value from the middle beat in each recording with the original viable electrode subset. Percent change, and not absolute (i.e., ms) change, in SDAT was used as the output in these simulations for comparison with previous work. The effects of the original viable-electrode subset size and of the original SDAT value on the rate of percent change in SDAT were also assessed. For that analysis, recordings were grouped by viable-electrode subset size in 5-electrode increments and by original SDAT value in 5-ms increments.

3.3.5 Multi-beat-averaging analyses

For the purposes of this study, multi-beat averaging consisted of averaging SDAT values calculated from multiple PM heartbeats. The following steps were performed for all 40 MECG recordings. First, the intra-recording beat-to-beat range of SDAT values was measured. Second, the SDAT values from all possible combinations of PM beats within each recording were averaged using an *n*-choose-*k* approach for *k* values of 1, 3, 5, and 10 beats. The coefficient of variation (CV) in SDAT at each level of multi-beat averaging was calculated for each recording and reported as a percentage. In addition, the time associated with SDAT calculation and averaging for each level of multi-beat averaging was recorded.

3.3.6 Statistics

Data are expressed as means ± standard deviations. Student's unpaired *t*-test or a one-way analysis of variance (ANOVA) combined with multiple pairwise comparisons using Tukey's difference criterion was used to analyze unpaired data. The slope of a univariate linear regression line was used to approximate the rate of percent change in SDAT with increasing levels of electrode loss for each case. Multivariate regression using backward stepwise elimination until all variables had a p value of <0.10 was subsequently used to identify significant predictors of the rate of change in SDAT. A p-value of <0.05 was considered significant for all other analyses. All statistical analyses were performed using MATLAB.

3.4 Results

3.4.1 Electrode-loss simulations

The details of the 40 recordings used for the electrode-loss simulations (and the multi-beat-averaging analyses; see below) are presented in Table 3-1. Recordings for each patient are listed in the order in which they were acquired. The average number of viable electrodes was 47 ± 3 electrodes (i.e., 89% of the 53 total electrode array), the average time between recordings for each patient was 7 ± 4 minutes, and the average change in the size of the viable-electrode subset between recordings for a given patient was 4 ± 2 electrodes. The viable-electrode subset size decreased between recordings for 11 (55%) patients. Change in the size of the viable-electrode array was not correlated with the time between recordings.

Table 3-1. Recordings used for simulations and analyses

Pt.	Condition	VE (*n*) [A]	Time (min)	Δ VE (*n*) [A]	PM beats (*n*)	SDAT (ms) [A]
1	BiV	45	2	6	11	31.5 ± 1.8
	Native	51			9	33.3 ± 0.2
2	Native	43	1	2	10	34.4 ± 0.3
	LV-only	45			12	26.3 ± 1.2
3	Native	47	3	–6	9	25.9 ± 1.1
	LV-only	41			12	27.3 ± 2.8
4	LV-only	45	3	–1	10	31.0 ± 0.7
	Native	44			8	47.7 ± 0.6
5	BiV	41	8	–1	16	25.9 ± 1.4
	Native	40			9	26.3 ± 1.2
6	LV-only	46	2	2	8	22.4 ± 0.9
	Native	48			12	24.3 ± 0.5
7	BiV	47	9	1	15	27.8 ± 1.3
	Native	48			12	26.9 ± 0.4
8	BIV	47	14	2	15	25.3 ± 0.2
	Native	49			14	31.2 ± 0.4
9	BiV	45	6	2	13	45.0 ± 0.4
	Native	47			12	30.6 ± 0.1
10	LV-only	51	4	–3	12	29.8 ± 0.7
	Native	48			10	31.6 ± 0.6
11	LV-only	49	9	1	12	30.2 ± 0.6
	Native	50			13	34.2 ± 0.4
12	LV-only	49	8	–8	16	23.5 ± 0.7
	Native	41			11	32.2 ± 0.7
13	LV-only	51	11	–6	10	22.6 ± 0.3
	Native	45			10	31.2 ± 0.2
14	BiV	50	3	–1	11	25.0 ± 3.0
	Native	49			8	34.4 ± 0.9
15	BiV	46	6	6	12	25.8 ± 1.4
	Native	52			12	49.9 ± 0.3
16	Native	49	6	–5	17	33.9 ± 0.3
	LV-only	44			16	23.6 ± 0.7
17	Native	45	5	3	14	41.8 ± 0.4
	LV-only	42			14	32.6 ± 2.2
18	BiV	46	9	5	16	32.1 ± 0.9
	Native	51			11	51.2 ± 0.7
19	BiV	47	1	1	9	22.2 ± 1.6
	Native	48			11	25.2 ± 0.3
20	BiV	51	4	–7	10	26.3 ± 0.4
	Native	44			12	27.5 ± 1.3

[A] VE = viable electrode; All-beats average SDAT.

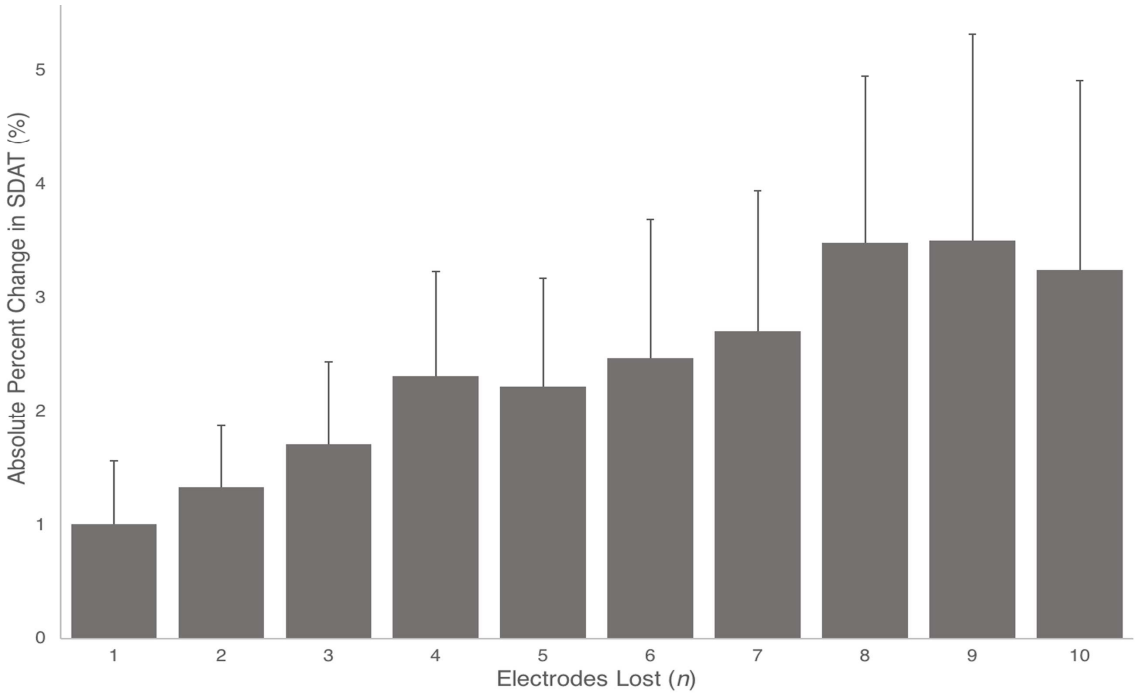

Figure 3-1. Change in SDAT for electrode-loss simulations
The average (across all recordings and simulations) absolute value of percent change in SDAT with increasing simulated levels of electrode loss. Standard deviation is indicated by vertical bars. No level of simulated electrode loss was associated with an average absolute value of percent change in SDAT of greater than 5%.

Figure 3-1 shows the percent change in SDAT (averaged across all recordings and simulations) as the simulated level of electrode loss increased. No level of simulated electrode loss was associated with an average SDAT change of greater than 5% although increased electrode loss was associated with a larger range in absolute percent change in SDAT values.

The average rate of change in SDAT for the 40 recordings used in the simulations was 0.3% ± 0.1% with each electrode lost. Figure 3-2A shows the percent change in SDAT versus the proportion of electrodes lost, broken down by the original size of the viable-electrode subset. The rate of change in SDAT increased with decreasing viable-electrode subset size. The average rate of change for cases with 40 to 45 viable electrodes was 1.4

times that of cases with 50 or more viable electrodes ($p < 0.05$; see Table 3-2 for details). A similar phenomenon was seen with respect to low versus high original SDAT values, as shown in Figure 3-2B. Recordings with original SDAT values between 20 and 25 ms exhibited an average rate of change in SDAT that was almost twice that of the cases with an original SDAT of 40 ms or more ($p = 0.06$; see Table 3-2 for details). Notably, when the absolute (i.e., ms) change in SDAT was used, the rate of change in SDAT did not differ between recordings grouped based on the original SDAT value (results not shown).

As suggested by the data in Figure 3-2, the multivariate regression showed that viable-electrode subset size and original SDAT value were both significant, inversely correlated predictors of the rate of change in SDAT with increasing levels of electrode loss ($r^2 = 0.25$, $p < 0.01$).

Table 3-2. Effectors of rate of change in SDAT

Comparison type	Group	*N*	Rate of change [A]	r^2	*p*-value
Size of viable-electrode subset	40 to 45 electrodes	9 (22%)	0.15	0.93	<0.01
	45 to 50 electrodes	23 (58%)	0.13	0.92	<0.01
	≥50 electrodes	8 (20%)	0.11	0.91	<0.01
Original SDAT value	20 to 25 ms	7 (18%)	0.39	0.94	<0.01
	25 to 30 ms	15 (38%)	0.29	0.92	<0.01
	30 to 35 ms	13 (32%)	0.24	0.92	<0.01
	≥40 ms	5 (12%)	0.21	0.88	<0.01

[A] Percent change in SDAT per number of viable electrodes lost.

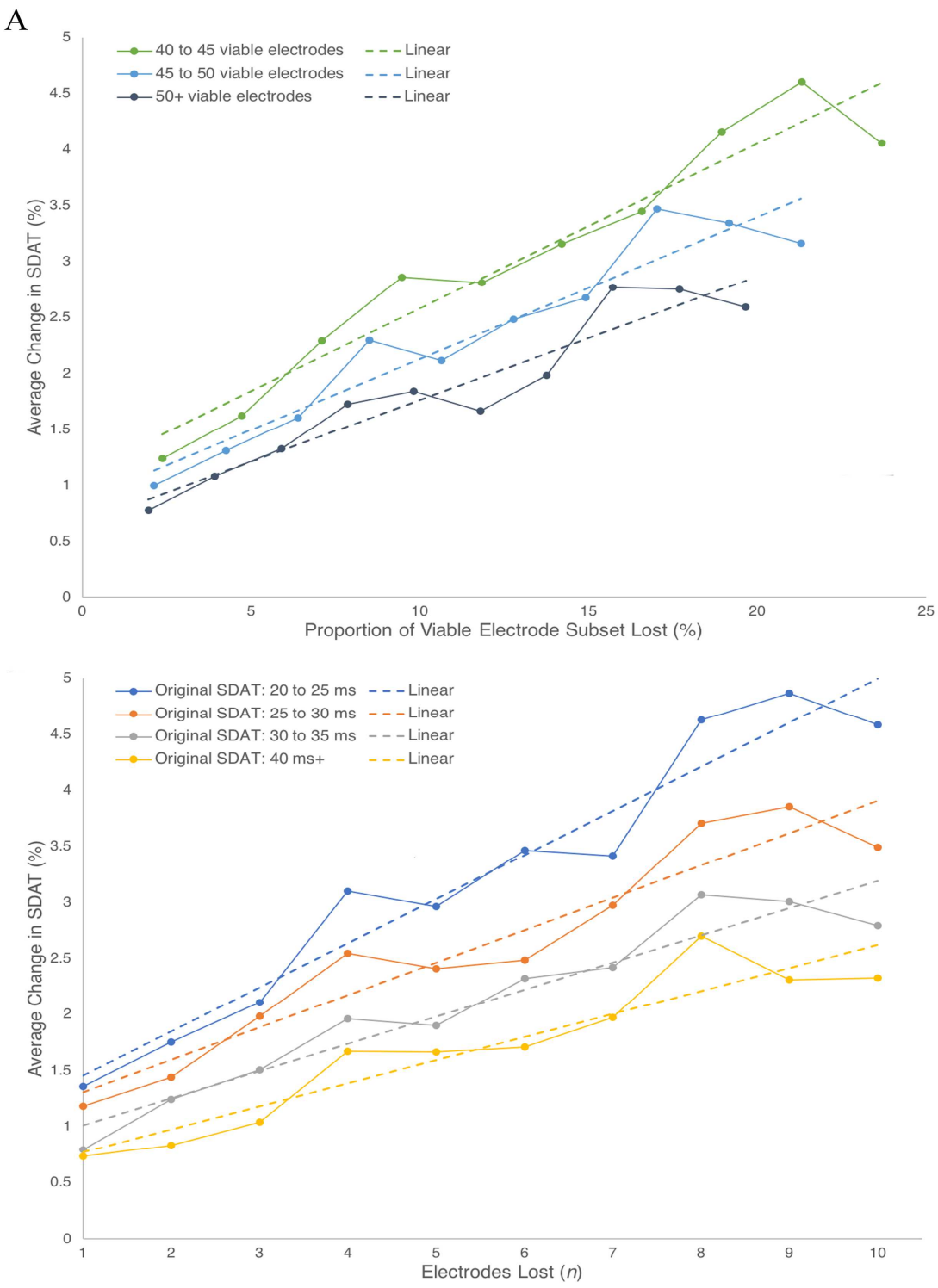

Figure 3-2. Effectors of rate of change in SDAT
The absolute value of percent change in SDAT with increasing simulated levels of electrode loss broken down by the original size of the viable-electrode subset (A) and by the original SDAT value (B). The rate of change in SDAT was largest for small viable-electrode subsets and low original SDAT values.

3.4.2 Multi-beat-averaging analyses

The same recordings used for the electrode-loss simulations were used for the multi-beat-averaging analyses (see Table 3-1). The average number of PM beats in a recording was 12 ± 2 beats, and the all-recordings all-beats average SDAT calculated from the complete viable-electrode subset was 33.4 ± 14.7 ms. SDAT calculation required 1 to 1.5 seconds for every beat included in the multi-beat average. In addition, 33 (83%) of the recordings had at least 10 PM beats present, but only 12 patients (60%) had at least 10 PM beats present in both the native conduction and the CRT recordings.

Figure 3-3 shows the all-recordings average CV in SDAT (reported as a percentage) at each level of multi-beat averaging and the observed inter-recording range of this variation (i.e., the standard deviations of the CVs in SDAT). The average CV for single-beat SDAT values was 3.0% ± 2.6%. The CV decreased with increasing levels of multi-beat averaging: 3-, 5-, and 10-beat averaging resulted in CVs of 1.5% ± 1.3%, 1.0% ± 0.9%, and 0.4% ± 0.4%, respectively. For two recordings (5%), both acquired during CRT, the CV for single-beat SDAT values was greater than the SDAT patient classification cutoff value of 10%, while the maximum CV in SDAT for 10-beat averaging was 1.3% (n = 33). Notably, the average CV in SDAT was significantly smaller in the native conduction recordings (1.8% ± 1.3%) than in the CRT recordings (4.3% ± 3.0%; $p < 0.01$). The average SDAT value was also significantly larger, however, for the native conduction recordings (33.7 ± 8.0 ms) than for the CRT recordings (27.8 ± 5.2 ms, $p < 0.01$).

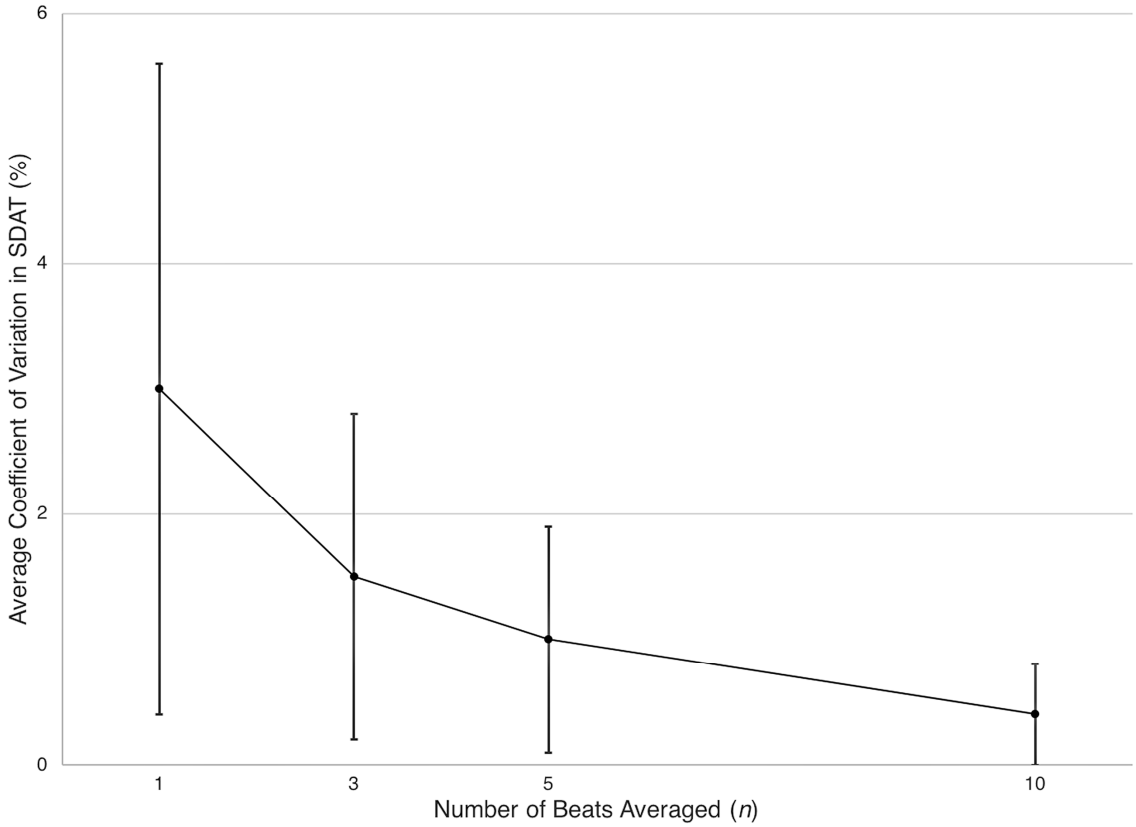

Figure 3-3. Coefficients of variation in multi-beat average SDAT values
The all-recordings average CV in SDAT (reported as a percent) at each level of multi-beat averaging (circular data points) and the expected extent of this variation (i.e., standard deviation the CV in SDAT) (shaded). Use of 10-beat averaging reduced the average CV in SDAT from 3% (single-beat SDAT values) to 0.4%.

3.5 Discussion

In this study, electrode-loss simulations and multi-beat-averaging analyses were used to investigate the effects of electrode loss, PP noise, and HRV on the reproducibility of the body surface activation metric SDAT and to determine the scale of these effects in the context of future SDAT-driven selection of CRT settings. The electrode-loss simulation studies showed (1) that electrode loss affects on average 11% of the array and can change, unpredictably, by 8% during data collection and (2) that while the rate of SDAT change with increasing electrode loss was low, it was inversely correlated with both original

viable-electrode subset size and original SDAT value. In addition, multi-beat-averaging analyses indicated that 10-beat averaging could reduce the CV for single-beat SDAT values by 87% and the previously used SDAT patient classification cutoff value by one order of magnitude.

3.5.1 Electrode-loss simulations

The average viable-electrode subset size in this study represented 89% of all possible electrodes available (i.e., 47 electrodes) with the ECG Belt system. Moreover, the viable-electrode subset changed by 4 ± 2 electrodes, or 8% of all possible electrodes, between recordings for a given patient. When considered in tandem with the relationship between rate of SDAT change and viable-electrode subset size, these results indicate that inter-recording changes in viable-electrode subset size cause changes in SDAT values that vary considerably between patients and/or recordings and may be substantial relative to the SDAT patient classification cutoff value of 10%. In a patient such as number 14, for example, whose viable electrode subset only decreased by 1 electrode between recordings, the change in SDAT for repeated recordings would be less than 1 percent. In contrast, in patient number 12, whose viable electrode subset decreased from 49 electrodes to 41 electrodes between recordings, the change in SDAT for repeated recordings may be 4% or greater.

As the electrode loss data shows, electrode loss may affect a significant portion of the ECG Belt electrodes. In addition, electrode loss is not readily predictable based on the duration of electrode application (i.e., time between recordings). There are, however, no

built-in mechanisms for altering the ECG Belt electrode array to improve electrode-torso contact. In addition, unlike the 12-lead ECG electrodes, placement of the ECG Belt electrode array is not determined by any anatomical landmarks. As a result, efforts to adjust the array improve patient comfort may create further impediments to electrode-torso contact. The presence of any flatline signals reported by the ECG Belt system monitor should be examined throughout data collection, and repeated collection of MECGs at the same CRT settings should be performed to confirm results. These steps will allow a more informed evaluation of changes in SDAT values observed at different CRT settings.

The multivariate analysis results suggest that SDAT reproducibility may be worst in what could be considered the most clinically significant circumstances for CRT optimization. The effects of small viable-electrode subset size on SDAT reproducibility were compounded by low SDAT values, which occur during highly synchronous conduction activity (i.e., during optimized CRT pacing). These results are likely due to the use of percent change in SDAT to quantify electrode-loss effects, as evidenced by the finding that the absolute change in SDAT was not significantly different between recordings grouped by original SDAT value. The use of percent change in SDAT, however, was motivated by its use as an outcome measure in a previous study of the relationship between change in SDAT and patient CRT outcomes [61].

Ultimately, the electrode-loss simulation results highlight the need for vigilance during data collection and confirmation of results, particularly when poor electrode-torso contact is apparent. Notably, electrode loss is an issue that would be expected to affect most MECG electrode arrays, and particularly those with posterior electrodes, but is a relatively minor

issue for 12-lead ECG acquisition. In addition, these results suggest that any resource management benefits of using arrays with fewer electrodes are likely outweighed by the concomitant reduction in SDAT reproducibility and also do not support limiting the size of the electrode array to its current design. Finally, the impact of using absolute change in SDAT to predict patient CRT outcomes should be investigated as another means of improving metric reproducibility.

3.5.2 Multi-beat-averaging analyses

The multi-beat-averaging analyses demonstrated that the effects of PP noise and physiologic single-beat intra-recording variation on SDAT reproducibility are generally moderate (3.0% ± 2.6%) although two recordings had CVs for single-beat SDAT values that were greater than the SDAT patient classification cutoff value of 10%. In contrast, 10-beat averaging reduced the average CV in SDAT by 87%, was associated with the largest stepwise reduction in the average CV (a 60% reduction compared to the CV with 5-beat averaging), and had a maximum CV in SDAT values of only 1.3%. Notably, the lower SDAT values seen during CRT in this study, which are expected due to the correction of some or all of the dyssynchrony associated with the native electrical substrate behavior [61], were associated with SDAT CV values that were more than twice those of native conduction recordings. This result was likely due to the CV calculation method and not a true increase in beat-to-beat variation with CRT pacing.

The improved SDAT reproducibility seen with 10-beat averaging was associated with a 10- to 15-second cost, which is the same amount of time required to collect a standard

12-lead ECG. For ECG Belt data collection at 20 standard CRT device settings, 10-beat averaging would result in an increase of 5 minutes to the total time required of the patient and clinic personnel. This minor increase in resources required is supported by the scale of the improvement in SDAT reproducibility. Notably, 10 or more PM beats were present in only 83% of the recordings used in this study; future data collection protocols should recommend recording 20 to 30 seconds of MECGs to ensure that the quantity of PM beats captured is sufficient for calculating multi-beat-average SDAT values even in cases of patients with premature ventricular contractions or other anomalous conduction activity. Although use of 10-beat-average SDAT values will improve confidence in the SDAT measurement, further analyses in a larger patient population may be necessary to elucidate the relationship(s) between 10-beat-average SDAT values and patient CRT outcomes.

3.5.3 Limitations

The viable-electrode subsets used in the electrode-loss simulations and in the multi-beat-averaging analyses represent the worst-case loss of electrode-torso contact for each recording because the subset was based on electrode contact across all beats. This approach was used because of the design of the offline MECG analysis software. An alternative method would be to define the viable-electrode subset on a beat-by-beat basis.

3.6 Conclusions

Both electrode-loss and beat-to-beat variations affect SDAT reproducibility at a level that is relevant to future SDAT-driven CRT setting selection. Electrode loss is

unpredictable and has effects on SDAT reproducibility that are of a scale relevant to the previously used SDAT patient classification cutoff value. Electrode-torso contact should be monitored during data collection, and use of smaller ECG electrode arrays is discouraged. Beat-to-beat variations can be successfully compensated for with multi-beat averaging using 10 beats to achieve reproducible SDAT results, but data acquisition protocols must be designed to ensure that the quantity of PM beats captured is sufficient.

4 Use of Mapped Body Surface Activation Sequences to Identify LBBB-Like Activation in IVCD Patients: A Pilot Study

4.1 Overview

4.1.1 Introduction

A 12-lead electrocardiogram (ECG) left bundle branch block (LBBB) QRS complex morphology is a key component of cardiac resynchronization therapy (CRT) implant guidelines because of its strong association with response to the therapy. Outcomes in patients with nonspecific intraventricular conduction delays (IVCD), however, are less well known. The presence of an LBBB-like IVCD subpopulation that would benefit from CRT has been suggested by multiple studies, but the relevant characteristics of LBBB-like IVCD patients and the means to identify them remain unclear. This study investigated (1) if mapped body surface activation sequences can be used to identify LBBB-like IVCD patients and (2) if IVCD patients with LBBB-like activation sequences have greater dyssynchrony than those without.

4.1.2 Methods

Body surface activation sequences in 85 CRT patients were mapped using multichannel electrocardiograms (MECGs) acquired with an investigational body surface mapping system. Grouping of mapped body surface activation sequences was performed using manual comparisons between and within 12-lead ECG morphological groups. Activation dyssynchrony was quantified by MECG QRS duration (QRSd), body surface activation duration (BSAd), and the standard deviation of activation times (SDAT). The

dyssynchrony of any IVCD patients that were assigned to groups that consisted mainly of LBBB patients was compared to the dyssynchrony of IVCD patients who were assigned to other groups or who were unclassifiable.

4.1.3 Results

The mapped body surface activation sequences of LBBB and right bundle branch block (RBBB) patients were distinct. The majority (59%, $n = 4$) of IVCD patients had LBBB-associated activation sequences, and these patients had more dyssynchrony by BSAd ($p = 0.08$) and SDAT ($p = 0.01$) than other IVCD patients in spite of similar 12-lead ECG QRSd and MECG QRSd values ($p = 0.24$ and 0.68, respectively).

4.1.4 Conclusion

Mapped body surface activation sequences may be used to identify LBBB-like IVCD patients, and these patients have more dyssynchrony than other IVCD patients and may be better candidates for CRT. Further studies are warranted to define and evaluate an LBBB-like body surface activation sequence based on a larger patient population for which patient CRT outcomes are available.

4.2 Introduction

This chapter preliminarily investigates whether body surface activation maps and metrics can be used to characterize the inter-patient variation in the electrical activation

sequences of cardiac resynchronization therapy (CRT) patients with nonspecific intraventricular conduction delays (IVCD).

Approximately 30% of CRT patients have a 12-lead electrocardiogram (ECG) IVCD QRS complex morphology (i.e., neither left bundle branch block [LBBB] nor right bundle branch block [RBBB]) [42]. The benefit of CRT in this population has varied in multicenter studies and remains, on the whole, uncertain [34, 39, 42]. Notably, the IVCD diagnosis is one of exclusion and therefore results in a population that is more heterogeneous than the LBBB or RBBB population [42]. In spite of the mixed responses of the IVCD population as a whole, there is evidence of an LBBB-like subgroup of IVCD patients who have more dyssynchrony than other IVCD patients and who are therefore more likely to respond to CRT [42, 51, 99]. *Post hoc* analyses of IVCD CRT patients have found that IVCD patients who improve clinically with CRT have more native conduction dyssynchrony than IVCD patients who do not respond to therapy [51]. However, attempts to proactively identify LBBB-like IVCD patients using 12-lead ECG QRS complex features have used inconsistent subsets of the 12-lead ECG LBBB criteria without a clear physiologic basis [99], and the problem is further complicated by use of inconsistent LBBB criteria across multicenter studies and frequent guideline revisions [8, 39, 51, 100].

In addition to the absence of discriminatory 12-lead ECG features, there are no other noninvasively acquired metrics that have been used to successfully prospectively identify electrical substrate behavior that is sufficiently LBBB-like to suggest patient response to CRT. The goal of the current work was to preliminarily determine (1) if mapped body surface activation sequences can be used to identify LBBB-like IVCD patients and (2) if

IVCD patients with LBBB-like activation sequences have greater dyssynchrony than other IVCD patients based on body surface activation metrics. Body surface activation metrics have previously been shown to be sensitive to electrical substrate behavior [61, 62, 94], but the clinical relevance of body surface activation maps has not been studied.

4.3 Methods

4.3.1 Study population

This analysis used 12-lead ECGs and multichannel electrocardiograms (MECGs) collected for a previous study of first-time CRT recipients at United Heart and Vascular Clinic (UHVC) in St. Paul, MN[6]. For that study, written informed consent was obtained from all patients, and the study protocol was approved by an institutional review board (IRB). Inclusion criteria for the analysis in this chapter were a QRSd of ≥120 ms, intact native conduction, and sinus rhythm.

4.3.2 12-lead ECG and MECG acquisition

12-Lead ECGs were collected during native conduction (CRT off), and QRSd was determined by measuring the QRS width in the lead with the widest complex, which is the standard clinical practice at UHVC. Moderate QRSd values were defined as 120 ms to <150 ms, and wide QRSd values were defined as ≥150 ms.

[6] Data from this previous prospective study will be used throughout this dissertation. The study in question was initiated and conducted by the research department at United Heart and Vascular Clinic; study funding and equipment were provided by Medtronic, PLC. Initial results from this study were published in Gage et al. [56]

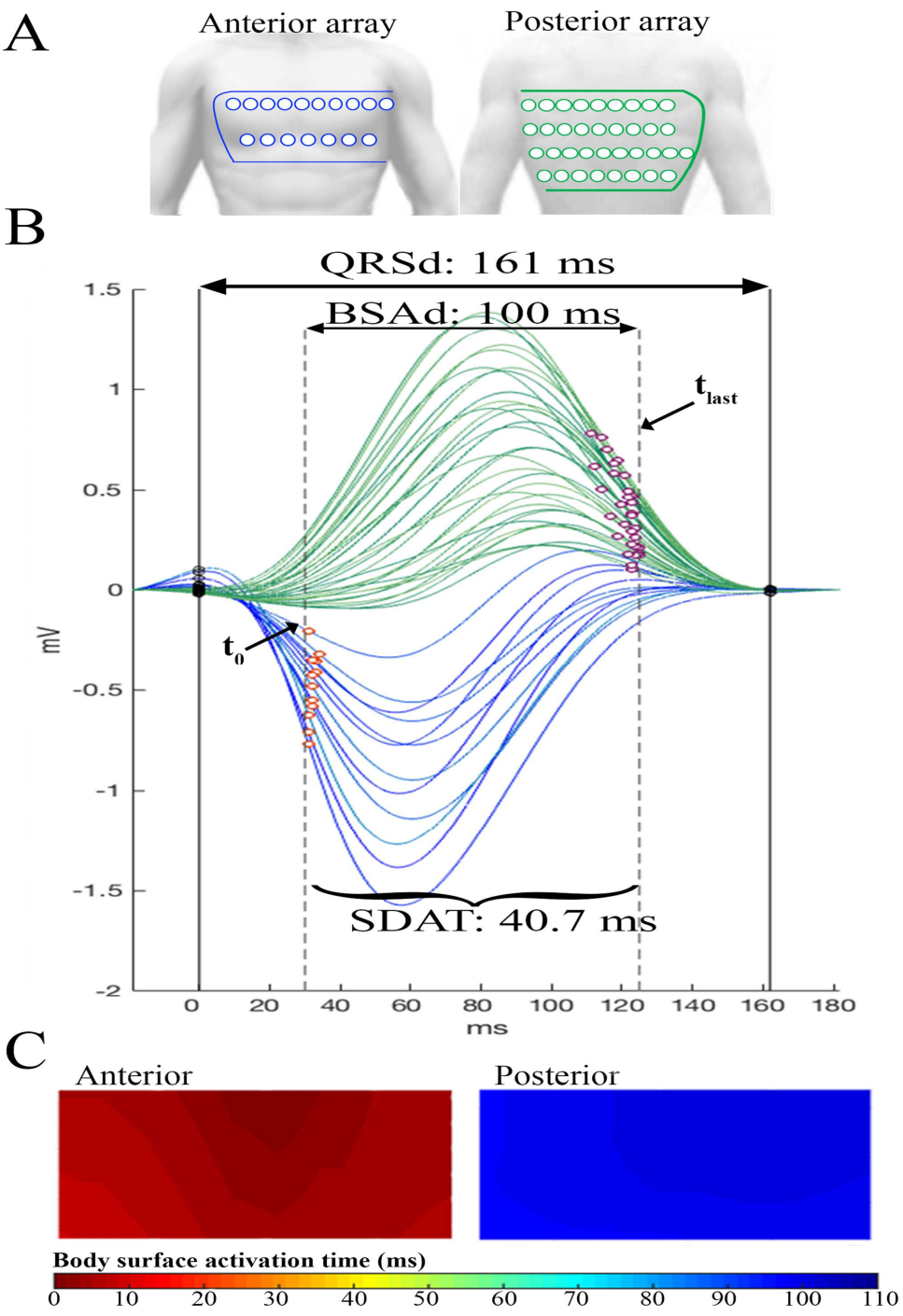

Figure 4-1. MECGs used for calculation of body surface activation metrics
(A) Placement of the anterior (left) and posterior (right) electrode arrays. (B) MECG QRS complex and BSAd interval borders are marked with solid and dashed lines, respectively. Anterior and posterior array ECGs recorded in a sample patient are shown with body surface activation events marked with orange and purple circles, respectively. (C) The body surface activation maps generated based on the data presented in panel B. Maps are presented as anterior and posterior and are displayed with anatomical right-to-left and left-to-right orientations, respectively.

MECGs were collected during native conduction using a custom ECG Belt investigational body surface mapping system, which has been described in detail previously [61, 62]. The investigational system consists of a multichannel amplifier, a monitor, and electrode array (Heartscape, Verathon, Seattle, WA) and customized data acquisition software (Medtronic, PLC, Minneapolis, MN). The ECG Belt electrode array is composed of 53 unipolar ECG electrodes, split into anterior (17 electrodes in two rows) and posterior (36 electrodes in four rows) arrays, which are placed around the patient's upper torso (Figure 4-1A).

The methods for offline analysis and QRS complex detection in MECGs acquired with the ECG Belt investigational body surface mapping system have been implemented in comprehensive stand-alone software[7] written in MATLAB (using MATLAB Release 2017b, The MathWorks, Inc., Natick, MA) and are described in detail elsewhere [96, 101] (see Chapter 2). The software supports the loading and serial analysis of MECGs collected during multiple conditions from one or more patients, displays the results with a graphical user interface, creates the associated body surface activation maps, and performs all of the requisite calculations to determine the metrics defined subsequently.

Dyssynchrony of the mapped activation sequences was quantified by MECG QRSd, body surface activation duration (BSAd), and the standard deviation of activation times (SDAT), as illustrated in Figure 4-1B. MECG QRSd is measured globally from the earliest ECG onset to the latest ECG offset of the QRS complex across all 53 ECGs [91]. For each

[7] The University of Minnesota, Minneapolis, MN, and United Heart and Vascular Clinic, St. Paul, MN

ECG, the local body surface activation event is defined, based on an extension of contact mapping principles [71], as the steepest negative slope in the QRS complex. The time associated with the first activation event captured by the arrays is designated as time zero, and the delay to each subsequent activation event is the respective local body surface activation time. The overall temporal activation sequence is then mapped by interpolating the activation times and creating a pair of anterior (left) and posterior (right) activation maps (Figure 4-1C). BSAd is the time between the first and the last local activation events, and SDAT is the standard deviation of the activation times.

4.3.3 Grouping of patients by mapped body surface activation sequence

Grouping of mapped body surface activation sequences was performed using manual comparisons between and within 12-lead ECG morphological groups. Grouping criteria were the size (i.e. portion of the map) and location (i.e. right or left and anterior or posterior) of any late-activated region(s). A late-activated region was defined as a region activated at least 50 ms after adjacent map areas, based on the definition of a region of conduction block from Jia et al. [64]. Grouping focused on the relative sequence of mapped activation events and not on the extent of the delays in any late-activated regions.

The grouping process consisted of three stages, as illustrated in Figure 4-2. First, the activation sequences of patients with the same 12-lead ECG morphology (LBBB or RBBB), based on the MADIT-CRT guidelines [99], were compared and grouped according to the criteria described above. If the activation sequence of a given patient did not match any of the groups created from the other patients with the same 12-lead ECG morphology,

the maps of that patient were set aside for later analysis. Second, after groups had been defined for the RBBB and LBBB patients, the activation sequences of the IVCD patients were compared with those of the existing groups and placed accordingly. Additional IVCD-specific groups were created as needed. Third, patients of any 12-lead ECG morphology with maps that were not assigned to a group after these two steps were designated "unclassified."

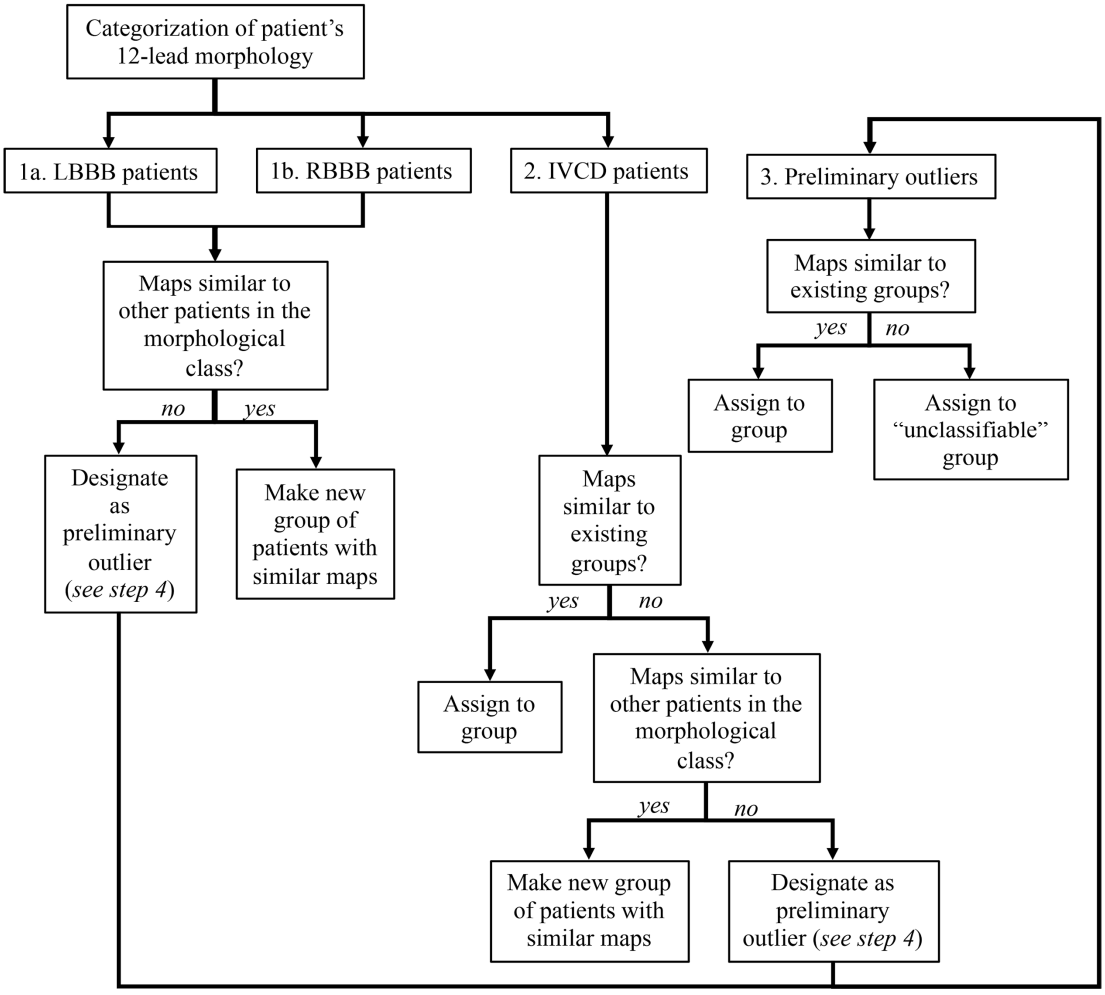

Figure 4-2. Approach for grouping of mapped body surface activation sequences
Similar maps were identified based on the size (i.e. portion of the map) and location (i.e. right or left and anterior or posterior) of any late-activated region(s). A substantial delay was defined as a region activated at least 50 ms after adjacent map areas, based on the definition of a region of conduction block from Jia et al. [64].

The mapped activation sequences of LBBB and RBBB patients with classifiable maps were compared to evaluate the relationship between the established physiologic substrate behaviors associated with the LBBB and RBBB pathologies and the mapped body surface activation sequences. The dyssynchrony (i.e., MECG QRSd, BSAd, and SDAT values) of any IVCD patients who were assigned to groups that were made up of mainly LBBB patients (i.e., groups corresponding to LBBB-associated sequences) was compared to the dyssynchrony of IVCD patients who were assigned to other groups or who were unclassifiable.

4.3.4 Statistics

Data are expressed as means ± standard deviations. Student's unpaired *t*-test or a one-way analysis of variance (ANOVA) combined with multiple pairwise comparisons using Tukey's difference criterion was used to analyze unpaired data. All statistical analyses were performed using MATLAB. A *p*-value of less than 0.05 was considered significant.

4.4 Results

4.4.1 Study population

The clinical characteristics of the 85 patients studied are presented in Table 4-1. The average ejection fraction was 27% ± 7%, the average 12-lead ECG QRSd was 152 ± 18 ms, 72% had an LBBB by 12-lead ECG, and 20% had an IVCD by 12-lead ECG.

Table 4-1. Clinical characteristics of the study population

Characteristic [A]	Value (*n*=85)
Age (years)	70 ± 11
Male (%)	71
Ischemic (%)	46
NYHA Class III (%)	64
ACEI/ARB (%)	92
β-blocker (%)	95
BMI (kg/m^2)	29 ± 6
LVESV (mL)	128 ± 61
EF (%)	27 ± 7
QRSd (ms)	152 ± 18
Wide QRS (≥150ms) (%)	54
LBBB (n(%))	61 (72)
RBBB (n(%))	7 (8)
IVCD (n(%))	17 (20)

[A] NYHA = New York Heart Association; ACEI/ARB = angiotensin-converting enzyme inhibitor/angiotensin II receptor blocker; BMI = body mass index; LVESV = left ventricular end-systolic volume; EF = ejection fraction.

4.4.2 Grouping of patients by mapped body surface activation sequence

The mapped native conduction body surface activation sequences of the 85 CRT patients in this study fell into five distinct groups, which are illustrated in Figure 4-3. There were three LBBB-associated groups, one RBBB-associated group, and one IVCD-only group. Figure 4-4 shows the number of LBBB, RBBB, and IVCD patients belonging to each activation sequence group. Seven patients (3 LBBB, 2 RBBB, and 2 IVCD patients) displayed unique, unclassifiable activation sequences.

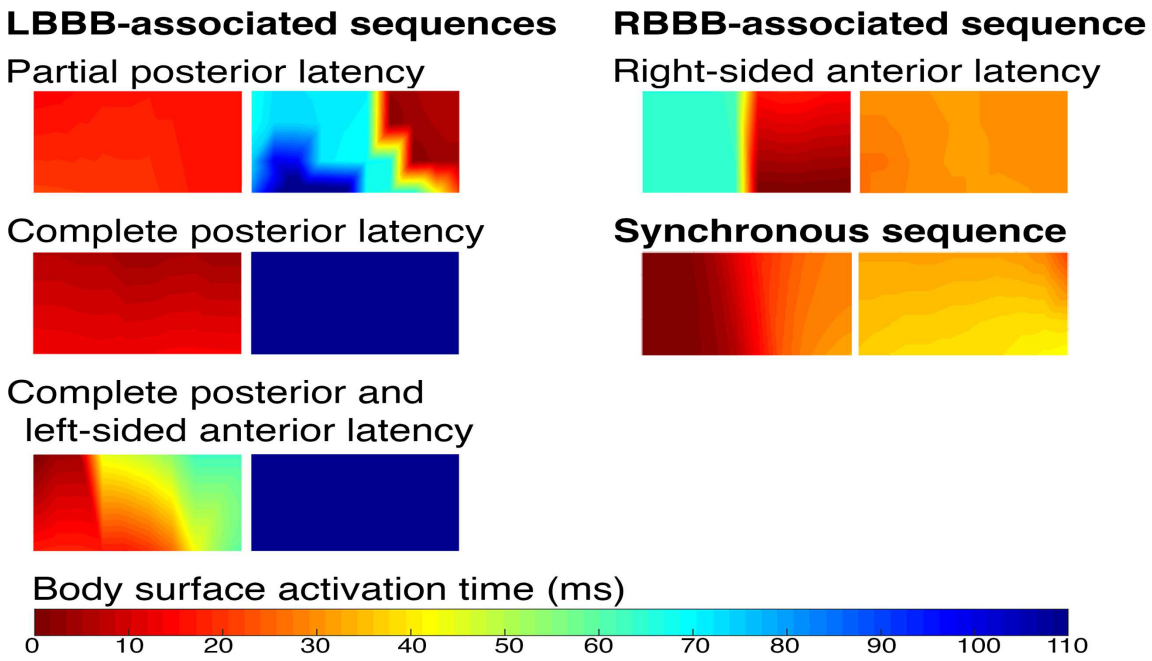

Figure 4-3. Sample activation maps for activation sequence groups
Paired anterior (left) and posterior (right) maps are shown for each group. The LBBB-associated map sequences were characterized by partial or complete posterior delay. The RBBB-associated map sequence had significant delay limited to the right anterior. A few IVCD patients presented with relatively synchronous activation.

4.4.2.1 LBBB and RBBB patients

All LBBB patients had activation sequences characterized by a substantial delay affecting at least one-third of the posterior map. The majority of LBBB patients (n = 32, 52%) had a complete (i.e., uniform) substantial posterior delay paired with a left-sided anterior delay affecting less than one-third of the anterior map. The remaining LBBB patients had substantial posterior-only delays, which were either regional (n = 13, 21%) or complete (n = 14, 23%) delays. Conversely, all classifiable RBBB patients (n = 5, 71%) had large areas of substantial delay on the right anterior map, and no RBBB patients exhibited LBBB-associated activation sequences.

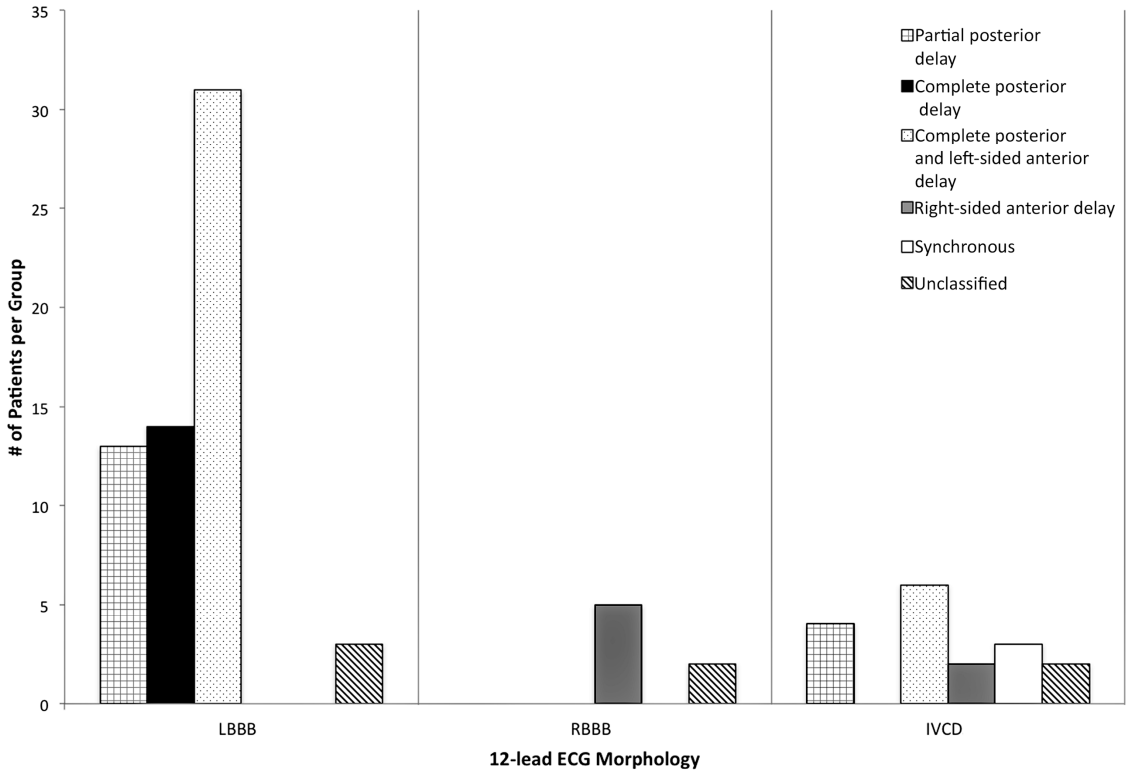

Figure 4-4. Distribution of activation sequences for each 12-lead ECG morphology
Most LBBB patients (95%) displayed posterior delay. Most RBBB patients (71%) displayed right-sided anterior delay. The IVCD patients displayed all of the map sequences except the LBBB-associated complete posterior delay.

4.4.2.2 IVCD patients

IVCD patients displayed activation sequences associated with five different groups. Most IVCD patients displayed LBBB-associated sequences (n = 10, 59%), while the rest displayed an RBBB-associated (n = 2, 12%) sequence, an IVCD-only, relatively synchronous, sequence with no substantial delays (n = 3, 18%) or were unclassified (n = 2, 12%). Figure 4-5 shows 12-lead ECGs and the mapped body surface activation sequences for a pair of IVCD patients that had sequences associated with different groups. Figure 4-5A shows the data for an IVCD patient with an LBBB-associated activation sequence (patient A), and panel B shows the data for an IVCD patient with an unclassifiable

activation sequence (patient B). Both patients had a 12-lead ECG QRSd of 142 ms and neither LBBB nor RBBB 12-lead ECG morphology. The LBBB-associated activation sequence of patient A shows a large area of substantial delay on the posterior map, no concomitant anterior delay, and had high values for both BSAd and SDAT (132 ms and 57.6 ms, respectively). In contrast, the unclassifiable activation sequence of patient B shows a moderate left-sided posterior delay with a milder left-sided anterior delay. The BSAd and SDAT values of the unclassifiable patient presented in panel B (74 and 28.3 ms, respectively) were nearly half those of the LBBB-like patient presented in panel A.

As shown in Figure 4-6, the IVCD patients with LBBB-associated activation sequences were not significantly different from IVCD patients with other sequences (RBBB-associated, synchronous, or unclassifiable) by 12-lead ECG or MECG QRSd values (12-lead ECG: 134 ± 13 ms vs. 142 ± 15 ms, $p = 0.24$; MECG: 158 ± 16 ms vs. 155 ± 12 ms, $p = 0.68$). In contrast, LBBB-like IVCD patients tended to have more dyssynchrony by BSAd (88 ± 18 ms vs. 71 ± 20 ms, respectively, $p = 0.08$) and were significantly more dyssynchronous by SDAT (32 ± 9 ms vs. 21 ± 5 ms, respectively, $p = 0.01$).

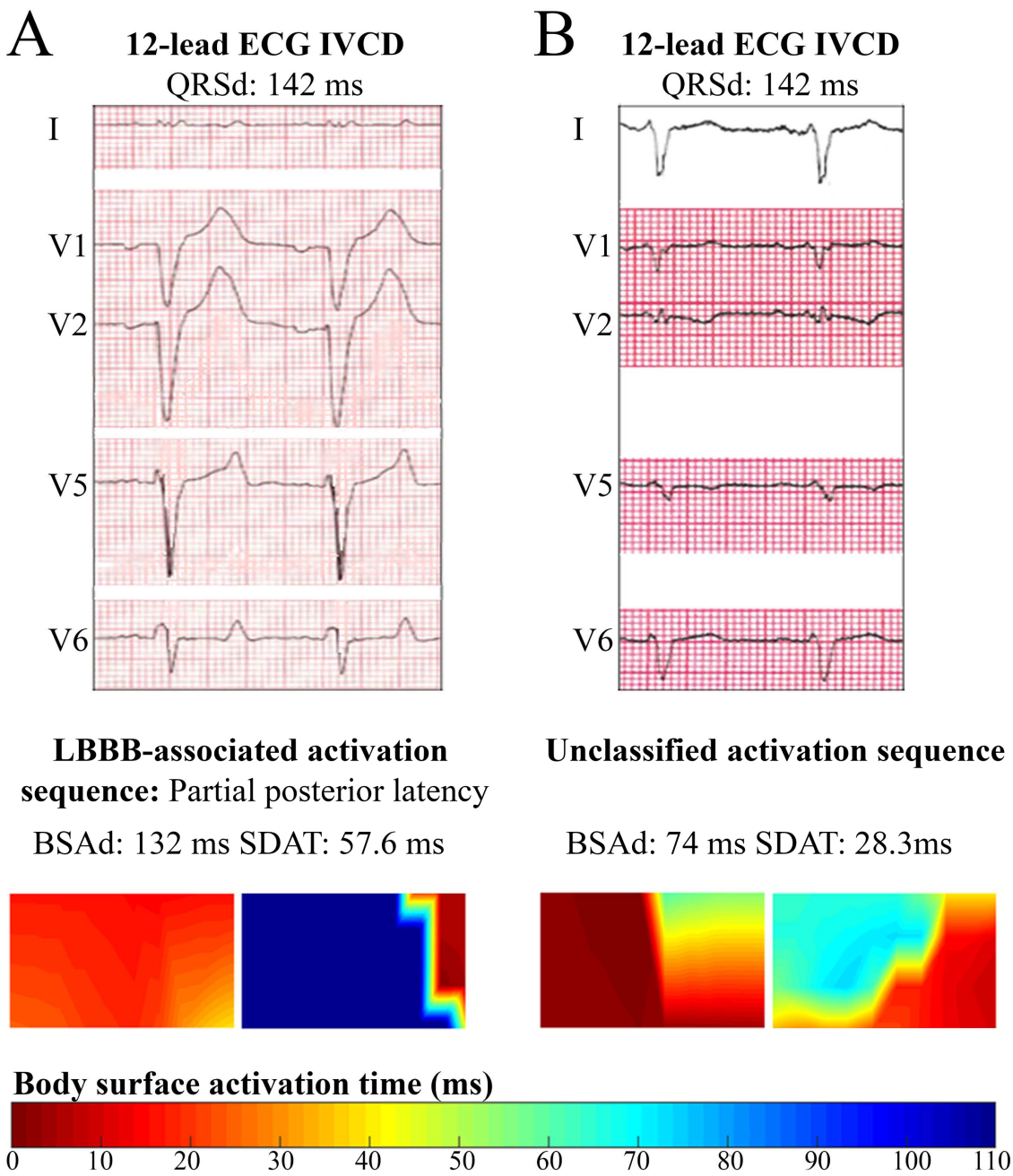

Figure 4-5. Pair of IVCD patients with different activation sequences

(A) A patient who had an IVCD 12-lead ECG morphology and exhibited an LBBB-associated activation sequence with a partial significant delay. (B) A patient who had an IVCD 12-lead ECG morphology and QRSd of 142 ms exhibited an unclassifiable sequence with partial posterior and a milder anterior delay.

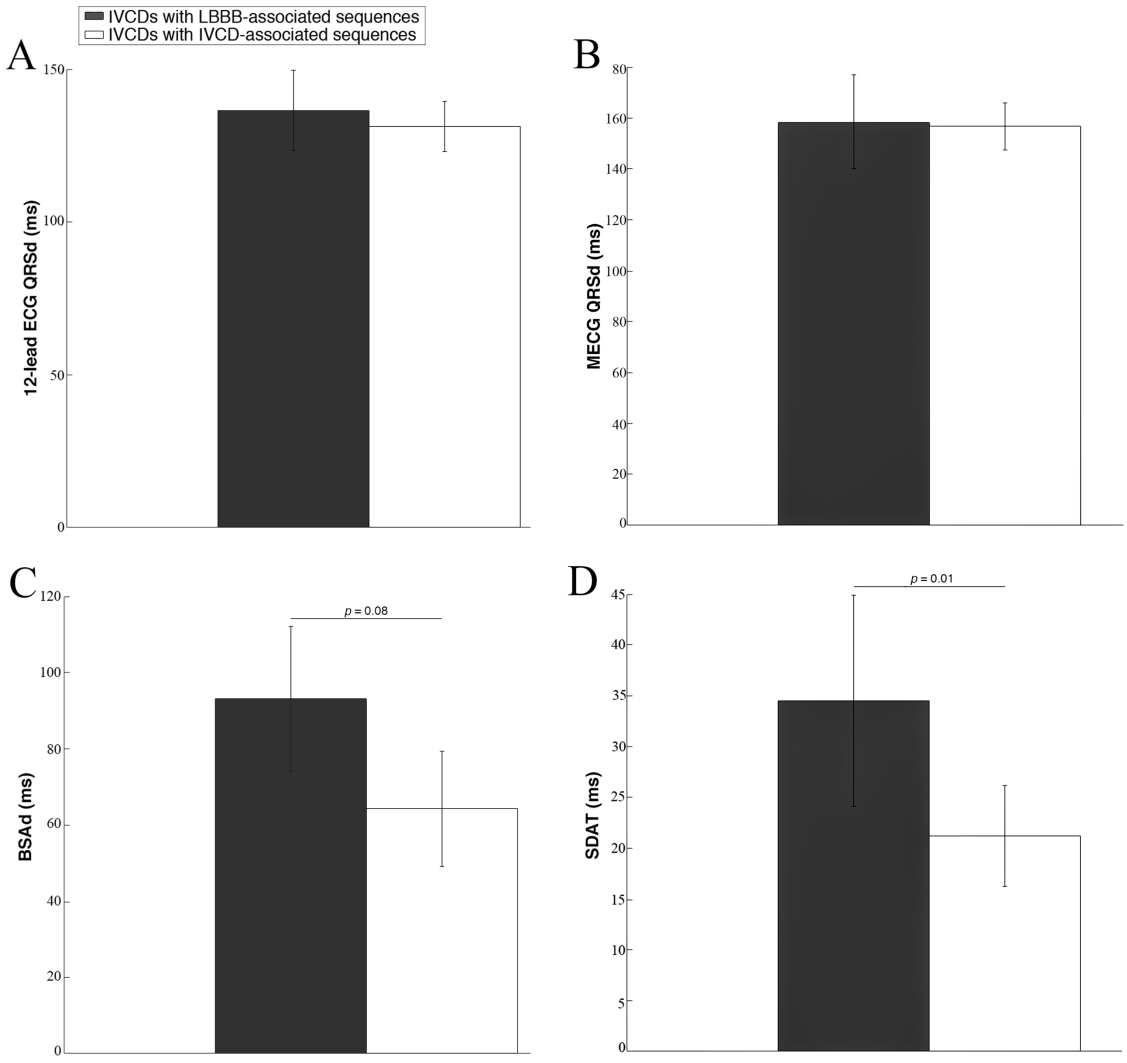

Figure 4-6. Comparison of IVCD patients with and without LBBB-associated activation sequences
IVCD patients with LBBB-associated activation sequences had higher BSAd and significantly higher SDAT values than IVCD patients with other activation sequences.

4.5 Discussion

In this study, mapped body surface activation sequences were compared within and between 12-lead ECG morphological subgroups. The mapped body surface activation sequences of LBBB and RBBB patients were distinct. In addition, a group of IVCD

patients with LBBB-like activation sequences was identified, and these LBBB-like IVCD patients had more dyssynchrony than the other IVCD patients based on body surface activation metrics.

4.5.1 Body surface activation sequences of LBBB and RBBB patients

Broadly, the observed body surface activation sequences matched the expected order of cardiac activation events based on LBBB and RBBB physiology. All LBBB patients with classifiable activation sequences (95%) exhibited delayed activation across most or all of the posterior map. This delay measured at the body surface echoes the delay in left ventricular (LV) depolarization that characterizes LBBB activation [64, 102]. The LBBB patients exhibited areas of posterior delay that varied in size, and some LBBB patients also had a left-side anterior delay. This inter-patient variation in the electrical substrate behavior in the LBBB population has been demonstrated in previous electrocardiographic imaging (ECGi) studies [103] and is linked to variations in LV geometry, fibrosis, and other factors, all of which may vary significantly in the CRT population [104, 105].

The RBBB patients' significant right-side anterior delay mirrors the pattern of activation associated with RBBB [64, 102]. The difference in the sizes of the areas of delay in the RBBB-associated group compared to those in the LBBB-associated group, as seen in Figure 4-3, may be due to the smaller delay-source volume in RBBB patients than in LBBB patients (i.e., the difference in the size of the right ventricle [RV] compared to that of the LV). The characteristics of and differences between the mapped body surface

activation sequences of the LBBB and RBBB patients in this study support the physiologic relevance of this data.

4.5.2 Body surface activation sequences of IVCD patients

The IVCD patients in this study with classifiable activation sequences were associated with five different groups. Moreover, a large proportion (59%) of the IVCD patients had LBBB-associated activation sequences and also had more dyssynchrony than the other IVCD patients based on BSAd and SDAT values. The percentage of identified LBBB-like IVCD patients in this study is reasonable based on the results of Hara et al., who found that 60% of IVCD patients had significant radial dyssynchrony (i.e., were LBBB-like) based on echocardiography speckle-tracking strain [51]. In contrast, in a study by Eschalier et al. of 15 IVCD patients analyzed with ECGi, only 20% had the same level of interventricular electrical dyssynchrony measured in the LBBB patient cohort (n = 18) [42].

Most of the LBBB-like patients retrospectively identified in the echocardiograph study by Hara et al. and all of the LBBB-like patients identified in the ECGi study responded to CRT [42, 51]. LV reverse remodeling outcomes were not reported in the current study because most of the IVCD patients did not have follow-up echocardiogram data available. However, native conduction SDAT values have been found to be significantly higher in CRT responders than in non-responders [61], which suggests that the higher BSAd and SDAT values seen in the LBBB-like IVCD patients indicates that they are more likely respond to CRT than the other IVCD patients.

Notably, there was no difference in 12-lead ECG QRSd values between the LBBB-like IVCD patients and the other IVCD patients in our study. The other technologies that have been used to characterize the LBBB-like IVCD population, ECGi and echocardiographic dyssynchrony analyses, are not suitable alternatives to the 12-lead ECG. ECGi is not standard clinical care for CRT candidates or patients and requires computed tomography images to map epicardial activation sequences. In contrast, echocardiograms are the standard-of-care assessment method to evaluate systolic function in CRT candidates and patients. However, criteria to identify echocardiographic LBBB-like mechanical dyssynchrony are lacking. A previous multicenter study was designed using echocardiographic dyssynchrony CRT implant criteria [50]. This study concluded that echocardiographic dyssynchrony was not a determinant of CRT response in patients that were similar by 12-lead ECG; the conclusion was reached, moreover, after the study was prematurely ended because the proportion of CRT recipients that died was nearly twice that of the control group [50].

Body surface activation mapping may be performed in real time and in a clinical setting, without the need for costly imaging, and the results of this pilot study suggest that mapped body surface activation sequences may be used in the future to identify LBBB-like IVCD patients. Further studies with a larger patient population, which would enable use of a more rigorous grouping technique, such as a machine learning approach, are needed to create and evaluate a broadly applicable LBBB-like IVCD body surface activation sequence.

4.5.3 Limitations

This was a pilot study of 85 patients with new CRT implants at a single center and without CRT outcomes. This work needs to be expanded upon in a larger study of IVCD patients for whom the relationship between LBBB-like activation sequences and patient response to CRT is available.

4.6 Conclusions

The results of this work suggest that mapped body surface activation sequences may be used to identify LBBB-like IVCD patients, who have more dyssynchrony than other IVCD patient and are, therefore, more likely to respond to CRT. Further studies are warranted to define and evaluate an LBBB-like body surface activation sequence based on a larger patient population.

5 Body Surface Activation Metrics for Prediction of Cardiac Resynchronization Therapy Outcomes

This chapter is intended for submission for publication in a peer-reviewed journal after the associated patent filings have become public. At that time, the authors will be as follows: Antonia E. Curtin, Kevin V. Burns, Jeffrey Gillberg, Subham Ghosh, Theoden I. Netoff, and Alan J. Bank.

5.1 Overview

5.1.1 Introduction

The 12-lead electrocardiogram (ECG) is the current tool for evaluating electrical dyssynchrony in cardiac resynchronization therapy (CRT) candidates and patients. However, 12-lead ECG data acquired during native conduction (i.e., pre-CRT) in CRT candidates or acquired at different CRT settings for setting selection has a limited capacity to predict patient outcomes. The goal of this work was to investigate the value of new body surface activation metrics for predicting patient outcomes in the CRT candidate evaluation (CRT_{CE}) and setting selection (CRT_{SS}) scenarios.

5.1.2 Methods

We used a novel set of body surface activation metrics derived with an investigational body surface mapping system to quantify activation times, anterior-posterior dyssynchrony, potential magnitudes, and ECG morphologies in 71 CRT patients. The physiologic relevance of the new metrics was evaluated in established CRT subgroups, and the metrics' sensitivity to changes in conduction with CRT was evaluated. A partial least squares regression (PLSR) approach was used create CRT_{CE} and CRT_{SS} models of patient

reverse remodeling outcomes. The accuracy (i.e., correlation with outcomes and classification of patients as predicted responders or non-responders) of CRT_{CE} and CRT_{SS} models created with the new metrics was compared to the accuracy of models using standard clinical variables and models using previously developed body surface activation metrics.

5.1.3 Results

The majority of the novel body surface activation metrics could distinguish CRT responders and non-responders based on differences in and changes to electrical substrate behavior. The CRT_{CE} model using the novel metrics was well correlated with patient left ventricular reverse remodeling outcomes (CRT_{CE}: $r^2 = 0.32$, $r^2_{adjusted} = 0.26$, $p < 0.01$) and reduced patient response type misclassification error by >60% compared to the models using other metrics. The CRT_{SS} model using the new metrics ($r^2 = 0.43$, $r^2_{adjusted} = 0.32$ $p < 0.01$) was nearly twice as well correlated with outcomes as the other models.

5.1.4 Conclusion

The newly developed body surface activation metrics described here for the first time are significantly better correlated with CRT outcomes in both CRT_{CE} and CRT_{SS} scenarios than standard clinical variables or previously developed body surface activation metrics. This improvement (1) enables accurately predicted response-type classification of an additional 8,500 CRT candidates yearly and (2) facilitates more informed CRT setting selection in the 30% of chronic CRT patients who are not benefiting from the therapy.

5.2 Introduction

The 12-lead electrocardiogram (ECG) is the current clinical tool for measuring cardiac electrical dyssynchrony in candidates for and patients with cardiac resynchronization therapy (CRT) devices. The CRT population, however, has a 30% rate of non-response to therapy [24], which is driven in part by the limitations of the 12-lead ECG measures used for CRT candidate evaluation or for CRT setting selection [34, 35]. CRT candidates with a wide 12-lead ECG QRS complex duration (QRSd) and an left bundle branch block (LBBB) 12-lead ECG morphology during native conduction are expected to respond to CRT [8], but QRSd criteria for CRT implant have varied across previous seminal multicenter studies and differ between the European and American guidelines [30, 31, 34, 35]. At the same time, the definition of LBBB morphology in CRT implant criteria continues to evolve [8, 33, 34], and the impact of more stringent LBBB criteria on patient outcomes has not been consistent [38-40]. CRT setting selection driven by QRSd reduction is supported by some investigators, but the relationship between changes in QRSd and patient left ventricular (LV) reverse remodeling remains uncertain [32, 46, 47]. Moreover, use of 12-lead ECG morphologic criteria for CRT setting selection is complex and, as a result, is seldom done [8, 32, 33, 48, 49].

Recently, a number of alternative or adjunctive measures of dyssynchrony, such as vectorcardiography (VCG)-based QRS_{AREA}, Q-LV, and metrics acquired through electrocardiographic imaging (ECGi), have been investigated as solutions to the shortcomings of the 12-lead ECG for CRT candidate evaluation and setting selection [35, 53, 55, 106]. These techniques in their present forms, however, either suffer from

limitations similar to those of the 12-lead ECG or are not well suited to clinical CRT_{CE} and CRT_{SS} because of complexity, invasiveness, and/or time and resources required.

In contrast, two previously developed, noninvasively acquired measures of body surface activation (hereafter, legacy metrics) derived with a custom ECG Belt investigational body surface mapping system (see *Methods*) have been shown to correlate with hemodynamic changes at different LV lead locations during CRT implant [62] and to correlate with LV reverse remodeling after CRT [61]. An advantage of these legacy metrics (the standard deviation of body surface activation times [SDAT] and the average left-thorax activation time [LTAT]) is that they may be measured in real time and at a range of CRT settings using noninvasively acquired multichannel electrocardiograms (MECGs).

The two legacy metrics, however, are defined with respect to time point of local body surface activation in each ECG. In the current study, we describe seven new body surface activation metrics, each of which is designed to reflect other ECG features that have been shown to be relevant to electrophysiologic substrate behavior in the CRT population, specifically, total activation time, anterior-posterior dyssynchrony, potential magnitudes, and ECG morphologies [32, 48, 53, 55, 81, 107]. We evaluated the new body surface activation metrics in three ways: (1) the physiologic relevance of the metrics, (2) the sensitivity of the metrics to differences in electrical substrate behavior, and (3) the utility of the metrics to predict patient CRT outcomes. The evaluation of the new body surface activation metrics for prediction of patient outcomes was applied to two clinically relevant scenarios. The first scenario of interest was prediction of outcomes for the evaluation of CRT candidates using a model based on only native conduction (i.e., pre-CRT) metric

values. The second scenario was prediction of outcomes for device setting selection in chronic CRT patients using a model incorporating both native conduction and CRT metric values.

5.3 Methods

5.3.1 Study population

The 12-lead ECGs, MECGs, and echocardiograms used in this study were acquired approximately as part of a previous study of new CRT patients at United Heart and Vascular Clinic in St. Paul, MN[8]. For that study, written informed consent was obtained from all patients and the protocol was approved by an Institutional Review Board (IRB). 12-Lead ECGs and MECGs were acquired approximately 1 week after CRT implant. The inclusion criteria for the current analyses were that patients have an ejection fraction (EF) of <40%, QRSd of ≥120 ms, intact native conduction, and sinus rhythm.

5.3.2 Echocardiography

Echocardiograms were acquired before CRT implant and at 6 months post-CRT per our standard clinical practice. LV end-systolic volume (LVESV) and ejection fraction (EF) were measured using the biplane Simpson's method [108]. Patients were classified as

[8] Data from this previous prospective study will be used throughout this dissertation. The study in question was initiated and conducted by the research department at United Heart and Vascular Clinic; study funding and equipment were provided by Medtronic, PLC. Initial results from this study were published in Gage et al. [56]

responders based on the common criterion of a reduction in LVESV of at least 15%, which is associated with clinical response [109-111].

5.3.3 12-Lead ECG acquisition and CRT setting selection

Standard 12-lead ECGs were collected during native conduction (CRT off) and at a range of CRT settings (i.e., different pacing vectors and atrioventricular [AVD] and interventricular delays). CRT setting selection and 12-lead ECG QRSd were determined according to our standard clinical practices. Briefly, the final CRT setting was identified based on wavefront fusion criteria (R-wave in V_1/V_2 and/or a reduction in QRSd) [81]. 12-Lead ECG QRSd was measured in the ECG lead with the widest complex and paced QRS complexes were measured from the ventricular pacing spike when present [112]. Moderate QRSd values were defined as 120 ms to <150 ms, and wide QRSd values were defined as ≥150 ms. All changes in metric values from native conduction to CRT (ΔNCRT) were based on the final CRT setting.

5.3.4 MECG acquisition

MECGs were acquired during native conduction and at the final CRT setting using the custom ECG Belt investigational body surface mapping system. The ECG Belt body surface mapping system has been described previously [61, 62]. The investigational system consists of a multichannel amplifier, an electrode array, and a monitor (Heartscape, Verathon, Seattle, WA) and customized data acquisition software (Medtronic, PLC,

Minneapolis, MN). As shown in Figure 5-1, the ECG Belt electrode array is composed of 17 anterior and 36 posterior unipolar ECG electrodes.

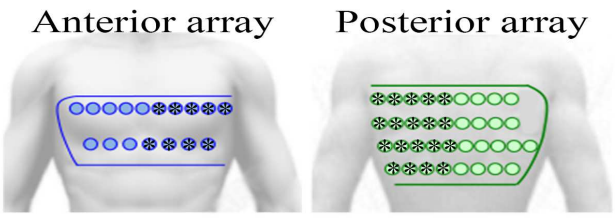

Figure 5-1. Arrangement of ECG Belt electrode array
Placement of anterior (left) and posterior (right) electrode arrays. Electrodes used in LTAT calculation are indicated with asterisks.

5.3.5 Body surface activation metrics

The methods for preprocessing and QRS complex detection in MECGs have been implemented in comprehensive stand-alone software[9] written in MATLAB (using MATLAB Release 2017b, The MathWorks, Inc., Natick, MA), which is described in detail elsewhere [96] (see Chapter 2). The software supports the loading and serial analysis of data collected during multiple conditions from one or more patients, displays the results with a graphical user interface, and performs all of the requisite calculations to determine the metrics defined subsequently.

A local body surface activation event is defined as the point of steepest negative slope during the QRS complex in each ECG, based on an extension of contact mapping principles [71]. This definition of local body surface activation has been shown to accurately represent depolarization activity in the underlying myocardium [69]. Local body surface activation times are calculated with reference to the earliest recorded local activation event

[9] The University of Minnesota, Minneapolis, MN, and United Heart and Vascular Clinic, St. Paul, MN

(time zero). These activation times are then interpolated and displayed in a pair of anterior (left) and posterior (right) isochronal activation maps.

The two legacy body surface activation metrics, for which the correlations with acute and chronic patient response have been reported previously [61, 62], are the standard deviation of the activation times (SDAT) and the left-thorax activation time (LTAT, the average activation time of the left-thorax electrodes, which are indicated with asterisks in Fig. 1).

Figure 5-2 shows sample MECGs collected during native conduction and CRT in an LBBB patient with a native 12-lead ECG QRSd of 140 ms. The corresponding isochronal activation maps are shown in Figure 5-3. Annotations on the ECGs illustrate the calculation of each of the legacy and new body surface activation metrics for both conditions in subpanels 1 to 4. For each body surface metric, larger metric values are associated with a more dyssynchronous activation sequence. The new body surface activation metrics are the MECG QRSd, anterior-posterior uncoupling (APU), anterior and posterior peak height, the body surface activation area under the curve (AUC_B), and the inter-activation event distance (IAED). Each of these metrics is defined in Table 5-1. None of the new body surface activation metrics have been investigated previously for prediction of patient outcomes, but they are described in [101].

Reproducibility of each body surface activation metric was assessed in 33 paired recordings. For each patient, the paired recordings were collected 5 to 20 minutes apart in a single visit.

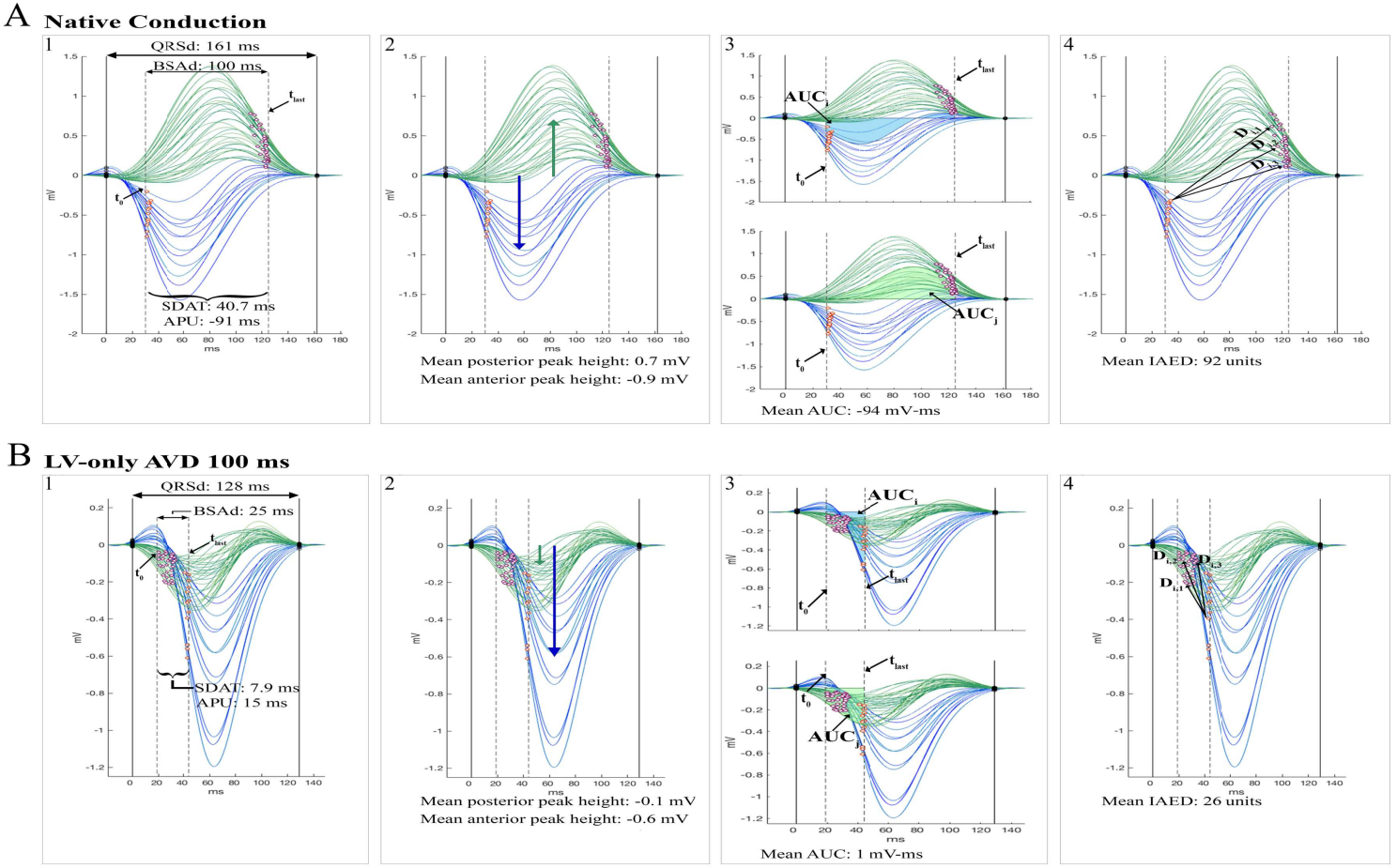

Figure 5-2. Diagram of body surface metric measurement methods

Anterior array (blue) and posterior (green) MECGs for an LBBB patient during native conduction (A) and during CRT at AdaptivCRT (aCRT) settings during a point in time when LV-only pacing with an AVD of 100 ms was being delivered by the CRT device (B). The ECGs for each condition are reproduced in panels 1 to 4 for ease of visualization. The local activation event for each ECG is marked with an orange or purple marker for anterior or posterior ECGs, respectively (B1 and C1). The mean peak heights of the anterior and posterior electrode arrays are illustrated with blue and green arrows, respectively (B2 and C2). The body surface activation area under the curve (AUC_B) is the average paired difference between the area under the curve (AUC; in mV×ms) for each anterior and every posterior ECG during the BSAd interval. The areas under the curve for an example anterior (AUC_i) and posterior (AUC_j) ECG are shown with blue and green shading, respectively (B3 and C3). The mean inter-activation event distance (IAED) is the mean of all of the Euclidean distances (x = time [ms]; y = potential [mV]) between each anterior activation event (orange markers on blue ECGs) and every posterior activation event (purple markers on green ECGs). The arrows illustrate an example subset of distances ($D_{i,1}$, $D_{i,2}$, and $Di_{,3}$) from anterior activation event "i" to three posterior activation events (B4 and C4).

Table 5-1. Definitions of body surface activation metrics

Metric (Acronym)	Auxiliary description	ΔNCRT definition
MECG QRSd	Earliest onset to latest offset across all electrodes	The difference between the metric value at native conduction and the value during CRT
Standard deviation of body surface activation times (SDAT)	N/A	
Left thorax activation time (LTAT)	Average activation time of the left-thorax electrodes [A]	
Body surface activation duration (BSAd)	Time interval across all which all activation events occur	
Anterior-posterior uncoupling (APU)	Difference between the average anterior and average posterior activation times [B]	The difference between the absolute values of the native conduction and CRT metric values [C]
Anterior peak height	Average peak height (i.e., potential magnitude) across the anterior array. Peak height for each ECG was calculated as the difference between the absolute values of the maximum and the minimum potentials over the course of the QRS complex.	The difference between the metric value at native conduction and the value during CRT
Posterior peak height	Average peak height (i.e., potential magnitude) across the posterior array. Peak height for each ECG was calculated as the difference between the absolute values of the maximum and the minimum potentials over the course of the QRS complex.	
Body surface area under the curve (AUC_B)	The average paired difference between the area under the curve (in mV× ms) for each anterior and every posterior ECG during the BSAd interval (i.e., the average of a 17-by-36 difference matrix)	The difference between the absolute values of the native conduction and CRT metric values [C]
Inter-activation event distance (IAED)	The average Euclidean distance (x: time [ms], y: potential [mV]) between each anterior activation event and every posterior activation event (i.e., the average (in arbitrary units) of a 17-by-36 distance matrix)	

[A] Indicated with asterisks in Figure 5-1

[B] APU is a body surface approximation of the ventricular electrical uncoupling metrics described by Ploux et al. and Rickard et al. [35, 64].

[C] This calculation was chosen based on the assumption that the magnitude of the difference between anterior and posterior activation events is more important than the sign of that difference.

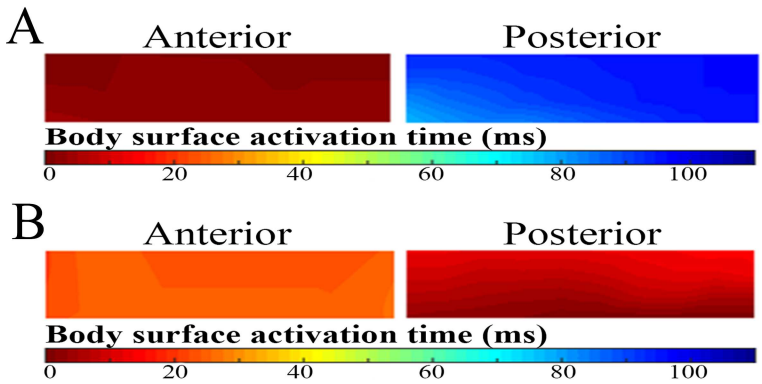

Figure 5-3. Body surface activation maps
The resulting isochronal body surface activation maps from the MECGs shown in Figure 5-2 for an LBBB patient during native conduction (A) and during CRT (B). Maps have anatomical left-to-right and right-to-left horizontal orientations for the anterior (left) and posterior (right) maps respectively.

5.3.6 Comparison of activation metrics

5.3.6.1 Identifying physiological differences between paired CRT subpopulations

To evaluate the physiologic relevance of the body surface activation metrics, 12-lead ECG QRSd values and values of all body surface activation metrics were compared for three standard paired high-dyssynchrony and low-dyssynchrony CRT patient subpopulations. The subpopulations were based on 12-lead ECG morphology (LBBB versus non-LBBB patients), QRS width (wide versus moderate), and heart failure (HF) etiology (non-ischemic [NICM] versus ischemic [ICM]).

5.3.6.2 Sensitivity of activation metrics to substrate behavior and response

To evaluate the sensitivity of the body surface activation metrics to differences in electrical substrate behavior and associated LV reverse remodeling (i.e., LVESV) outcomes, a dichotomy analysis was performed. For each metric, patients were divided into two groups (dichotomized): patients whose metric values were less than the mean and

patients with metric values that were greater than or equal to the mean. The LVESV outcomes were then compared between the two groups of patients. This analysis was performed for native conduction and ΔNCRT metric values, as well as for paired CRT patient subgroups that are expected to respond differently: males versus females, LBBB versus non-LBBB patients, wide versus moderate QRSd patients, and NICM versus ICM patients.

5.3.7 Regression models to predict patient outcomes

The goal of the regression modeling analyses was to determine if the new body surface activation metrics could be used to predict patient CRT outcomes more accurately than standard clinical variables and/or legacy body surface activation metrics. To this end, a partial least squares regression (PLSR) approach was used to create models of patient CRT LVESV outcomes for two clinically relevant scenarios: CRT candidate evaluation (CRT_{CE}) and CRT setting selection (CRT_{SS}) in chronic CRT patients. The CRT_{CE} model used clinical variables and native conduction metric values, and the CRT_{SS} model used clinical variables and both native conduction and ΔNCRT metric values.

For each scenario, the predictive values (i.e., adjusted r^2 values) of models created using three sets of variables were compared (see Table 5-2). The "clinical" variable set included the patient characteristics noted in the current CRT guidelines and those that have been widely shown to correlate with patient response [31, 113]. The legacy body surface activation variable set included all of the clinical variables as well as SDAT and LTAT (i.e., the legacy body surface activation metrics). The enhanced body surface activation

variable set included the clinical variables, the legacy body surface activation metrics, and the seven novel body surface activation metrics described above and in Figure 5-2.

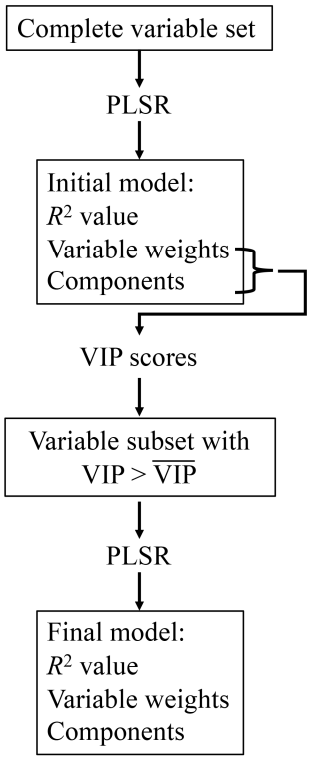

Figure 5-4. PLSR flowchart
Iterative PLSR was first applied to a complete variable set, and then the resultant variable weights and component coefficients were used to calculate the variable importance in PLSR (VIP) scores for each variable [1-5]. The final model was then determined using PLSR applied to the subset of significant predictor variables as determined by the VIP scores. $\overline{VIP}$ = average VIP score.

Iterative PLSR was used to create the CRT_{CE} and CRT_{SS} models of patient LVESV outcomes, as illustrated in the flowchart in Figure 5-4 using each of the three variable sets. PLSR was first applied using all of the variables in one of the three variable sets, and the resultant variable weights and component coefficients were used to calculate the variable importance in PLSR (VIP) scores for each variable [1-5]. VIP scores provide a relative measure of the significance of each variable for the accurate prediction of the outcome variable (i.e., change in LVESV) and permit the subsequent down-selection of only those variables that are significant contributors to the PLSR model, which could not be otherwise

determined using PLSR [1, 2, 5, 114, 115]. The subset of significant predictor variables as determined by the VIP scores (i.e., those variables with VIP scores greater than the average VIP score) was then used to create the final model using PLSR. For both the initial model and the final model, four-fold cross-validation was used to create training and testing sets of data in order to avoid over-fitting of the PLSR parameters. Adjusted r^2 values [116] were calculated to compare the predictive values of the final clinical, legacy, and enhanced models after adjusting for the number of included predictor variables. The response-type classification accuracy (i.e. the proportion of correctly identified responders and non-responders based on LVESV outcomes) was also compared for each of the CRT_{CE} models.

Table 5-2. Sets of variables used in models

Variable set	Variables included
Clinical	Gender HF etiology (ICM or NICM) ECG morphology (LBBB or non-LBBB) QRS width (wide or moderate) Pre-CRT EF
Legacy	All of the clinical variables + SDAT LTAT
Enhanced	All of the clinical variables + All of the legacy body surface activation metrics + MECG QRSd BSAd APU Anterior peak height Posterior peak height AUC_B IAED

5.3.8 Additional statistics

Student's unpaired *t*-test or a one-way analysis of variance (ANOVA) combined with multiple pairwise comparisons using Tukey's difference criterion was used to analyze

unpaired data. Multivariate regression techniques are described above. All statistical analyses were performed using MATLAB. A p-value <0.05 was considered significant.

Table 5-3. Clinical characteristics of study population

Characteristic [A]	Value [B]
Age (y)	69 ± 12
Males	48 (68%)
NYHA class III	46 (65%)
ICM	29 (41%)
Beta−blocker	67 (94%)
ACEI/ARB	66 (93%)
QRSd (ms)	152 ± 18
LBBB	52 (73%)
RBBB	7 (10%)
IVCD	12 (17%)
LVESV (mL)	124 ± 59
EF (%)	27 ± 7

[A] NYHA = New York Heart Association; ACEI/ARB = angiotensin-converting enzyme inhibitor/angiotensin II receptor blocker.
[B] Values are presented as mean ± STD or as number of patients (%).

5.4 Results

5.4.1 Study population

The clinical characteristics of 71 patients whose data was retrospectively analyzed in this study are presented in Table 5-3. The average pre-CRT EF was 27% ± 7%, the average 12-lead ECG QRSd was 152 ± 18 ms, and 52 (73%) of the patients had an LBBB by 12-lead ECG. Seventy-seven percent of patients had the right ventricular pacing lead

positioned in the septum, and 88% of patients had the LV pacing lead positioned laterally or posterior-laterally. At 6 months post-CRT implant, the average EF change was 8.4 ± 9.4 units, and the average LVESV change was −21% ± 33%. All of the body surface activation metrics showed good reproducibility, with no significant differences between paired values (n = 33) for any of the metrics.

5.4.2 Comparison of dyssynchrony metrics

5.4.2.1 Identifying physiological differences between paired CRT subpopulations

There were no differences between male and female patients with respect to any body surface activation metric or 12-lead ECG QRSd (results not shown). The results for the 12-lead ECG morphology, QRS width, and HF etiology subgroups are shown in Figure 5-5. 12-Lead ECG QRSd and both of the legacy and enhanced body surface activation metrics were significantly different between LBBB and non-LBBB patients and between wide (≥150 ms) and moderate (120 to 149 ms) QRSd patients during native conduction. As shown in Figure 5-5, both of the legacy and 5 (71%) of the new body surface activation metrics were also significantly different between NICM and ICM patients ($p < 0.05$), while 12-lead ECG QRSd values were not.

5.4.2.2 Sensitivity of dyssynchrony metrics to substrate behavior and outcomes

For each metric, patients were divided into two groups (dichotomized): patients whose metric values were less than the mean and patients with metric values that were greater than or equal to the mean. Dichotomization was also performed using gender, 12-lead ECG

morphology (LBBB versus non-LBBB), QRS width (moderate versus wide QRSd), and HF etiology (NICM versus ICM). The results of the dichotomy analyses are presented in Figure 5-6. The majority of the new body surface activation metrics (APU, anterior peak height, AUC_B, and IAED) showed significantly different LVESV outcomes when both the native conduction metric values and the ΔNCRT metric values were dichotomized about the mean (IAED native: $p = 0.06$; IAED ΔNCRT: $p = 0.09$). LVESV outcomes were also significantly different when both native conduction SDAT and ΔNCRT SDAT were dichotomized about the mean. LVESV outcomes were not significantly different between patients dichotomized, as in the current CRT guidelines, using wide and moderate (native) 12-lead ECG QRSd and were also not different between patients dichotomized using ΔNCRT 12-lead ECG QRSd.

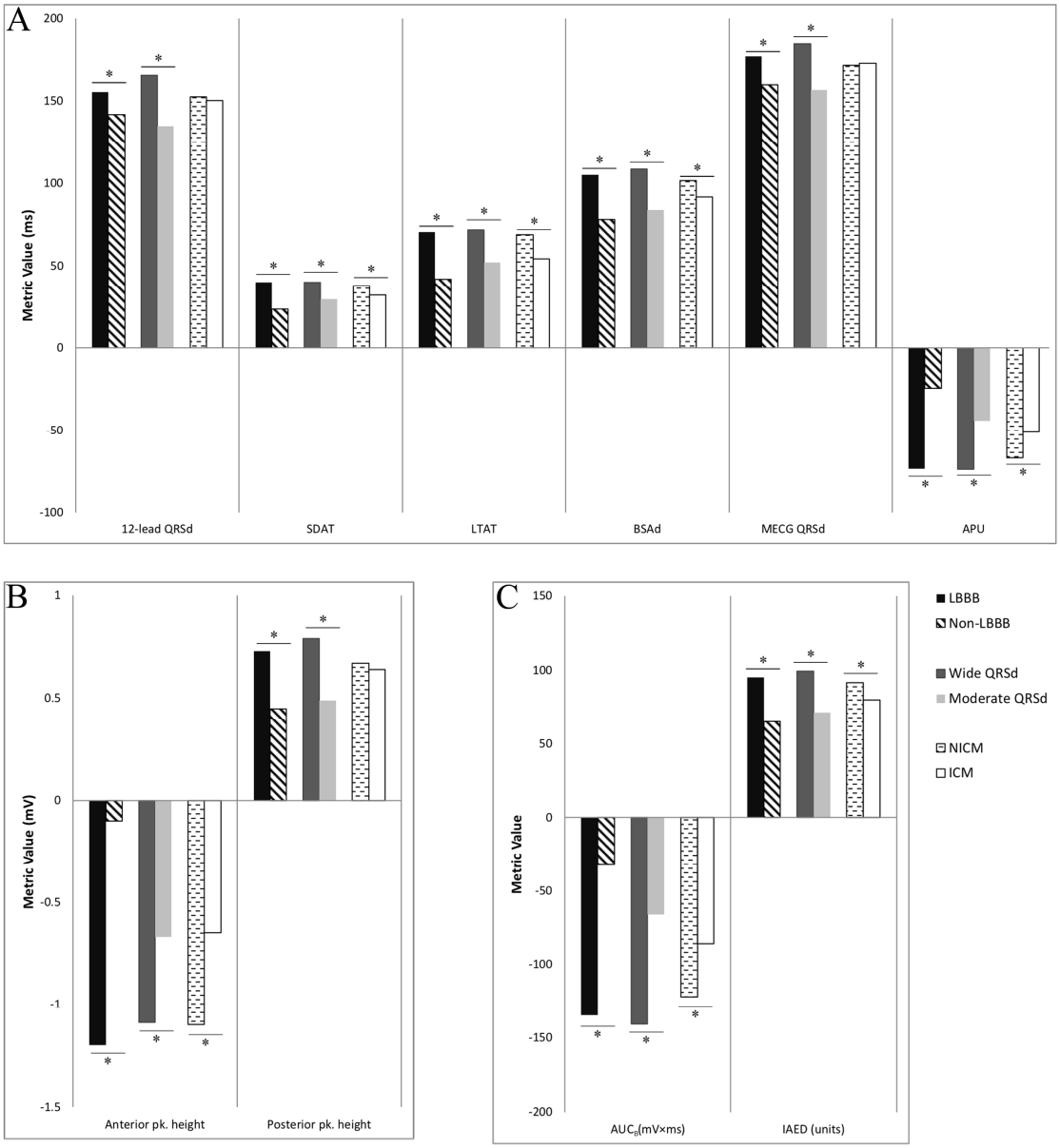

Figure 5-5. Comparison of dyssynchrony metrics in CRT subpopulations
Metrics associated with similar activity or with the same units are grouped into panels: times (ms units) (A), potential magnitudes (mV units) (B), and relationships between anterior and posterior ECG morphologies (C). Significant differences between subgroup pairs are indicated with an asterisk. 12-Lead ECG QRSd values and all of the body surface activation metrics were significantly different between LBBB and non-LBBB patients and between wide and moderate QRSd patients during native conduction. Pk. = peak.

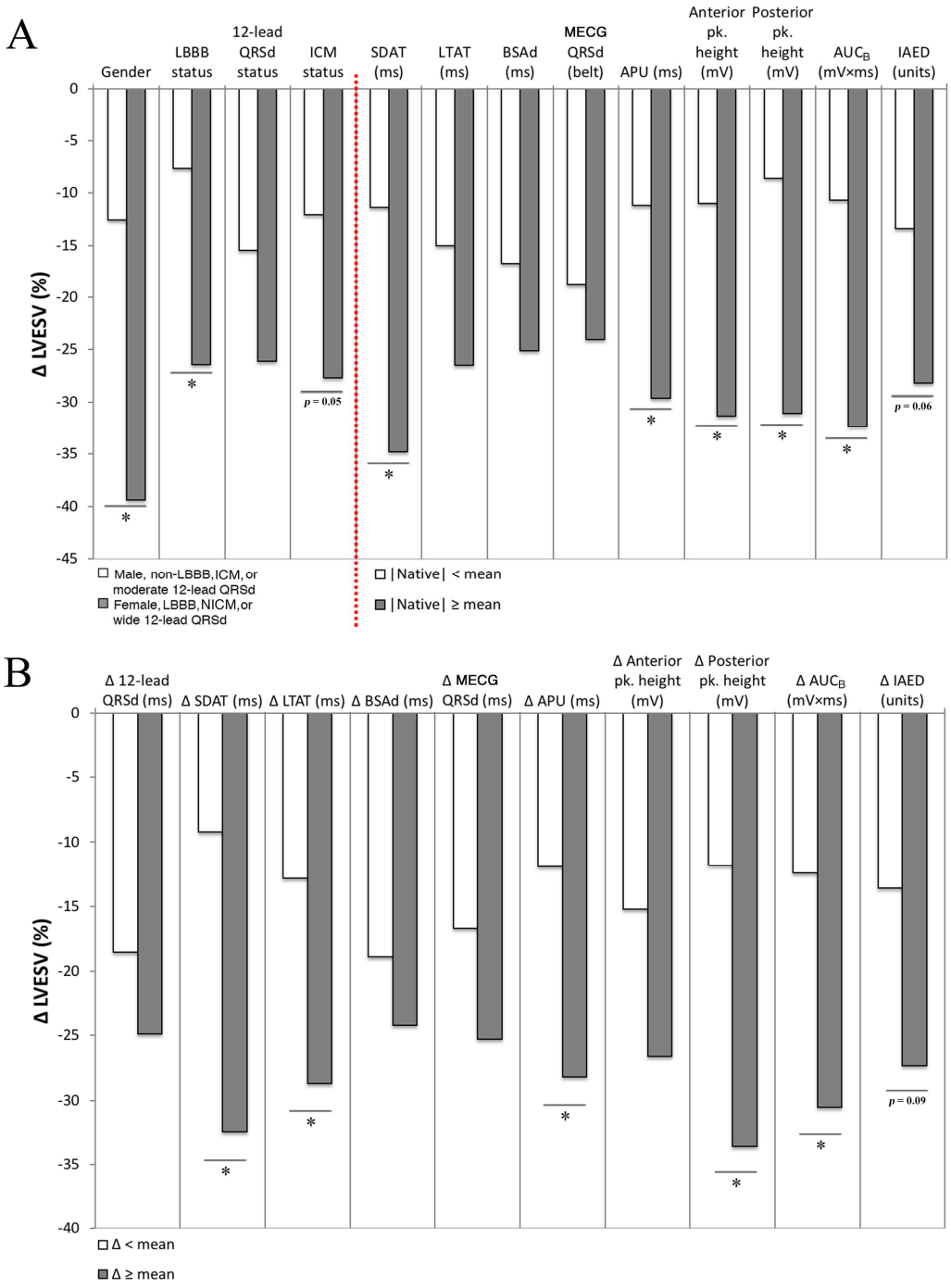

Figure 5-6. Sensitivity of dyssynchrony metrics to substrate behavior and response
(A) Red dashed line separates baseline variables (gender, LBBB status, and wide versus moderate 12-lead ECG QRSd status) from native dyssynchrony metrics. (B) ΔNCRT metric values. Significant differences between values for subgroup pairs ($p < 0.05$) are indicated with an asterisk. Most of the body surface activation metrics had significantly different LVESV outcomes when both the native conduction metric values and the ΔNCRT metric values were dichotomized about the mean. Neither native conduction nor ΔNCRT 12-lead ECG QRSd values could be used to discriminate LVESV outcomes.

5.4.3 Regression models to predict patient outcomes metrics

The performance of the CRT_{CE} models (using only clinical variables and native conduction metric values) and the variables included in each final model are presented in Tables 5-4 and 5-5, respectively. The adjusted r^2 values are reported in order to adjust the strength of each correlation for the number of variables included in the model. The magnitudes of the VIP scores (see Table 5-4) indicate the relative importance of each variable included in the model.

The clinical CRT_{CE} model was modestly correlated with LVESV outcomes ($r^2 = 0.17$, adjusted $r^2 = 0.14$, $p < 0.01$), as was the legacy CRT_{CE} model ($r^2 = 0.18$, adjusted $r^2 = 0.14$, $p < 0.01$). The enhanced CRT_{CE} had an adjusted r^2 value twice that of the clinical and the legacy CRT_{CE} models ($r^2 = 0.32$, adjusted $r^2 = 0.26$, $p < 0.01$). Notably, (1) gender was the most significant predictor in each of the CRT_{CE} models, and (2) none of the legacy body surface activation metrics were sufficiently significant predictors (i.e., had high enough VIP scores) to be included in the final enhanced CRT_{CE} model.

Figure 5-7 shows the response-type (i.e., responder or non-responder) classification accuracy for each of the CRT_{CE} models, with the classification threshold (LVESV reduction of at least 15%) indicated. The clinical and legacy CRT_{CE} models were only 56% and 58% accurate, respectively. The enhanced CRT_{CE} model, however, had an accuracy of 73%, which was a 61% to 64% reduction in misclassification of predicted patient response type compared to results with the clinical and legacy CRT_{CE} models.

Table 5-4. Performance of final CRTCE models

Model	Number of variables	r^2	r^2_{Adjusted}	p
Clinical	2	0.17	0.14	$\mathbf{4\times10^{-4}}$
Legacy	3	0.18	0.14	$\mathbf{3\times10^{-4}}$
Enhanced	6	0.32	0.26	$\mathbf{2\times10^{-7}}$

Table 5-5. Variables included in final CRT_{CE} models

Model	Included variables	VIP
Clinical	Gender	1.39
	Pre-CRT EF	1.17
Legacy	Gender	1.63
	Pre-CRT EF	0.98
	Native LTAT	0.97
Enhanced	Gender	1.90
	Wide QRSd	1.00
	Pre-CRT EF	1.02
	Native BSAd	1.01
	Native posterior peak height	1.26
	Native AUC	1.01

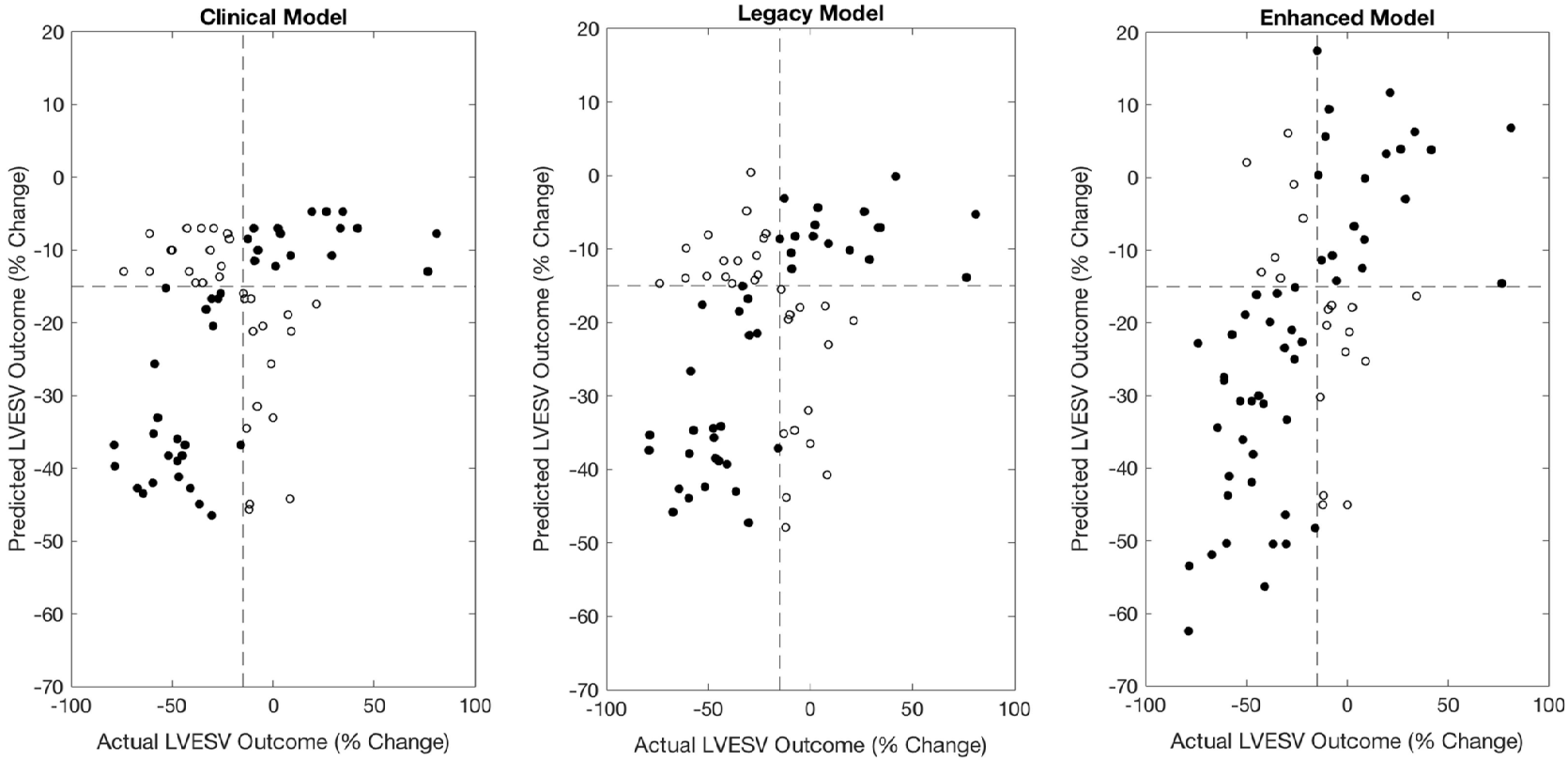

Figure 5-7. Accuracy of LVESV outcomes predicted by the CRT_{CE} models
Patients accurately identified by the model as responders or non-responders are indicated by filled circles. The cutoff value for LVESV response (indicated by dashed lines) was ≥15% ΔLVESV. The clinical model (A) and the legacy model (B) were 56% and 58% accurate, respectively. The enhanced model (C) was 73% accurate.

The performance of the CRT_{SS} models (using clinical variables and both native conduction and ΔNCRT metric values) and the variables included in each final model are presented in Tables 5-6 and 5-7, respectively. The results for each model are shown in Figure 5-8. The clinical CRT_{SS} model included the ΔNCRT 12-lead QRSd data as a significant predictor in addition to the variables included in the clinical CRT_{CE} model. In spite of this addition, the clinical CRT_{SS} model was not an improvement on the clinical CRT_{CE} model ($r^2 = 0.18$, adjusted $r^2 = 0.15$, $p < 0.01$). Furthermore, the strength of the correlation with LVESV outcomes for the legacy CRT_{SS} model remained below that of the enhanced CRT_{CE} model. However, addition of legacy ΔNCRT metric values, specifically LTAT, in the legacy CRT_{SS} model improved the strength of the correlation (i.e., adjusted r^2 value) with LVESV outcomes by 43% compared to that of the legacy CRT_{CE} model ($r^2 = 0.26$, adjusted $r^2 = 0.20$, $p < 0.01$). The incorporation of ΔNCRT metric values in the enhanced CRT_{SS} model improved the correlation by 23% compared to that of the enhanced CRT_{CE} model (LVESV: $r^2 = 0.43$, adjusted $r^2 = 0.32$ $p < 0.01$). Similar to the performance of the CRT_{CE} models, the strength of the correlation with LVESV outcomes (i.e., adjusted r^2 value) for the enhanced CRT_{SS} model was approximately 150% greater than that of the legacy CRT_{SS} model.

Table 5-6. Performance of final CRT_{SS} models

Model	Number of variables	r^2	$r^2_{Adjusted}$	p
Clinical	3	0.18	0.15	$\mathbf{2\times10^{-4}}$
Legacy	5	0.26	0.20	$\mathbf{7\times10^{-6}}$
Enhanced	11	0.43	0.32	$\mathbf{7\times10^{-10}}$

Table 5-7. Variables included in final CRT_{SS} models

Model	Included variables [A]	VIP
Clinical	Gender	1.51
	Pre-CRT EF	1.00
	ΔNCRT 12-lead ECG QRSd	1.03
Legacy	Gender	1.80
	Wide QRSd	1.01
	Pre-CRT EF	1.04
	Native LTAT	1.03
	ΔNCRT LTAT	0.96
Enhanced	Gender	1.97
	Wide QRSd	0.97
	Pre-CRT EF	1.01
	Native BSAd	1.16
	Native MECG QRSd	0.98
	Native posterior peak height	1.27
	Native AUC	1.02
	Native IAED	1.05
	ΔNCRT MECG QRSd	1.10
	ΔNCRT anterior peak height	1.14
	ΔNCRT posterior peak height	1.15

[A] For each model (clinical, legacy, or enhanced), variables not included in the respective CRT_{CE} model are identified with bold text.

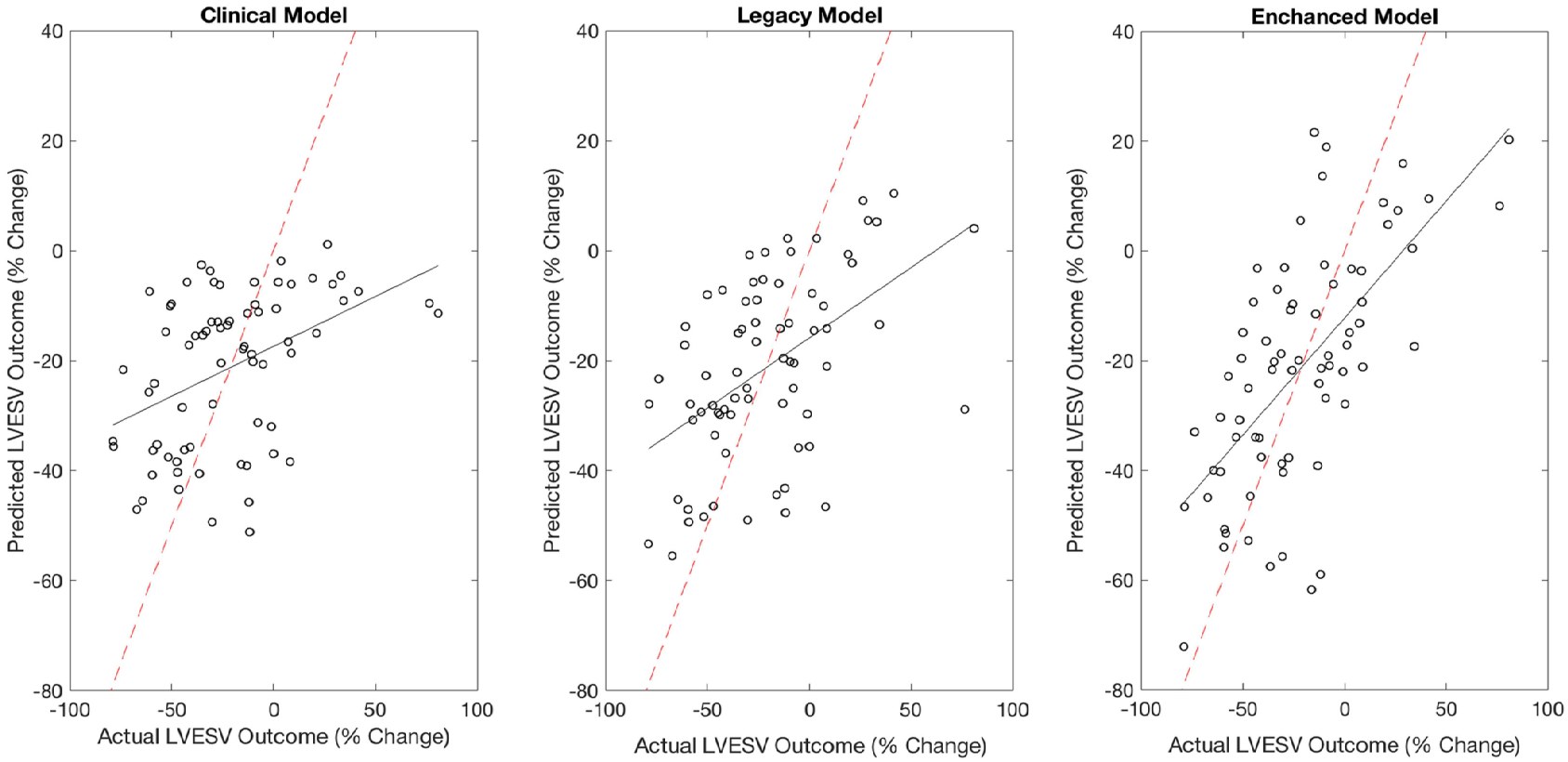

Figure 5-8. Accuracy of LVESV outcomes predicted by the CRTss models
The correlations between the predicted and actual LVESV outcomes had r^2 values of 0.18 and 0.26 for the clinical (A) and legacy (B) models, respectively. The enhanced model (C) had an r^2 value of 0.42. The p-value was less than 0.01 for all three models. Dashed red line represents the line of equality.

5.5 Discussion

In this study, we describe seven novel measures of body surface activation derived from MECGs acquired with the ECG Belt investigational body surface mapping system. We evaluated the physiological relevance of these metrics and their sensitivity to changes in electrical substrate behavior and associated LV reverse remodeling. We compared the added predictive value of these metrics to that of standard clinical variables and previously described (i.e., legacy) body surface activation metrics using models designed for two clinical scenarios: CRT candidate evaluation model used clinical variables and native conduction metric values and CRT device setting selection using clinical variables and both native conduction and ΔNCRT metric values.

The new body surface activation metrics reflected the expected physiological differences between established CRT patient subgroups during native conduction and were also sensitive to changes in electrical substrate behavior. Moreover, the CRT_{CE} model using the new body surface activation metrics (i.e., the enhanced CRT_{CE} model) reduced misclassification error for patient response type (i.e., prediction of patient response or non-response) by 61% to 64% compared to results with models using standard clinical variables or legacy body surface activation metrics. In addition, the enhanced CRT_{SS} model was nearly twice as well correlated with patient LVESV outcomes as the clinical or legacy CRT_{SS} models.

5.5.1 Comparison of body surface activation metrics

5.5.1.1 Identifying physiological differences between paired CRT subpopulations

Both of the legacy and new body surface activation metrics showed more dyssynchrony in the expected established CRT subgroups (i.e., LBBB and wide QRSd patients). In addition, most of the new and both of the legacy body surface activation metrics showed more dyssynchrony in NICM patients than in ICM patients, while the current clinical standard, 12-lead ECG QRSd, did not. The body surface activation metric values indicated increased activation dyssynchrony in the NICM patients compared to that of ICM patients. Increased dyssynchrony during native conduction is associated with better response to CRT, and these body surface activation metric results provide an explanation for studies showing that NICM patients respond better to CRT than ICM patients [117], which matches results seen in our study (see Figure 5-5). These results show that the activity being measured by the body surface activation metrics is reflective of the underlying substrate physiology.

5.5.1.2 Sensitivity of dyssynchrony metrics to substrate behavior and outcomes

The analysis of LVESV outcomes and dichotomized body surface activation metrics evaluated their sensitivity to differences (native conduction metric values) and changes (ΔNCRT metric values) in electrical substrate behavior. When dichotomized, both native conduction and ΔNCRT values for the majority of the new body surface activation metrics distinguished groups of patients that were significantly different based on LVESV outcomes. In contrast, in spite of their ubiquity in CRT candidate evaluation criteria and

prevalence in CRT optimization strategies, neither native conduction nor ΔNCRT 12-lead ECG QRSd values could significantly discriminate LVESV outcomes. The sensitivity of the novel body surface activation native conduction and ΔNCRT metrics demonstrates that they are capturing characteristics of the electrical substrate behavior that are effectors of LV reverse remodeling outcomes.

5.5.2 Regression models to predict patient outcomes

The enhanced CRT_{CE} and CRT_{SS} models clearly demonstrate the significant contributions of the new body surface activation metrics for the prediction of patient CRT outcomes. The enhanced CRT_{CE} model had a response-type classification accuracy of 73%, which represented a 61% reduction in misclassification error over the CRT_{CE} model based on the legacy body surface activation metrics and a 64% improvement over the clinical-guideline-based CRT_{CE} model. The impact of the new body surface activation metrics also translated to an enhanced CRT_{SS} model with a correlation (i.e. adjusted r^2 value) with patient LVESV outcomes that was 150% of that for the clinical or legacy CRT_{SS} models, neither of which performed as well as the enhanced CRT_{CE} model in spite of the addition of ΔNCRT data. The inclusion of ΔNCRT metric values did lead, however, to a significant improvement in the enhanced CRT_{SS} model over the enhanced CRT_{CE} model, highlighting the further optimization potential available using ΔNCRT data for setting selection in chronic CRT patients.

Most of the new body surface activation metrics and none of the legacy body surface activation metrics were incorporated into the enhanced CRT_{CE} and/or CRT_{SS} models. The

clinical variables of gender, wide 12-lead ECG status, and baseline EF were included in the enhanced models, and gender was the most significant predictor (i.e., highest VIP score) overall. The significance of gender for prediction of LVESV outcomes is likely because of the discrepancy between baseline LVESV values in men and women and the associated impact on the LVESV percent change outcome measure [118].

The new body surface activation metrics included in the final enhanced models were BSAd, MECG QRSd, anterior and posterior peak heights, AUC_B, and IAED. Of these, the native conduction and ΔNCRT posterior peak height metrics were the most significant predictors in both the CRT_{CE} and CRT_{SS} models. However, for both the CRT_{CE} and CRT_{SS} models, the other significant body surface activation metrics contributed equally to the accuracy of the model (see Tables 5-5 and 5-7). These findings suggest that the activation time, potential magnitude, and ECG morphology information that are captured by the new body surface activation metrics included in the models reflect distinct activation information that makes each metric relevant to predicting LVESV outcomes. The individual relevance of activation times, potential magnitudes, and ECG morphologies to electrical substrate behavior in CRT patients is supported by previous, independent work and will be summarized briefly below.

5.5.2.1 Activation time metrics

BSAd and QRSd are both measures of activation time. BSAd is the body surface approximation of total ventricular activation time, a reduction in which Strik et al. have shown to be correlated with improved synchrony and acute hemodynamic response [107].

The MECG QRSd differs in both acquisition and measurement from the 12-lead ECG QRSd, which may be why the MECG QRSd was a significant predictor in the final enhanced CRT_{SS} model. The unipolar ECG electrode array used with the ECG Belt investigational body surface mapping system collects more than four times as many ECGs as a conventional 12-lead ECG and uses only unipolar electrodes. The ECG Belt array also captures data from a larger, different area of the torso, with more than two-thirds of the electrodes located on the posterior. Previous studies have shown that these characteristics of MECG systems make them more sensitive than 12-lead ECGs or VCGs to electrical substrate behavior [57, 58]. Posterior body surface activation data may be of added value because of the more-posterior orientation of the LV, which is of particular relevance in the mainly LBBB CRT population [32, 53, 81]. However, the specific value of anterior-derived versus posterior-derived QRSd data has not been investigated. Last, the global method of QRS complex measurement, used in the custom MECG analysis software, has been shown to be more sensitive to differences in QRSd [91] but is not yet the clinical norm for 12-lead ECG.

5.5.2.2 Potential magnitude metrics

The importance of anterior and posterior ECG peak heights has been demonstrated with both 12-lead ECG and VCG data. QRS complex peak heights and polarities from precordial 12-lead ECGs reflect the primary direction of depolarization activity, which is anterior to posterior in LBBB patients [32, 53, 81]. As a result, more balance between anterior and posterior depolarization activity, measured by changes in QRS complex R-

and S-wave heights, is a key component of wavefront fusion-based CRT optimization strategies for 12-lead ECGs [48, 56]. Similarly, VCG data has shown that large-amplitude QRS complexes in the anterior-posterior vector during native conduction are associated with better patient response to CRT [53].

5.5.2.3 ECG morphology metrics

The component of ECG morphology measured by AUC_B (i.e., the area inscribed by the ECG QRS complex) has also been the subject of VCG studies. These studies highlight the importance of the VCG QRS_{AREA}, which has been shown to be able to discriminate between CRT responders and non-responders and to reflect the physiologic characteristics of known CRT subgroups [55]. Because of the differences in the arrangement of the electrodes used with the ECG Belt body surface mapping system and that of a VCG system, the AUC_B was calculated using the average area between each anterior and posterior curve in order to best capture the anterior-to-posterior depolarization wavefront activity.

There is no direct analog to IAED available in the literature. IAED measures the Euclidean distance between anterior and posterior activation events within the QRS complex. As shown in Figure 5-2, these diagonals bisect the ECG area and reflect timing and magnitude differences in the depolarization wavefronts associated with anterior and posterior activation events. IAED, like AUC_B, uses the differences between anterior and posterior ECGs to measure the anterior-to-posterior depolarization activity, but IAED differs in its focus on the time of local body surface activation and the associated local ECG magnitude in its calculation.

5.5.3 Limitations

CRT setting selection in this study was performed by 12-lead ECG optimization based on wavefront fusion criteria, a method which is not currently a standard of care for CRT patients at most centers. This strategy is utilized in our clinic to improve patient CRT outcomes but may result in greater changes between native conduction and CRT pacing measures than seen in the typical CRT patient population. This study was a retrospective analysis of 71 new CRT patients with intact native conduction, and the results must be confirmed in a larger patient population.

5.5.4 Clinical significance

The long-standing issue of non-response to CRT, which affects approximately 30% of recipients, is likely driven by a lack of metrics that are predictive of patient outcomes and that may be used to inform CRT candidate evaluation and CRT setting selection [24, 28, 45]. The body surface activation metrics described herein may be used to improve the current standard of care in both of these scenarios. Approximately 50,000 new CRT devices are implanted annually [22], and use of the enhanced CRT_{CE} model could lead to 8,500 additional correctly evaluated CRT candidates each year. In addition, CRT non-responders have a 5-year survival probability of 50%, while >90% of responders are likely to survive over the same time frame [25]. In these chronic CRT patients, the enhanced CRT_{SS} model may be applied to select the CRT setting most likely to yield LV reverse remodeling, with

a correlation (i.e., adjusted r^2 value) that is 150% greater than that of current clinical approaches.

One of the key features of the ECG Belt investigational body surface mapping system is that it enables the ready collection MECGs and subsequent calculation of body surface activation metrics at a range of CRT settings in a clinical environment. The addition of the new metrics described in this work does not add to the time or resources required to collect the MECGs. This strength of the ECG Belt system is in contrast to the requirements and limitations of other systems being investigated for improving outcomes in CRT patients, such as VCG- or ECGi-based techniques. VCG-based metrics are based on the transformation of 12-lead ECG data and, as a result, are likely to suffer from similar spatial and sensitivity limitations [57, 58]. ECGi is more permanently limited in its applications and is ill suited to routine use in an outpatient clinic because this technology requires the acquisition of costly, non-standard computed tomography images and, in many cases, intravenous contrast [72].

5.6 Conclusions

The new body surface activation metrics described for the first time in this study capture physiologically relevant information about the behavior of the electrophysiologic substrate that is associated with LV reverse remodeling outcomes. The combined predictive value of the new body surface activation metrics could be used to accurately predict patient response type in an additional 8,500 CRT candidates each year and facilitate more-informed CRT setting selection in the 30% of CRT recipients who are not benefiting

from the therapy. The impact of the new body surface activation metrics, combined with the ECG Belt investigational body surface mapping system's ease of use in a real-world outpatient clinic, makes these metrics a potentially powerful tool to improve patient response to CRT in the future.

5.7 Acknowledgements

This work was supported by a grant through the Medtronic External Research Program, Medtronic, PLC. Ms. Curtin, Mr. Gage, Dr. Burns, Dr. Netoff, and Dr. Bank have received grant and consulting payments from Medtronic. Dr. Ghosh and Mr. Gillberg are employees of Medtronic.

6 Left Ventricular Orientation and Position in an Advanced Heart Failure Population

This chapter is reprinted with permission from Elsevier GmbH.

Antonia E. Curtin, Kevin V. Burns, Ryan M. Gage, Alan J. Bank. "Left ventricular orientation and position in an advanced heart failure population." *Translational Research in Anatomy*, 7 (2017): p. 12-19.

6.1 Overview

6.1.1 Introduction

Previous canine and *in silico* studies indicate that left ventricular (LV) orientation and position have clinically significant effects on standard 12-lead electrocardiogram (ECG) elements, which are particularly relevant in an advanced heart failure (HF) population. Our objectives were to investigate the real-world implications of these previous results by describing for the first time the range of LV orientations and positions in HF patients, identifying clinical predictors of orientation and position, and investigating how thoracic geometry may affect orientation and position.

6.1.2 Methods

Cardiac magnetic resonance images (MRIs) were used to measure LV orientation angles, LV position, chest dimensions, and the ratio of LV volume to thoracic area (LVTR). Multivariate regression analyses were used to identify significant predictors of orientation and position.

6.1.3 Results

The mean frontal plane LV orientation angle was 31 ± 11° (range, 0° to 47°) and fell within the ranges used in previous studies of orientation effects. Orientation in the transverse plane, the effects of which have not been simulated previously, averaged 48 ± 10° (range, 21° to 71°). The ranges of LV positions in the frontal and transverse planes (7.9 and 5.6 cm, respectively) are similar to or greater than those used *in silico*. Orientation and position were weakly correlated with multiple significant predictors, and the relationship between HF progression and LV orientation and position could not be determined.

6.1.4 Conclusion

Variation in LV orientation and position in advanced HF patients is large and cannot be readily predicted using the standard clinical variables or the additional thoracic geometry measures used in this study. These findings may have significant clinical implications because of the possible effects of orientation and position on key 12-lead ECG features. New tools and additional studies are needed before LV orientation or position data can be incorporated into clinical 12-lead ECG interpretation.

6.2 Introduction

Previous canine and *in silico* studies have shown that alterations in left ventricular (LV) orientation and position significantly alter the main diagnostic elements of the 12-lead electrocardiogram (ECG), including QRS duration (QRSd) and morphology [119-125]. These studies used ranges of orientations and positions based on limited, healthy-patient

data [124, 125]. In addition, population studies documenting LV orientation or position have focused on patients without cardiovascular disease [126-129]. The single identified study that reported LV orientation ranges in a heart failure (HF) population included only 13 HF patients out of a total cohort of 77 [130]. The relationship between LV orientation, LV position, and thoracic geometry has not been reported previously. We hypothesized that LV orientation and position would correlate strongly with thoracic geometry and LV size and that such relationships could help identify patients predisposed to unusual LV orientations or positions and to subsequent confounding effects on the interpretation of their 12-lead ECGs.

The potential effects of LV orientation and position on 12-lead ECG features are particularly relevant for the HF population. 12-Lead ECG elements such as QRSd, QRS waveform components (i.e., R- and S-wave patterns and notching), and the QRS axis are relied upon for diagnosing underlying conduction abnormalities and previous myocardial infarctions [100, 131-134]. The same features are used to determine if a patient is a candidate for treatments such as cardiac resynchronization therapy (CRT) [135-137]. Although many studies have investigated the effects of body habitus, age, gender, and LV anatomy on 12-lead ECG results [104, 121, 138, 139], efforts to adjust 12-lead ECG measures and lead positioning to account for cardiac orientation or position have failed [124, 125, 129].

Our primary study goal was to investigate the real-world implications of previous simulation studies by describing for the first time LV orientations and positions in a large population of advanced systolic HF patients. We also aimed to identify any relationships

between LV orientation and position and standard clinical variables, such as age, body mass index (BMI), LV volume, QRSd, and thoracic geometry measures (e.g., chest depth and width). Such information constitutes the first step in determining the possible impact of LV orientation and position variation in a clinical setting, in identifying patients that are likely to have unusual LV orientations or positions, and in defining the need for new technologies or strategies to address this issue.

6.3 Methods

6.3.1 Study design and data collection

This was a retrospective study of advanced systolic HF patients at United Heart and Vascular Clinic (UHVC) in St. Paul, MN, who participated in a study of patients with new CRT implants between 2013 and 2015. For that study, written informed consent was obtained from all patients, and the study protocol was approved by an IRB. Inclusion criteria for the current analyses were clinical HF and a viable cardiac magnetic resonance image (MRI) less than 2 years prior to CRT implant. Patients were excluded if they had atrial fibrillation, previous right ventricular pacing, or complete heart block.

MRIs available for analysis were acquired using a Siemens MAGNETOM Avanto 1.5T system (Siemens, Erlangen, Germany) and in the course of standard clinical care. Patients were imaged in the supine position. Images from axial and coronal plane TrueFISP sequences without breath hold were used in this analysis. For each patient, a frontal plane image was selected such that the aortic valve, outflow tract, and pulmonary artery were

visible in addition to the LV. A four-chamber transverse plane image was selected such that the interventricular septum could be clearly visualized.

6.3.2 Determination of orientation, position, and thoracic geometry measures

For each patient, the two MRI images were used to measure frontal and transverse plane LV long axis orientation angles, chest depth, chest width, and anterior-posterior and medial-lateral LV position in the transverse plane.

The method for LV orientation angle determination was based on that of Foster et al., who showed that the resulting measurements were not affected by respiration or the cardiac cycle [130]. Figure 6-1 demonstrates the coordinate systems for frontal (panel A) and transverse (panel B) plane LV orientation angles, which are the same as those used by Foster et al. [130]. Frontal (Figure 6-2A) and transverse (Figure 6-2B) plane LV orientation angles were determined by drawing a line tangent to the LV apex, measuring the perpendicular to the apex tangent, and then measuring the angle between that perpendicular and the horizontal.

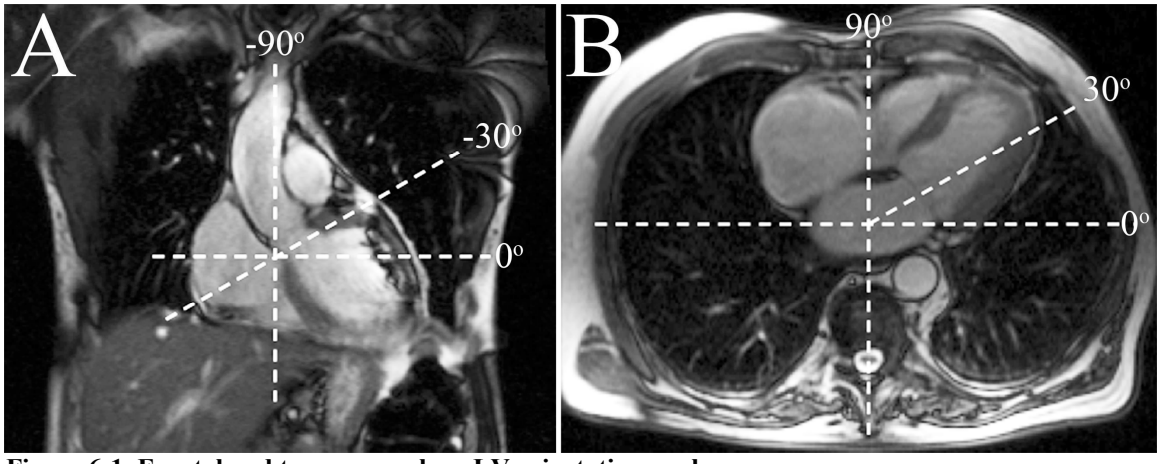

Figure 6-1. Frontal and transverse plane LV orientation angles
Coordinate systems for frontal (A) and transverse (B) plane LV orientation angles.

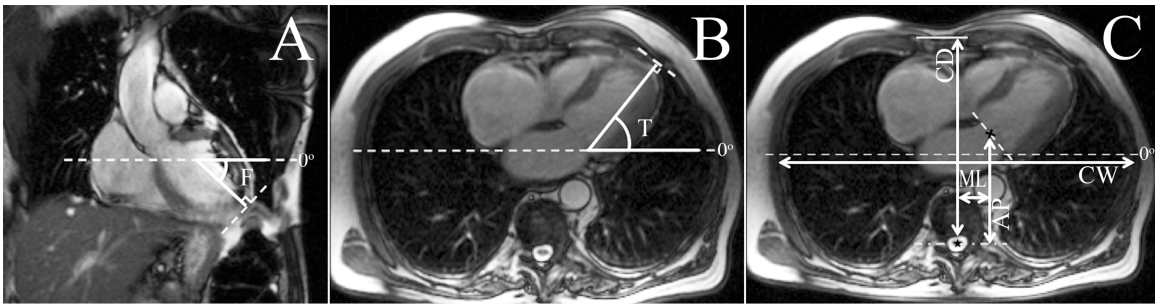

Figure 6-2. Frontal and transverse plane measurements
(A) Illustration of horizontal axis and LV apex tangent used for frontal plane (F) LV orientation angle measurement. (B) Illustration of horizontal axis and LV apex tangent used for transverse plane (T) LV orientation angle measurement. (C) Chest depth (CD) was measured using the vertical from the center of the visible spine (indicated by a black star) to the level of the sternum (white line), while chest width (CW) was measured using the maximum transverse internal thoracic diameter. Anterior-posterior LV position (AP) was measured using the vertical beginning at the mid-point of the line across the mitral valve plane (black x and white dashed line) and terminating at the horizontal through the center of the visible spine (black star and white dashed-dotted line). Medial-lateral LV position (ML) was measured as the distance between the vertical used for the chest depth measurement and the vertical from the mitral valve midpoint.

Using the selected four-chamber view, chest depth (Figure 6-2C) was measured using the vertical from the center of the visible spine to the level of the sternum, while chest width was measured using the maximum transverse internal thoracic diameter. Anterior-posterior LV position was measured using the vertical beginning at the midpoint of the line across the mitral valve plane and terminating at the level of the visible spine. Medial-lateral LV position was measured as the distance between the vertical used for the chest depth measurement and the vertical from the midpoint of the line across the mitral valve plane.

The ratio of LV end-diastolic volume (EDV) to thoracic cross-sectional area (LVEDV thoracic ratio, LVTR), which was approximated as an ellipse using chest depth and width, was used to broadly examine the relationship between LV orientation, LV size, and thoracic area. Last, anterior-posterior and medial-lateral LV positions relative to chest depth and width, respectively, were also calculated. Relative positions were defined from −50% (the right lateral or the posterior aspect) to +50% (the left lateral or the anterior aspect), i.e., with the center of the chest at 0% medial-lateral and 0% anterior-posterior.

While the LV position ranges are of significance for simulation studies, relative position data was considered to be easier for clinicians to interpret than raw position data. Regression analyses between LV position and other measures were therefore performed using the relative position data.

MRI analysis was performed in ImageJ [140] and cvi^{42} (cvi^{42} 2015, Circle Cardiovascular Imaging, Inc., Calgary, Canada). Native QRSd was determined using a 12-lead ECG collected at 1-week post-implant follow-up device check (with CRT turned off) or using the 12-lead ECG recorded immediately before CRT implant. Baseline LVEDV and ejection fraction (EF) were calculated from echocardiograms using the biplane Simpson's method by a single reviewer blinded to knowledge of MRI characteristics.

6.3.3 Statistics

Data are expressed as means ± standard deviations, unless otherwise indicated. Student's unpaired *t*-test was used to analyze unpaired data. Univariate linear regression was used to identify relationships between standard clinical variables (age, BMI, LVEDV, and QRSd), LV orientation and position, and thoracic geometry measures (chest dimensions, LVTR, and relative LV positions). Four multivariate models with backward stepwise elimination until all variables had a p value of < 0.10 were subsequently used to identify significant predictors of LV orientation and relative LV position. Significant predictors from the univariate regression were included in the initial step of each model. In all other analyses, a p value of <0.05 was considered significant. No adjustments for multiple comparisons were made because this study was exploratory in nature. All

statistical analyses were performed in MATLAB (MATLAB and Statistics Toolbox Release 2015b, The MathWorks, Inc., Natick, MA).

Table 6-1. Clinical characteristics of study population

Clinical Characteristics [A]	Value (n = 55)
Male (%)	70
Age (years)	70 ± 11
NYHA Class 3 (%)	69
CAD (%)	56
HTN (%)	60
MI (%)	27
NICM (%)	56
LBBB (%)	73
RBBB (%)	7
NSIVCD (%)	20
Wide (≥150 ms) QRSd (%)	56
Obese (BMI ≥30 kg/m^2) (%)	45
EF (%)	26.6 ± 7

[A] NYHA = New York Heart Association, CAD = coronary artery disease, HTN = hypertension, MI = previous myocardial infarction, NICM = non-ischemic cardiomyopathy, LBBB = left bundle branch block, RBBB = right bundle branch block, and NSIVCD = nonspecific interventricular conduction delay.

6.4 Results

6.4.1 Study population

Fifty-five patients had viable MRIs from less than 2 years prior to CRT implant and met the other inclusion criteria. MRIs used for analyses were acquired 80 ± 134 days prior to CRT implant. The study population clinical characteristics are presented in Table 6-1. Patients were on optimal medical therapy, with 85% on angiotensin-converting enzyme inhibitor or angiotensin receptor blocker therapy and 95% on a beta blocker. No patients had a QRSd of <120 ms. The results for the standard clinical variables, LV orientation and position, and thoracic geometry measures are presented in Table 6-2. Among the factors of

age, BMI, LVEDV, and QRSd, only LVEDV values differed between male and female patients.

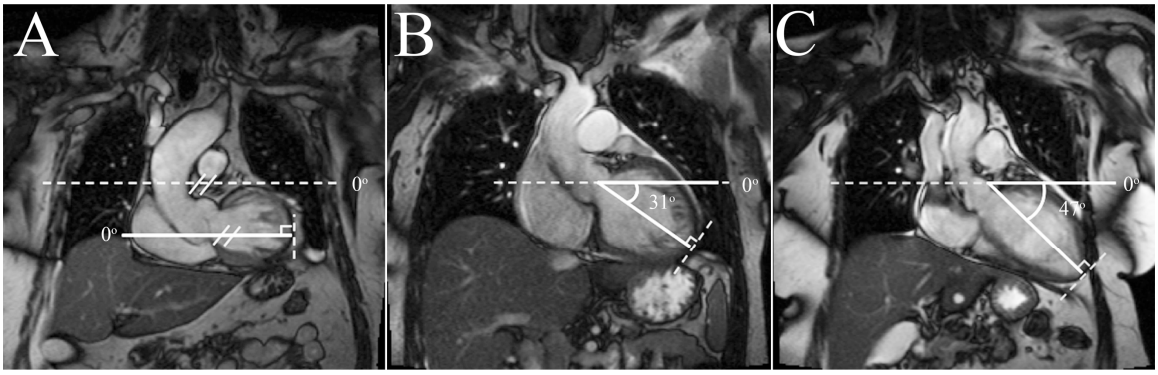

Figure 6-3. Minimum, mean, and maximum frontal plane LV orientation angles
Examples of frontal plane images from a subject with the minimum frontal plane LV orientation angle (0°; A), a subject with the mean frontal plane LV orientation angle (31°; B), and a subject with the maximum frontal plane LV orientation angle (47°; C).

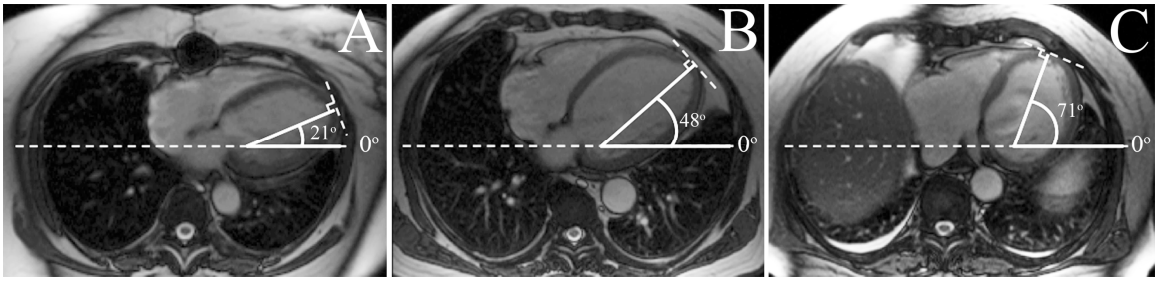

Figure 6-4. Minimum, mean, and maximum transverse plane LV orientation angles
Examples of transverse plane images from a subject with the minimum transverse plane LV orientation angle (21°; A), a subject with the mean transverse plane LV orientation angle (48°; B), and a subject with the maximum transverse plane LV orientation angle (71°; C).

6.4.2 Orientation, position, and thoracic geometry

The average frontal plane LV orientation angle was 31 ± 11°, with a range of 0° to 47°. Figure 6-3 shows images from patients with the minimum, average, and maximum frontal plane LV orientation angles (panels A to C, respectively). Female patients had larger frontal plane orientation angles (i.e., more vertically, or inferiorly, oriented hearts; p = 0.04). The average transverse plane orientation angle was 48 ± 10°, with a range of 21° to

71°. Figure 6-4 shows images from patients with the minimum, average, and maximum transverse plane LV orientation angles (panels A to C, respectively).

Mean chest depth was 18.0 ± 2.3 cm, and mean chest width was 27.4 ± 2.3 cm. Male patients had significantly larger chest widths and depths than females ($p < 0.01$). The average anterior-posterior position of the LV in the transverse plane (defined in Figure 6-2C) was 7.62 ± 1.8 cm (range, 7.9 cm). The average medial-lateral position of the LV in the transverse plane was 2.8 ± 1.1 cm to the left of the sternum (range, 5.6 cm). The average relative anterior-posterior position of the LV in the transverse plane was −7.9% ± 5.6%, i.e., slightly posterior, and the average medial-lateral position of the LV was 10.3% ± 3.9%, i.e., left lateral.

Table 6-2. Results for the standard clinical variables, LV orientation and position, and thoracic geometry measures

Parameter [A]	All (*n*=55)	Males (*n*=39)	Females (*n*=16)	*p*
Age	70 ± 11	69 ± 12	71 ± 9	0.69
BMI (kg/m^2)	29 ± 5	30 ± 4	28 ± 6	0.18
LVEDV (mL)	164 ± 68	175 ± 74	137 ± 41	0.06
QRSd (ms)	153 ± 22	153 ± 20	153 ± 25	0.99
$\theta_{LV,F}$ (°)	31 ± 11	30 ± 11	36 ± 10	**0.04**
$\theta_{LV,T}$ (°)	48 ± 10	49 ± 10	45 ± 10	0.19
CD (cm)	18.0 ± 2.3	19.1 ± 1.5	16.0 ± 2.0	**1.36×10^{-4}**
CW (cm)	27.4 ± 2.3	28.4 ± 1.5	24.8 ± 1.8	**5.10×10^{-7}**
LVTR (cm^{-1})	0.4 ± 0.2	0.4 ± 0.2	0.4 ± 0.1	0.54
AP (cm)	7.6 ± 1.8	8.2 ± 1.4	6.5 ± 1.7	**4.39×10^{-4}**
ML (cm)	2.8 ± 1.1	2.9 ± 1.1	2.6 ± 1.0	0.26
AP_{REL} (%)	−7.9 ± 5.6	−7.2 ± 5.0	−9.6 ± 6.9	0.16
ML_{REL} (%)	10.3 ± 3.9	10.3 ± 4.0	10.2 ± 3.9	0.96

[A] $\theta_{LV,F}$ = frontal plane orientation; $\theta_{LV,T}$ = transverse plane orientation; CD = chest depth; CW = chest width; AP = anterior-posterior position; ML = medial-lateral position; AP_{REL} = relative anterior-posterior position; ML_{REL} = relative medial-lateral position.

The quiver plot in Figure 6-5 illustrates the range of LV orientation angles, relative LV positions, and LVTR values in our study population. Each arrow in the figure

represents an individual patient's data: the location of the tail of each arrow represents relative LV position (medial-lateral and anterior-posterior on the *x* and *y* axes, respectively), the orientation of each arrow is that of the LV in the transverse plane, the length of each arrow is scaled to frontal plane orientation such that longer arrows correspond to smaller angles (i.e., the arrow for a patient with a frontal plane orientation angle of 90° would have no tail), and the color of each arrow represents the LVTR. This figure illustrates that even among clusters of patients with very similar relative LV positions, markedly different frontal and transverse plane LV orientation angles and the full spectrum of LVTR values are apparent.

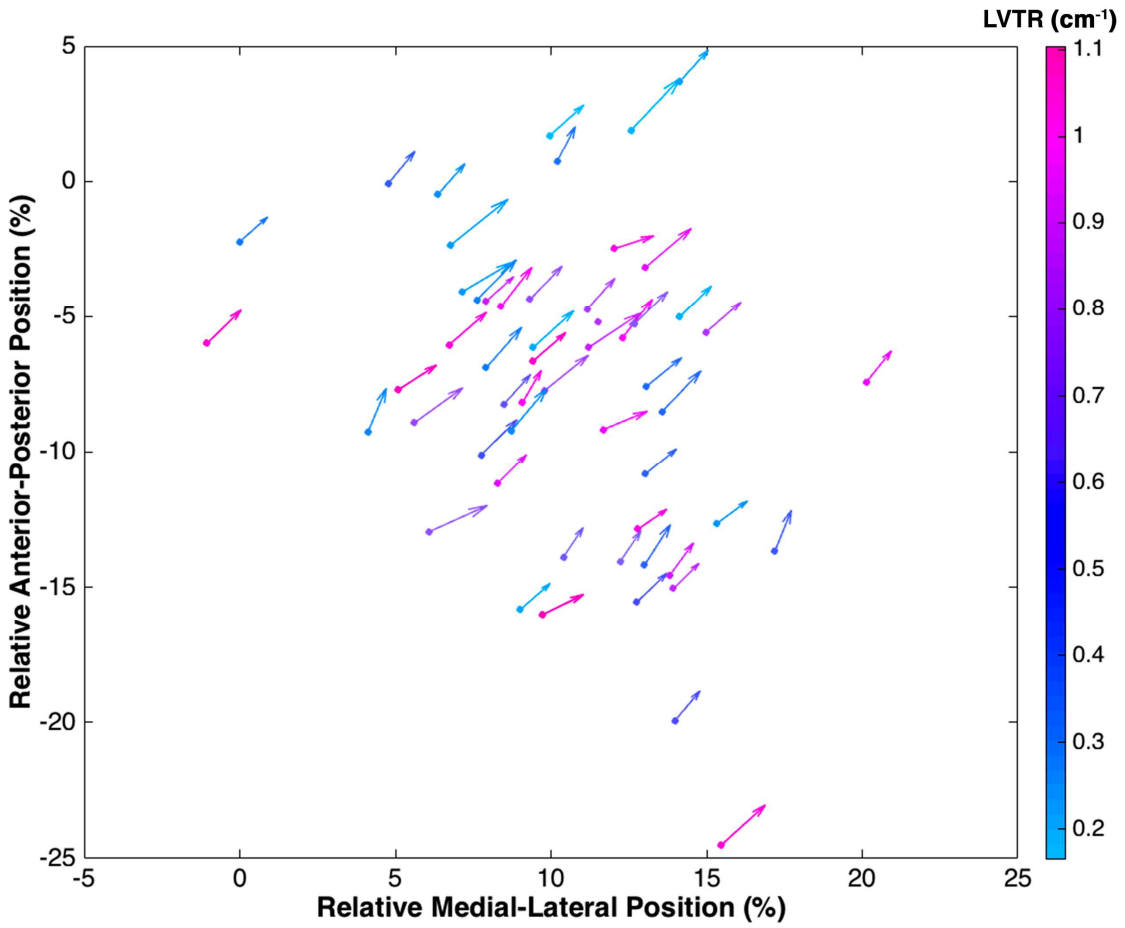

Figure 6-5. Quiver plot of position and orientation data
Quiver plot of relative medial-lateral position (*x*-axis location of arrow tail marker) and relative anterior-posterior position (*y*-axis location of arrow tail marker), transverse plane LV orientation (arrow orientation), frontal plane LV orientation (arrow length), and LVTR (arrow color). Relative anterior-posterior position is scaled from −50% (most posterior) to +50% (most anterior), and relative medial-lateral position is scaled from +50% (leftmost lateral) to −50% (rightmost lateral). Arrow length is scaled such that more horizontally oriented hearts have longer arrows (i.e., the arrow for a frontal plane orientation angle of 90° would have no tail).

Table 6-3. Univariate correlations between standard clinical variables, LV orientation and position, and thoracic geometry measures

Parameters [A,B]										
	ML_{REL}	AP_{REL}	LVTR	CW	CD	$\theta_{LV,T}$	$\theta_{LV,F}$	QRSd	LV EDV	BMI
Age	0.50 (0.03)	**0.76 (0.15)**	**−21.29 (0.09)**	−0.62 (0.02)	0.41 (0.01)	**0.27 (0.09)**	−0.08 (0.01)	-10^{-3} (10^{-5})	**−1.88 (0.09)**	**−0.16 (0.13)**
BMI	−0.09 (10^{-3})	−0.07 (10^{-2})	7.20 (0.05)	**0.82 (0.15)**	**0.97 (0.20)**	−0.49 (0.06)	**−0.64 (0.08)**	0.03 (0.02)	**5.72 (0.17)**	
LV EDV	−1.94 (0.01)	−2.23 (0.03)	**392.19 (0.80)**	**9.25 (0.10)**	8.8 (0.08)	−0.03 (0.04)	10^{-3} (10^{-5})	**1.05 (0.11)**		
QRSd	0.31 (10^{-3})	−0.06 (10^{-4})	35.71 (0.07)	−0.61 (10^{-3})	**2.93 (0.09)**	0.34 (0.03)	0.03 (10^{-4})			
$\theta_{LV,F}$	0.38 (0.02)	−0.37 (0.04)	13.22 (0.04)	**−1.69 (0.13)**	**−1.87 (0.15)**	0.13 (0.02)				
$\theta_{LV,T}$	0.28 (0.01)	−0.01 (10^{-5})	**−20.3 (0.10)**	0.07 (10^{-4})	1.03 (0.05)					
CD	−0.06 (0.01)	**0.17 (0.19)**	−1.48 (0.01)	**0.45 (0.22)**						
CW	−0.06 0.01	0.02 (10^{-3})	−0.33 (10^{-3})							
LVTR	-10^{-3} (10^{-3})	**−0.01 (0.11)**								
AP_{REL}	**−0.41 (0.08)**									

[A] $\theta_{LV,F}$ = frontal plane orientation; $\theta_{LV,T}$ = transverse plane orientation; CD = chest depth; CW = chest width; AP = anterior-posterior position; ML = medial-lateral position; AP_{REL} = relative anterior-posterior position; ML_{REL} = relative medial-lateral position.

[B] Univariate correlations are presented as $a(r^2)$ where a is the coefficient estimate. P values < 0.05 are indicated by bold font.

6.4.3 Predictors of LV orientation and position

Table 6-3 provides a summary of the univariate correlations between each of the standard clinical variables, LV orientation and position, and the thoracic geometry measures. BMI, age, and LVEDV were all modestly correlated with each other: older patients tended to have lower BMIs and smaller LVEDVs, while a larger BMI was independently correlated with a larger LVEDV. Increasing QRSd with increasing LVEDV

was also found. Frontal plane LV orientation significantly correlated with age and chest dimensions; transverse plane orientation correlated with age and LVTR; relative anterior-posterior position correlated with age, chest depth, LVTR, and relative medial-lateral position; and relative medial-lateral position correlated only with relative anterior-posterior position.

Table 6-4. Results from multivariate modeling

Variables included in final model [A,B]	Response variable			
	$\theta_{LV,F}$	$\theta_{LV,T}$	AP_{REL}	ML_{REL}
Age		0.2‡	0.2*	0.1*
BMI		−0.6*	−0.3‡	
LVEDV	0.04*		−0.02*	
$\theta_{LV,F}$	N/A	0.3*		
$\theta_{LV,T}$	0.03*	N/A	−0.2*	
CD	−2.0*	2.8*	1.6*	
CW	−1.2‡			
LVTR		−20.0*		
AP_{REL}		−0.8*	N/A	−0.3*
ML_{REL}			−0.4*	N/A
r^2	0.30	0.42	0.55	0.18
p	**1×10^{-3}**	**1×10^{-4}**	**6×10^{-7}**	**5×10^{-7}**

[A] $\theta_{LV,F}$ = frontal plane orientation; $\theta_{LV,T}$ = transverse plane orientation; CD = chest depth; CW = chest width; AP_{REL} = relative anterior-posterior position; ML_{REL} = relative medial-lateral position.
[B] Regression model coefficient estimates are shown. Variable-specific p values indicated by: ‡ ($0.10 > p \geq 0.05$), * ($0.05 > p$). N/A: Not applicable.

Multivariate models using backward stepwise regression were implemented to determine the most significant predictors of frontal and transverse plane LV orientation and of relative anterior-posterior and medial-lateral position. For each of the four response variables, there were multiple significant but weakly correlated predictors included in the final model. The results are summarized in Table 6-4 and illustrated in Figure 6-6. Frontal plane LV orientation is predicted by LVEDV, transverse plane orientation, chest depth, and chest width ($r^2 = 0.30$, $p = 0.001$). Transverse plane LV orientation is predicted by age,

BMI, frontal plane orientation, chest depth, LVTR, and relative anterior-posterior position ($r^2 = 0.42$, $p < 0.001$). Relative anterior-poster position is predicted by age, BMI, LVEDV, transverse plane orientation angle, chest depth, and relative medial-lateral position ($r^2 = 0.55$, $p < 0.001$); relative medial-lateral position is predicted by age and relative anterior-posterior position ($r^2 = 0.18$, $p = 0.005$).

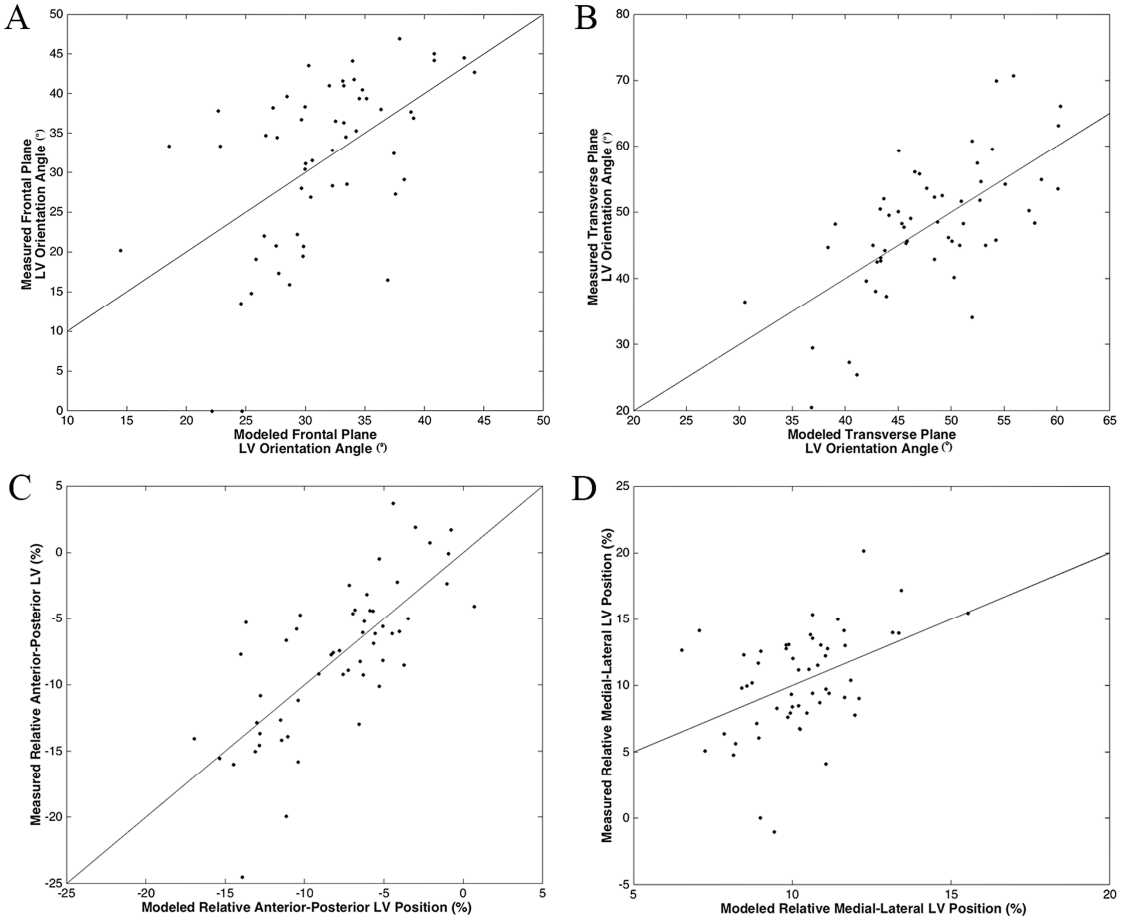

Figure 6-6. Results of multivariate regression
(A) Model of frontal plane orientation. LVEDV, transverse plane orientation, chest depth, and chest width were the significant predictors of frontal plane orientation (solid line shows fit: $r^2 = 0.30$, $p = 0.001$). (B) Model of transverse plane orientation. Age, BMI, frontal plane orientation, chest depth, LVTR, and relative anterior-posterior position were significant predictors of transverse plane orientation (solid line shows fit: $r^2 = 0.42$, $p < 0.001$). (C) Model of relative anterior-posterior position. Age, BMI, LVEDV, transverse plane orientation, chest depth, and relative medial-lateral position were all significant predictors of relative anterior-posterior position (solid line shows fit: $r^2 = 0.55$, $p < 0.001$). (D) Model of relative medial-lateral position. Age and relative anterior-posterior position were significant predictors of relative medial-lateral position (solid line shows fit: $r^2 = 0.18$, $p = 0.005$).

6.5 Discussion

Studies indicate that LV orientation and position may greatly affect the morphology of 12-lead ECGs. Although the 12-lead ECG is a standard tool in the clinical assessment of HF patients [141], the variation in LV orientation and position and any relationship with standard clinical variables or thoracic geometry in this patient population are unknown. The goal of this study was to describe for the first time the frontal and transverse plane LV orientations and the LV positions seen in an advanced systolic HF population. In addition, we wanted to investigate whether orientation or position, and the potential of each for associated confounding effects on 12-lead ECG interpretation, can be predicted by standard clinical variables, such as age, BMI, LV volume, and QRSd, or by thoracic geometry as described by chest dimensions and LVTR. Our results indicate (1) that there is great variation in LV orientation and position in the HF population, (2) that this variation cannot be readily predicted using the clinical variables or thoracic geometry measures investigated in this study, and (3) that the effects of LV orientation and position variation on key 12-lead ECG features documented in previous studies are based on parameter ranges that are reasonable for the HF population.

6.5.1 Comparison of results with available literature

The frontal and transverse plane LV orientation angles found in this study (31 ± 11° and 48 ± 10°, respectively) are in agreement with those reported by Foster et al. for their HF subgroup [130]. In that group of 13 patients, the frontal and transverse plane LV orientation angles were 35 ± 11° and 49 ± 12°, respectively [130]. The ranges of LV

orientation angles determined in our study of an advanced systolic HF population (frontal 47°, transverse 50°), however, were larger than those found by Engblom et al., Foster et al., and Hoekema et al. Engblom et al. reported ranges of 43° and 29° in the frontal and transverse planes, respectively, for their healthy population [127]. Foster et al. reported standard deviations of 6° and 7° for their mixed population of healthy (25%), "in-house" MRI (32%), acute coronary syndrome (26%), and HF (17%) patients [130]. And Hoekema et al. reported standard deviations of 5° and 9° in the frontal and transverse planes, respectively, for their healthy subjects [124]. Notably, Foster et al. found a significant difference between HF patients and healthy subjects only with respect to frontal plane LV orientation angles, but these results may have been limited by small subgroup size ($n = 13$) [130]. Our results broadly suggest that the range of frontal and transverse plane LV orientations may be larger in the HF population. It is possible that heart orientation or position outside the normal range would translate to 12-lead ECG variations that could lead to misdiagnosis. Our LV orientation results provide context for previous simulation study results by MacLeod et al. and Nguyen et al. showing that variation in LV orientation has significant effects on 12-lead ECG features [122, 125]. Those study findings were based on similar or smaller ranges of orientation angles than the values found in our study and on only modulating orientation in the frontal plane [122, 125].

Our chest dimension results are in general agreement with those reported by Laurin et al. for 28 healthy patients (50% males; BMI of 22.5 ± 2.1 kg/m^2), despite the use of external landmarks to measure chest dimensions, the use of subjects in a standing position, and the lower population BMI in that study [142]. The results of our study and those of others

indicate that chest dimensions positively correlate with increased BMI [143]. The average chest depth of our population (18.0 ± 2.3 cm) is consistent with that reported by Laurin et al., which was 15 ± 1.8 cm at the level of the manubrium [142]. The chest widths in our study are also similar to those of Laurin et al. (27.4 ± 2.3 cm vs. 23.4 ± 2.5 cm, respectively) [142].

No studies quantifying interindividual variation in heart position or the relationship between LV position or orientation and thoracic geometry were identified for comparison. As with the LV orientation data, the ranges of anterior-posterior and medial-lateral LV positions in the transverse plane (5.6 cm and 7.9 cm, respectively) found in our study are similar to or larger than those used in simulations by MacLeod et al., Hoekema et al., and Ngyuen et al., who found that alteration in heart position of up to 5 cm and 6 cm, respectively, caused significant changes to 12-lead ECG features, which could not be corrected for by altering 12-lead ECG lead positioning [122-125]. The real-world HF population position data found in our study provides support for the clinical relevance of the previous simulation and canine study findings.

6.5.2 Prediction of LV orientation and position

The interpretation of the uni- and multivariate regression results is made difficult by the weak but significant correlations with multiple significant predictors and by the interplay between these predictors. In the case of LV orientation and position, we believe that an individual's particular progression of HF and his or her unique thoracic geometry combine to create the large range of LV orientations seen in our HF population. Ultimately,

these results and the diverse spectrum of data seen in our study population (illustrated in Figure 6-5) suggest that LV orientation and position cannot be readily predicted for individual HF patients based on either standard clinical variables or the additional thoracic geometry measures used in this study.

6.5.3 Clinical implications

The large ranges of frontal plane LV orientation angles and positions found in our study have been previously shown to impact amplitude-based features of the 12-lead ECG, such as R-wave heights, as the heart is brought closer to or moved farther from the chest wall [125, 144]. These fluctuations are relevant for specific 12-lead ECG-based criteria associated with myocardial infarct size, such as Q-wave area and QRS score [100, 134, 145], and also for highly emphasized elements of 12-lead ECG definitions of underlying conduction disorders, such as QRS notching [125, 146]. The range of transverse plane LV orientation angles documented in Figure 6-4 is also likely significant for the advanced systolic HF population but has not been explored in previous simulation studies. The 50° range in the transverse plane orientation angles suggests large interindividual variability in the location of the heart relative to the (constant) positioning of the 12-lead ECG leads and, in tandem, variability in the regional cardiac activity reflected in each of the standard 12-lead ECG leads. Such variation could result in masking the true underlying electrical conduction behavior, particularly in the case of CRT candidate assessment, where stricter 12-lead ECG criteria are becoming more favored [40, 125]. Previous studies have shown

that adjusting 12-lead ECG electrode positions is not sufficient to account for variation in heart position or frontal or transverse plane LV orientation [124, 125, 129].

In addition to 12-lead ECG interpretation, the variation in LV orientation and position found in our HF population may affect the interpretation of two-dimensional clinical images. Such effects are of particular relevance to the 10 to 15% of HF patients who are candidates for CRT therapy [147, 148]. Recent studies suggest that appropriate LV lead placement during CRT implant is a significant contributor to patient response [26, 149]. But LV lead placement is currently guided by fluoroscopy images, and lead position after implant is typically assessed using chest X-rays, without incorporating any global LV orientation or position data. Assessing LV orientation using MRI prior to CRT implant may facilitate more optimal LV lead placement by (1) providing a more accurate global frame of reference in which to consider the standard target fluoroscopy views and (2) indicating the potential need for less standard views during the procedure. Similarly, a more accurate interpretation of the LV lead position after implant may be achieved by considering chest X-ray findings in concert with orientation data.

6.5.4 Future directions

Studies documenting the effects of LV orientation and position modulation on 12-lead ECG features using simulations or canine models have described effects of significance for clinical diagnoses using LV frontal plane orientation and LV position ranges that are similar to but smaller than those that we found in our HF population. Considering the *in silico* results in the context of our novel findings underscores the potential impact of

orientation and position variation on 12-lead ECG interpretation in a real-world clinical population. Unfortunately, the technology to incorporate LV orientation or position data into 12-lead ECG interpretation is not currently available. Electrocardiographic imaging (ECGi) could be used to account for orientation and position variation by using body surface potentials, a CT scan, and the inverse solution to create a patient-specific model of 12-lead ECG waveforms with respect to the population average orientation and position. This would require (1) the identification of a suitable reference population, (2) the collection of expensive images and of body surface data that is not the standard of care, and (3) the investment of much more time than is required to acquire a 12-lead ECG. As a result, any such ECGi technology would likely be limited to research applications.

It is possible that the progression of HF (e.g., LV dilation), rather than the previously simulated random alterations to LV orientation and position, creates predictable alterations to 12-lead ECG features when the pre-HF or early-stage HF 12-lead ECG is available as a baseline. A study of clinical echocardiograms, MRI data, and 12-lead ECGs collected serially during the progression and treatment of HF could be performed to investigate how LV remodeling may affect orientation or position and thus lead to clinically relevant changes in 12-lead ECG morphology. Such a study would require prospective patient selection and long-term follow-up. As a result, further, larger *in silico* or animal studies varying LV orientation in both the frontal and transverse planes, using the HF population ranges of orientation and position found in our study, and designing simulations to mimic the possible progression of HF, may be the most readily executable method for advancing research in this arena.

In current clinical practice, the potential for abnormal heart orientation or position and subsequent confounding effects on 12-lead ECG-based diagnostics should be considered in HF patient care, particularly in the case of cardiac imaging, as outlined above.

6.5.5 Limitations

A comparison of pre-HF and post-HF 12-lead ECGs and MRI-based orientation and position data was not possible, and healthy controls were not available because this was a retrospective study. In addition, a comparison of cardiac electrical axis by 12-lead ECG with LV orientation was not performed because the pathologic conduction abnormalities in our population would have distorted the cardiac axis results and because numerous previous studies have found no relationship, even in healthy patients, between cardiac position and electrical axis. Last, in some cases, the sternum could not be properly visualized in the transverse plane MRIs because of artifacts created by sternotomy wires. In these instances, the most-medial visible portion of the rib cage was used for the anterior-posterior chest depth measurement.

6.6 Conclusions

The findings of this study indicate that the ranges of LV orientation and position are large in the HF population and cannot be predicted using standard clinical variables or additional thoracic geometry measures. These results suggest that previous *in silico* studies describing significant alterations to 12-lead ECG elements caused by variation in LV orientation and position have real-world clinical implications. Our results also highlight

the need for further studies to better characterize the temporal relationship between the progression of HF, changes in LV orientation and position, and subsequent changes in a patient's 12-lead ECG features.

6.7 Acknowledgements

We thank the UHVC CT/MRI department for their assistance. We have no conflicts of interest.

7 Effects of Cardiac Geometry on the Predictive Value of Body Surface Activation Metrics: A Pilot Study

7.1 Overview

7.1.1 Introduction

A model using body surface activation metrics to predict patient cardiac resynchronization therapy (CRT) outcomes was previously shown to have a response-type classification accuracy (i.e., prediction of patients as responders or non-responders) of 73%. However, previous studies have shown that variations in cardiac geometry can have significant effects on 12-lead electrocardiogram (ECG) metrics, and the extent of similar effects on body surface activation metrics and associated models is unknown. As a result, the current study investigated the influence of atypical cardiac geometry parameter values on the classification accuracy of the CRT outcomes model.

7.1.2 Methods

The model to predict patient CRT reverse remodeling outcomes and classify patients as predicted responders or non-responders was developed and evaluated in a previous study. In a second, retrospective study, eight cardiac geometry parameters were measured from magnetic resonance images (MRIs) in CRT patients. The analyses in this chapter used only patients who were included in both studies. Cardiac geometry parameters were compared between patients correctly classified by the CRT outcomes model and those who were incorrectly classified. Patients with parameters values outside of the mean ± 1 standard deviation (i.e., high or low outlier values) were identified for each cardiac

geometry parameter. Classification error-biased parameters were defined as those for which the proportion of incorrectly classified patients with high or low outlier values was at least 5% larger than that of the correctly classified patients.

7.1.3 Results

Thirty-four patients participated in both studies (21 correctly classified; 13 incorrectly classified). There was a mild bias toward classification error for patients with chest depth, chest width, or LV relative medial-lateral position measurements that were high outlier values. Moreover, there was a prominent bias towards classification error for patients with (1) LV relative anterior-posterior position or (2) LV volume-to-thoracic cross-sectional-area ratio (LVTR) measurements that were high or low outlier values. Among the incorrectly classified patients that had outlier values for the classification error-biased parameters, there was only one patient with an LV reverse remodeling outcome that was close to the cutoff point for classifying CRT response.

7.1.4 Conclusions

The body surface activation metrics used in the CRT outcomes model may be affected by variation in multiple cardiac geometry parameters and may be particularly sensitive to variations in LV relative anterior-posterior position and LVTR. The lack of borderline outcomes in the incorrectly classified patient group and the scale and two-sided (i.e., high and low) nature of the bias for these two parameters suggest that *in silico* and/or canine

studies would be worthwhile to determine the cost-benefit balance of including these parameters in a future model.

7.2 Introduction

This chapter preliminarily investigates the influence of atypical cardiac geometry parameter values on the classification accuracy of a previously developed model of patient cardiac resynchronization therapy (CRT) reverse remodeling outcomes and aims to identify parameters that may be incorporated into the model in the future to improve its performance.

A multivariate regression model using novel body surface activation metrics derived from multichannel electrocardiograms (MECGs) acquired during native conduction was previously developed to predict patient LV reverse remodeling outcomes in the context of CRT candidate evaluation (CRT_{CE}). The CRT_{CE} model had a response-type classification accuracy (i.e., prediction of patients as responders or non-responders) of 73% in a cohort of CRT patients and was significantly more accurate than models based on current standard clinical metrics or on previously developed body surface activation metrics.

Two advantages of the body surface activation metrics used in the CRT_{CE} model are (1) that they that may be noninvasively measured in a routine clinical setting and (2) that they utilize MECG data as a bulk surrogate for local myocardial activity and, therefore, do not require registration to anatomic landmarks or the associated use of costly imaging methods. As a result, however, anatomical factors that may affect the relationship between electrical substrate behavior and the body surface activation metrics are not accounted for.

Canine and *in silico* studies of 12-lead electrocardiograms (ECGs) have shown, for instance, that LV orientation and position (hereafter, cardiac geometry parameters) can have clinically significant effects on QRS complex peak heights, morphology, areas, and duration [120, 122, 125], each of which is incorporated in the MECG-based calculation of one or more of the body surface activation metrics used in the CRT_{CE} model. These metrics are body surface activation duration, posterior ECG QRS complex peak height, and anterior-posterior difference in area under the ECG curve (see Figure 5-2 and Table 5-1).

The relationship between body surface activation metrics and cardiac geometry is particularly relevant to the CRT population because the effects of variation in cardiac geometry are dependent upon the cardiac activation sequence [120, 122], and these patients may experience inconsistent native or paced conduction patterns. Moreover, studies have shown that the ranges of cardiac geometry parameters are large in the CRT population [105].

This chapter compares cardiac geometry parameter values in patients with correct CRT_{CE} model response-type classifications and patients with incorrect response-type classifications. The driving hypotheses for the analyses in this study are that cardiac geometry parameters that affect the accuracy of the CRT_{CE} model may be identified (1) by significantly different values in correctly classified versus incorrectly classified patients and (2) by the presence of a larger proportion of patients with outlier parameter values in the incorrectly classified patient group than the correctly classified group.

7.3 Methods

7.3.1 CRT_{CE} model

The development, structure, and performance of the CRT_{CE} model that was used in this study have been described in detail elsewhere (see Chapter 5). Briefly, a partial least squares regression model of patient LV reverse remodeling outcomes was created using a combination of standard clinical and novel body surface activation metrics acquired during native conduction. The body surface activation metrics were derived from MECGs acquired with a custom investigational body surface mapping system, and model performance was retrospectively assessed in a cohort of 71 CRT patients (see Table 5-3) who participated in a previous study at United Heart and Vascular Clinic (UHVC) in St. Paul, MN[10]. Patients in whom there was a reduction in LV end-systolic volume (LVESV) of at least 15% at 6 months after CRT implant were defined as responders [109-111]. The CRT_{CE} model had a response-type classification accuracy of 73%.

7.3.2 Cardiac geometry parameters

The methods for the MRI-based measurement of the cardiac geometry parameters used in this study have been described previously [105] (see Chapter 6). The measured parameters were frontal and transverse plane LV orientation, chest width and depth, LV

[10] Data from this previous prospective study will be used throughout this dissertation. The study in question was initiated and conducted by the research department at United Heart and Vascular Clinic; study funding and equipment were provided by Medtronic, PLC. Initial results from this study were published in Gage et al. [56]

relative anterior-posterior and medial-lateral position, and the ratio of LV end-diastolic volume to chest area (LVTR). All of these parameters were previously measured in a retrospective study of 55 CRT patients who had participated in a different, earlier study at UHVC in St. Paul, MN, between 2013 and 2015. At the time of MRI acquisition, all of these patients had advanced systolic heart failure. Body mass index (BMI) was also calculated for each patient in accordance with the standard clinical formula [150]. Notably, this previous cardiac geometry study showed that none of the investigated parameters were correlated with each other (maximum univariate $r^2 = 0.20$) [105] (see Chapter 6).

7.3.3 Comparison of cardiac geometry parameter values

The aforementioned MRI-derived cardiac geometry parameters of patients that were included in both the CRT_{CE} model evaluation study and in the cardiac geometry study were compared in patients with correct CRT_{CE} model response-type classifications (i.e., correct prediction of patients as responders or non-responders) and patients with incorrect response-type classifications. First, values for each parameter were compared between the two groups. Second, patients with outlier parameter values compared to the all-patients average value were identified. Patients with high outlier values (i.e., values greater than the parameter mean plus one standard deviation) were distinguished from patients with low outlier values (i.e., values less than the parameter mean minus one standard deviation). The proportions of patients with outlier values of either type were compared between the correctly and incorrectly classified groups for each of the cardiac geometry parameters. Classification error-biased parameters were defined as those for which the proportion of

incorrectly classified patients with high or low outlier values was at least 5% larger than that of the correctly classified patients.

7.3.4 Statistics

Data are expressed as means ± standard deviations. Student's unpaired *t*-test or a one-way analysis of variance (ANOVA) combined with multiple pairwise comparisons using Tukey's difference criterion was used to analyze unpaired data. All statistical analyses were performed using MATLAB (MATLAB and Statistics Toolbox Release 2017a, The MathWorks, Inc., Natick, MA). A p value <0.05 was considered significant.

7.4 Results

7.4.1 Study population

There were 34 patients in both the CRT_{CE} model evaluation study and the cardiac geometry study. The clinical characteristics of these patients are presented in Table 7-1. Of these patients, 21 (62%) were correctly classified by the CRT_{CE} model as responders or non-responders, and 13 (38%) were incorrectly classified.

7.4.2 Comparison of cardiac geometry parameter values

Table 7-2 shows the average frontal and transverse plane LV orientations, chest width and depth, LV relative anterior-posterior and medial-lateral positions, LVTR, and BMI for the correctly classified patient group and the incorrectly patient classified group. None of

the cardiac geometry parameters investigated were significantly different between the two groups.

Table 7-1. Clinical characteristics of study population

Characteristic A	Value B (n = 34)
Age (y)	68 ± 9
Males	22 (65%)
NYHA class III	22 (65%)
ICM	14 (41%)
Beta-blocker	33 (97%)
ACEI/ARB	32 (94%)
QRSd (ms)	155 ± 20
LBBB	28 (82%)
RBBB	2 (6%)
IVCD	4 (12%)
LVESV (mL)	127 ± 70
EF (%)	27 ± 7

[A] NYHA = New York Heart Association; ICM = ischemic cardiomyopathy; ACEI/ARB = angiotensin-converting enzyme inhibitor/angiotensin II receptor blocker; LBBB = left bundle branch block; RBBB = right bundle branch block; IVCD = (nonspecific) intraventricular conduction delay; LVESV = left ventricular end-systolic volume; EF = ejection fraction.
[B] Values are presented as mean ± STD or as count (%).

Table 7-2. Results for cardiac geometry parameters

Parameter [A]	All (*n*=34)	CCP group [B] (*n*=21)	ICP group [B] (*n*=13)	*p*
$\theta_{LV,F}$ (°)	32 ± 11	30 ± 11	34 ± 12	0.32
$\theta_{LV,T}$ (°)	48 ± 10	48 ± 10	47 ± 9	0.74
CD (cm)	17.5 ± 2.4	17.2 ± 2.3	17.9 ± 2.6	0.42
CW (cm)	27.2 ± 2.5	26.8 ± 2.4	27.9 ± 2.7	0.24
AP_{REL} (%)	−8.3 ± 6.1	−8.5 ± 5.3	−8.0 ± 7.3	0.83
ML_{REL} (%)	10.0 ± 3.5	9.8 ± 3.9	10.3 ± 2.9	0.71
LVTR (cm^{-1})	0.4 ± 0.2	0.5 ± 0.1	0.4 ± 0.2	0.88
BMI (kg/m^2)	30 ± 5	29 ± 5	31 ± 5	0.28

[A] $\theta_{LV,F}$ = frontal plane orientation; $\theta_{LV,T}$ = transverse plane orientation; CD = chest depth; CW = chest width; AP_{REL} = relative anterior-posterior position; ML_{REL} = relative medial-lateral position.
[B] CCP: Correctly classified patients; ICP: Incorrectly classified patients.

Table 7-3. Proportions of correctly classified patients and incorrectly classified patients with outlier values for cardiac geometry parameters

	Proportion (%) of CCPs [A] with		Proportion (%) of ICPs [A] with	
Parameter [B]	HOVs	LOVs	HOVs	LOVs
$\theta_{LV,F}$ (°)	14.3	28.6	15.4	7.7
$\theta_{LV,T}$ (°)	19.0	14.3	7.7	15.4
CD (cm)	9.5	19.0	15.4	23.1
CW (cm)	14.3	19.0	23.1	15.4
AP_{REL} (%)	4.8	9.5	23.1	23.1
ML_{REL} (%)	14.3	19.0	23.1	7.7
LVTR (cm^{-1})	9.5	0.0	15.4	30.8
BMI (kg/m^2)	19.0	19.0	7.7	7.7

[A] CCP = correctly classified patients (n = 21); ICP = incorrectly classified patients (n = 13); HOV = patients with high outlier parameter values; LOV = patients with low outlier parameter values; ICP-biased parameters are indicated with shading.
[B] $\theta_{LV,F}$ = frontal plane orientation; $\theta_{LV,T}$ = transverse plane orientation; CD = chest depth; CW = chest width; AP_{REL} = relative anterior-posterior position; ML_{REL} = relative medial-lateral position.

Table 7-3 shows the proportions of patients who had high and low outlier values in the incorrectly classified and the correctly classified groups for each of the cardiac geometry parameters. Five classification error-biased cardiac geometry parameters were identified, and these are indicated with shading in Table 7-3. There was a mild classification error bias of about 5% to 10% for patients with chest depth, chest width, or LV relative medial-lateral position measurements that were high outlier values. Furthermore, there was a prominent bias of up to 31% for patients with LV relative anterior-posterior position and LVTR measurements that were high or low outlier values. Notably, no incorrectly classified patients were uniquely characterized by high outlier values for chest width or LV relative medial-lateral position but rather also had outlier values for one of the other classification error-biased parameters (i.e., chest depth, LV relative anterior-posterior position, and/or LVTR). In addition, among the patients with outlier values for the classification error-biased parameters, there was only one patient with an LV reverse

remodeling outcome that was close to the cutoff point for classifying CRT response (i.e., with an LVESV outcome between –10% and –20%).

7.5 Discussion

The presence of multiple classification error-biased parameters, as identified in this study, suggests that some of the geometry parameters investigated (specifically, chest depth and width, LV relative anterior-posterior and medial-lateral positions, and LVTR) may have a significant impact on the classification accuracy of the CRT_{CE} model even though none of the cardiac geometry values were, on the whole, significantly different between the group of incorrectly classified patients and the group of correctly classified patients. Furthermore, the body surface activation metrics used in the CRT_{CE} outcomes model may be particularly sensitive to variations in LV relative anterior-posterior position and in LVTR, as evidenced by their two-sided (i.e., high and low outlier) classification error bias, indicating that for these parameters the range of values that can be accommodated by the current model is more limited than that of other parameters. The scale of the difference in the proportions of incorrectly classified patients with LV relative anterior-posterior position or LVTR outlier values compared to proportions in the correctly classified group also suggests particular sensitivity of the CRT_{CE} model to these parameters. Last, inclusion of chest width and LV relative medial-lateral position may not be necessary in a future model because all incorrectly classified patients with high outlier values for these parameters also had outlier values for the other classification error-biased parameters.

Notably, only one of the incorrectly classified patients with outlier values for the classification error-biased parameters had an LVESV outcome close to the CRT response classification cutoff, which suggests that outlier values for any of the classification error-biased parameters likely create an error in predicted outcome values that is significant for accurate response-type classification.

The results of this analysis do not eliminate the possibility that other cardiac geometry parameters may affect body surface activation metrics. Ultimately, in spite of the associated time and effort required, this pilot study indicates that *in silico* or canine studies, similar to those performed with 12-lead ECGs, should be performed to determine the scale of cardiac geometry effects on MECG-derived body surface activation metrics.

There are a number of practical limitations to incorporating MRI-derived cardiac geometry parameters into the CRT_{CE} outcomes model or a similar model in the future. Importantly, these limitations are not caused by the inclusion of multiple MRI-derived parameters but result from the inclusion of even one such parameter. MRI data requires costly imaging and software as well as time-consuming offline analysis of the images. In addition, only 48% of the patients that met the criteria for the CRT_{CE} model evaluation study were also included in the LV orientation and thoracic geometry study. While this is an important limitation of the current findings, it also highlights that, based on the current standard of clinical care at UHVC, MRI data may not be available for many CRT candidates. This proportion may vary considerably from clinic to clinic.

7.5.1 Limitations

In addition to the small patient population used in this study, it is noteworthy that the CRT_{CE} model response-type classification accuracy in this patient subset (62%) was substantially lower than that for the original cohort of 71 patients, which was 72%.

7.6 Conclusion

The results of this pilot study suggest that the accuracy of the previously developed CRT_{CE} outcomes model may be improved by the inclusion of some MRI-derived cardiac geometry parameters, particularly LV relative anterior-posterior position and LVTR. Undertaking *in silico* and/or canine studies would be worthwhile to clarify these results and determine the cost-benefit balance of including these parameters in a future CRT_{CE} model.

8 Conclusions and Future Directions

8.1 Overview

Cardiac resynchronization therapy (CRT) is intended to ameliorate intra- and interventricular electrical dyssynchrony and improve systolic function in heart failure (HF) patients. In spite of the success of CRT in many multicenter studies, 30% of CRT patients fail to respond to the therapy. Lack of CRT patient response is linked with the limited sensitivity and spatial resolution of the 12-lead ECG and specifically of the QRS complex duration (QRSd) and morphology, which are the standard clinical metrics for evaluation of candidates for and patients with CRT devices. A promising alternative to the 12-lead ECG is body surface activation mapping derived from multichannel electrocardiograms (MECGs). However, in order to be a viable solution to CRT non-response, body surface activation data must be not only better correlated with patient CRT outcomes than current 12-lead ECG measures but also readily measurable in a real-time clinical setting. This thesis evaluated an investigational body surface mapping system against these criteria by developing automated QRS complex analysis algorithms for MECGs, by evaluating the reproducibility of body surface activation metrics, and by developing new metrics to predict patient CRT outcomes. This work also explored the use of body surface activation maps to characterize electrical sequences and dyssynchrony in the nonspecific intraventricular conduction delay (IVCD) subpopulation and evaluated the effects of patient cardiac geometry on the predictive value of body surface activation metrics.

8.2 Automated MECG analysis algorithms

Use of body surface activation maps and metrics in a clinical setting requires real-time analysis of MECGs for detection of QRS complexes and calculation of associated metrics. Current QRS complex detection algorithms are designed specifically for 12-lead ECG applications, are typically validated with single-channel 12-lead ECG data, and struggle with many ECG features that are prevalent in the CRT population (i.e., paced complexes, wide complexes, negative polarity complexes, etc.). This thesis developed and validated automated QRS complex detection and QRSd measurement algorithms specifically designed for the challenges of MECGs acquired in the CRT population. The algorithm performed as well as current state-of-the-art algorithms for 12-lead ECGs and within the variation found in clinical 12-lead ECG QRSd measurements and could be implemented in real time.

Notably, the QRS detection and duration measurement algorithms were designed and validated specifically with MECGs acquired with the custom ECG Belt investigational body surface mapping system. As a result, the performance of the algorithms when applied to MECGs acquired with a different size, arrangement, or type of electrode array is unknown. The MECG electrode arrays used for electrocardiographic imaging or pre-procedural mapping vary considerably in the literature, and the morphological channel grouping and averaging methods used to facilitate QRS complex detection and classification would likely be particularly susceptible to such variations. The identification of array-specific QRS complex borders may also be affected by MECG arrays with fewer

channels. Use of a different amplifier or data acquisition at a different sampling rate or bit resolution could also affect the accuracy of either algorithm.

The QRS complex detection and measurement algorithms were validated with MECGs recorded over 15 to 20 seconds, and the validation studies showed that the QRS complex detection accuracy was negatively affected by the presence of fewer QRS complexes of the predominant morphology (PM). These results suggest that the algorithms' performance would be reduced if the MECGs were recorded for a shorter period of time in order to improve data acquisition efficiency. However, the results of Chapter 3 emphasize the need for analysis of multiple QRS complexes in the calculation of body surface activation metrics in order to generate reproducible results.

The QRS complex detection and classification algorithm only discriminates between the QRS complexes with the predominant morphology and those with outlier morphologies (OM). The algorithm also reports the OM complex burden, which is clinically relevant because even a 1.5% OM complex burden (i.e., proportion of un-paced beats) is significantly detrimental to CRT patient symptomatic response and mortality [151]. However, corrective CRT setting selection to reduce the OM complex burden would require further information about the physiologic source of the OM complexes. The QRS complex classification structure could be further developed to identify and report specific types of conduction, such as premature ventricular contractions, premature atrial contractions, fusion beats, or breakthrough native conduction. Development of such additional algorithm functionality would create a tool for CRT setting selection that could be used to identify not only the CRT settings that ameliorate the native dyssynchrony but

also those that improve the consistency of the therapy being delivered. Targeted MECG acquisition in patients with suboptimal pacing percentages and ectopic conduction would be needed for the development and validation of a more specific QRS complex classifier.

8.3 Reproducibility of body surface activation metrics

In order to compare metric values associated with different CRT settings, the metric values associated with each setting must be reproducible. The large interobserver variation in 12-lead ECG QRSd values is an impediment to their clinical use for predicting patient CRT outcomes [36]. This thesis assessed the reproducibility of the SDAT (standard deviation of body surface activation times) metric to identify noise sources that may be detrimental to SDAT reproducibility. The associated analysis showed (1) that electrode-torso contact can vary substantially during MECG acquisition, with significant effects on SDAT values and (2) that multi-beat averaging can be leveraged to substantially reduce beat-to-beat variation in SDAT values from physiologic or pseudo-physiologic noise.

The effects of both multi-beat averaging and electrode loss were evaluated only with respect to the SDAT metric and not the subsequently developed metrics described in Chapter 5. Some metrics that are based on multichannel averages, such inter-activation event distance or the average area under the ECG curve, may be more robust to electrode loss than the standard-deviation-based SDAT. On the other hand, metrics based on smaller subsets of the electrode array, such as the left-thorax activation time or the anterior peak height, could be particularly sensitive to electrode loss localized to the anterior array due to its lower proportion of electrodes relative to the total number of electrodes (17 of 53) in

the array used with the ECG Belt system. Future studies are needed to determine the effects of electrode loss and other noise sources on the metrics used to predict patient outcomes described in Chapter 5. The results of such work could be used to generate variable weights and then to repeat the regression model development described in Chapter 5 to identify the set of variables that is not only the most predictive but also the most reproducible.

Electrode loss was also evaluated using only the ECG Belt electrode array, and the reproducibility of any body surface activation metric could be affected by alternative array designs, electrode types, and/or adhesives used. Pertinently, the MECGs available for electrode-loss simulations did not permit evaluation of alternative arrays using more than 53 electrodes. The electrode-loss simulations also utilized a random-loss strategy, instead of one based on the most commonly lost electrodes. A retrospective analysis of the most frequently lost electrodes could be helpful to inform future electrode array designs, but the inter-patient variation is likely to be too large to make such an approach successful. However, evaluation of electrode loss in patient subgroups defined by gender, body mass index, and height could be used to create multiple electrode array designs that would improve electrode-torso contact for the range of body habitus seen in the CRT population. Success of such an analysis, however, could be hindered by inconsistent placement of the ECG Belt electrode array on the torso, which is not determined by any anatomical landmarks and is occasionally adjusted for patient comfort.

8.4 Characterization of the activation in the IVCD subpopulation

The benefit of CRT in IVCD patients is uncertain, but studies suggest that there is an IVCD subpopulation that would benefit from CRT due to high electrical dyssynchrony and LBBB-like activation sequences. However, there are no current criteria to prospectively identify such patients. This thesis investigated if mapped body surface activation sequences can be used to identify LBBB-like IVCD patients and if the identified LBBB-like IVCD patients had more dyssynchrony than other IVCD patients based on body surface activation metrics. That pilot study demonstrated (1) that use of body surface activation mapping to identify LBBB-like IVCD patients is feasible and (2) that the LBBB-like IVCD patients had significantly more dyssynchrony by body surface activation metrics than the other IVCD patients and should, therefore, be more likely to respond to CRT.

The pilot study in Chapter 4 included 85 CRT patients, but only 17 of those (20%) were IVCD patients. In addition, CRT outcomes, such as LV reverse remodeling data, were not available, and activation sequences were grouped manually and with *a priori* knowledge of the patients' 12-lead ECG morphologies. A more rigorous future study (1) would utilize a blinded approach to grouping, such as machine learning, (2) would evaluate more IVCD patients, and (3) would incorporate and compare CRT outcomes between LBBB-like IVCD patients and other IVCD patients.

8.5 New metrics to predict patient CRT outcomes

The current standard, 12-lead ECG, metrics are limited in their ability to predict patient CRT outcomes. The development of new, noninvasively acquired metrics that are predictive of patient CRT outcomes in the context of both CRT candidate evaluation (CRT_{CE}) and CRT setting selection (CRT_{SS}) is critical to addressing patient non-response to therapy. This thesis described seven novel body surface activation metrics, each of which was designed to reflect ECG features that have been shown to be relevant to electrophysiologic substrate behavior in the CRT population and that were not captured by previous body surface activation metrics. The new metrics were used to develop enhanced CRT_{CE} and CRT_{SS} models that were each nearly twice as well correlated with patient LV reverse remodeling outcomes as models using standard clinical variables or previously developed body surface activation metrics.

The novel body surface activation metrics and the associated enhanced CRT_{CE} and CRT_{SS} models were evaluated only in the context of LV reverse remodeling outcomes, using a retrospective analysis of only 71 patients who had already received CRT devices. Because the enhanced models were each developed with partial least squares regression, larger retrospective studies are needed to further train the models and confirm their accuracy prior to undertaking a prospective study. The models could also be expanded to predict additional outcome variables, such as acute changes in blood pressure, which would reflect hemodynamic response. Furthermore, the relationship between accurately predicted LV reverse remodeling outcomes and clinical changes in HF status could be investigated by measuring clinical outcomes such as all-cause mortality and hospitalization rates.

The novel body surface activation metrics used in the enhanced CRT_{CE} and CRT_{SS} models were developed and evaluated using MECGs collected with the ECG Belt investigational body surface mapping system, and the performance of the enhanced models was compared only to standard clinical variables and previously developed body surface activation metrics. As a result, the effects of different MECG electrode array designs on the predictive value of the new metrics is unknown. In addition, the performance of the new body surface activation metrics relative to that of other new metrics developed by other groups, such as the VCG-based QRS_{AREA} or the 12-lead-ECG-based QRS integral is unknown. Limited studies with all three systems, 12-lead ECGs, VCGs, and MECGS, showed that the quantity and placement of electrodes in MECG systems make MECGs more sensitive to electrical substrate behavior than either of the other systems.

The effects of cardiac geometry on the predictive value of the novel body surface activation metrics and the associated enhanced CRT_{CE} and CRT_{SS} models may be significant, as indicated by the pilot study in Chapter 7 and analogous work with 12-lead ECGs, but this matter requires further investigation. Future studies using clinical cardiac magnetic resonance images (MRIs) and electrophysiologic simulation software, such as SCIRun, are needed to more thoroughly investigate which body surface activation metrics are affected by variations in which cardiac geometry parameter(s) and how these effects translate to the accuracy of the CRT_{CE} and CRT_{SS} models. Notably, because previous work has shown that cardiac geometry parameters are not well correlated with each other [105], the net effects of alterations to multiple parameters would also need to be evaluated, and a multidimensional probability density approach would be needed to create a tractable

parameter space to pursue. Due to the resource-intensive nature of collecting MRIs and measuring the requisite cardiac geometry parameters, it would be advantageous to identify any and all body surface activation metrics that are relatively insensitive to changes in cardiac geometry, which would then eliminate the need to make MRI-based measurements and incorporate cardiac geometry parameters into the enhanced CRT_{CE} and CRT_{SS} models. The results of the aforementioned simulation studies could be used to generate corresponding variable weights and then to repeat CRT_{CE} and CRT_{SS} model development to identify the set of variables that is not only the most predictive but also the most robust. As with the metrics themselves, the effects of variation in cardiac geometry would depend on the design of the electrode array.

8.6 Significance and broader impacts

Over half a million patients have received CRT devices in the United States in the past decade, but 30% of these patients do not respond to the therapy. Moreover, CRT non-response is not only an issue of high prevalence but also of serious consequence: patients who fail to respond to CRT have a 5-year survival probability of only 50%, while the survival rate for responders is over 90% [25]. CRT non-response is due, in part, to the limitations of the 12-lead ECG, which is the main clinical tool used to assess candidates for and patients with CRT devices. Previous studies have indicated that body surface activation maps and metrics derived from MECGs (1) may be more sensitive to relevant electrical substrate behavior than the 12-lead ECG and (2) may have better spatial resolution than the 12-lead ECG, while still enabling the noninvasive evaluation of CRT

patients in a clinical setting. This thesis built upon previous findings by (1) creating an MECG analysis algorithm that is at least as accurate as current clinical analogs for 12-lead ECGs, (2) demonstrating the utility of body surface activation maps for characterizing a poorly understood CRT subpopulation, and (3) developing models of CRT patient LV reverse remodeling outcomes designed for candidate evaluation and for setting selection that reduced misclassification of predicted CRT candidate response type by 64% and were significantly better correlated with patient outcomes than models using current clinical metrics. Ultimately, this work holistically advances the evidence and methods for applying body surface activating mapping technology in the CRT population.

References:

[1] N. Akarachantochote, S. Chadcham, and K. Saithanu, "Cutoff threshold of variable importance in projection for variable selection," *International Journal of Pure and Applied Mathematics,* vol. 94, no. 3, pp. 307-322, 2014 2014.

[2] M. Farres, S. Platikanov, S. Tsakovski, and T. R., "Comparison of the variable importance inprojection (VIP) and of the selectivity ratio (SR) methods for variable selection and interpretation," *Journal of Chemometrics,* vol. 29, pp. 528-536, July 2015 2015.

[3] T. Mehmood, K. H. Liland, L. Snipen, and S. Sæbø, "A review of variable selection methods in Partial Least Squares Regression," *Chemometrics and Intelligent Laboratory Systems,* vol. 118, pp. 62-69, 2012 2012.

[4] T. Mehmood, H. Martens, S. Saebo, J. Warringer, and L. Snipen, "A Partial Least Squares based algorithm for parsimonious variable selection," *Algorithms Mol Biol,* vol. 6, no. 1, p. 27, Dec 5 2011.

[5] G. Palermo, P. Piraino, and H. D. Zucht, "Performance of PLS regression coefficients in selecting variables for each response of a multivariate PLS for omics-type data," *Adv Appl Bioinform Chem,* vol. 2, pp. 57-70, 2009.

[6] M. Writing Group *et al.*, "Heart Disease and Stroke Statistics-2016 Update: A Report From the American Heart Association," *Circulation,* vol. 133, no. 4, pp. e38-360, Jan 26 2016.

[7] P. A. Iaizzo, "Handbook of cardiac anatomy, physiology, and devices." New York, NY: Springer, 2009, p.^pp. Pages.

[8] K. Vernooy, C. J. van Deursen, M. Strik, and F. W. Prinzen, "Strategies to improve cardiac resynchronization therapy," *Nat Rev Cardiol,* vol. 11, no. 8, pp. 481-93, Aug 2014.

[9] L. Littmann and J. D. Symanski, "Hemodynamic implications of left bundle branch block," *J Electrocardiol,* vol. 33 Suppl, pp. 115-21, 2000.

[10] J. J. Blanc, M. Fatemi, V. Bertault, F. Baraket, and Y. Etienne, "Evaluation of left bundle branch block as a reversible cause of non-ischaemic dilated cardiomyopathy with severe heart failure. A new concept of left ventricular dyssynchrony-induced cardiomyopathy," *Europace,* vol. 7, no. 6, pp. 604-10, Nov 2005.

[11] J. N. Cohn, R. Ferrari, and N. Sharpe, "Cardiac remodeling--concepts and clinical implications: a consensus paper from an international forum on cardiac remodeling. Behalf of an International Forum on Cardiac Remodeling," *J Am Coll Cardiol,* vol. 35, no. 3, pp. 569-82, Mar 1 2000.

[12] L. Bacharova *et al.*, "Second statement of the working group on electrocardiographic diagnosis of left ventricular hypertrophy," *J Electrocardiol,* vol. 44, no. 5, pp. 568-70, Sep-Oct 2011.
[13] D. G. Strauss, "Differentiation between left bundle branch block and left ventricular hypertrophy: implications for cardiac resynchronization therapy," *J Electrocardiol,* vol. 45, no. 6, pp. 635-9, Nov-Dec 2012.
[14] F. Tournoux *et al.*, "Concordance between mechanical and electrical dyssynchrony in heart failure patients: a function of the underlying cardiomyopathy?," *J Cardiovasc Electrophysiol,* vol. 18, no. 10, pp. 1022-7, Sep 2007.
[15] W. T. Abraham *et al.*, "Cardiac resynchronization in chronic heart failure," *N Engl J Med,* vol. 346, no. 24, pp. 1845-53, Jun 13 2002.
[16] F. Zannad *et al.*, "Left bundle branch block as a risk factor for progression to heart failure," *Eur J Heart Fail,* vol. 9, no. 1, pp. 7-14, Jan 2007.
[17] M. O. Sweeney and F. W. Prinzen, "Ventricular pump function and pacing: physiological and clinical integration," *Circ Arrhythm Electrophysiol,* vol. 1, no. 2, pp. 127-39, Jun 1 2008.
[18] S. Baldasseroni *et al.*, "Left bundle-branch block is associated with increased 1-year sudden and total mortality rate in 5517 outpatients with congestive heart failure: a report from the Italian network on congestive heart failure," *Am Heart J,* vol. 143, no. 3, pp. 398-405, Mar 2002.
[19] E. Cingolani, J. I. Goldhaber, and E. Marban, "Next-generation pacemakers: from small devices to biological pacemakers," *Nat Rev Cardiol,* vol. 15, no. 3, pp. 139-150, Mar 2018.
[20] J. Gorcsan, 3rd and H. Tanaka, "Echocardiographic assessment of myocardial strain," *J Am Coll Cardiol,* vol. 58, no. 14, pp. 1401-13, Sep 27 2011.
[21] J. G. Cleland *et al.*, "The effect of cardiac resynchronization on morbidity and mortality in heart failure," *N Engl J Med,* vol. 352, no. 15, pp. 1539-49, Apr 14 2005.
[22] A. J. Bank, R. M. Gage, and B. Olshansky, "On the underutilization of cardiac resynchronization therapy," *J Card Fail,* vol. 20, no. 9, pp. 696-705, Sep 2014.
[23] K. Noyes *et al.*, "Cost-effectiveness of cardiac resynchronization therapy in the MADIT-CRT trial," *J Cardiovasc Electrophysiol,* vol. 24, no. 1, pp. 66-74, Jan 2013.
[24] A. Auricchio and F. W. Prinzen, "Non-responders to cardiac resynchronization therapy: the magnitude of the problem and the issues," *Circ J,* vol. 75, no. 3, pp. 521-7, 2011.
[25] P. Palmisano *et al.*, "Reduced long-term overall mortality in heart failure patients with prolonged QRS treated with CRT combined with ICD vs. heart failure patients with narrow QRS treated with ICD only," *Europace,* vol. 18, no. 9, pp. 1374-82, Sep 2016.

[26] J. P. Singh *et al.*, "Left ventricular lead position and clinical outcome in the multicenter automatic defibrillator implantation trial-cardiac resynchronization therapy (MADIT-CRT) trial," *Circulation,* vol. 123, no. 11, pp. 1159-66, Mar 22 2011.

[27] W. W. Brabham and M. R. Gold, "The role of AV and VV optimizaiton for CRT," *Journal of Arrhythmia,* vol. 29, no. 3, pp. 153-161, June 2013 2013.

[28] W. Mullens *et al.*, "Insights from a cardiac resynchronization optimization clinic as part of a heart failure disease management program," *J Am Coll Cardiol,* vol. 53, no. 9, pp. 765-73, Mar 3 2009.

[29] M. Lunati *et al.*, "Clinical Relevance Of Systematic CRT Device Optimization," *J Atr Fibrillation,* vol. 7, no. 2, p. 1077, Aug-Sep 2014.

[30] M. Brignole *et al.*, "2013 ESC guidelines on cardiac pacing and cardiac resynchronization therapy: the task force on cardiac pacing and resynchronization therapy of the European Society of Cardiology (ESC). Developed in collaboration with the European Heart Rhythm Association (EHRA)," *Europace,* vol. 15, no. 8, pp. 1070-118, Aug 2013.

[31] A. E. Epstein *et al.*, "2012 ACCF/AHA/HRS focused update incorporated into the ACCF/AHA/HRS 2008 guidelines for device-based therapy of cardiac rhythm abnormalities: a report of the American College of Cardiology Foundation/American Heart Association Task Force on Practice Guidelines and the Heart Rhythm Society," *J Am Coll Cardiol,* vol. 61, no. 3, pp. e6-75, Jan 22 2013.

[32] S. S. Barold and B. Herweg, "Usefulness of the 12-lead electrocardiogram in the follow-up of patients with cardiac resynchronization devices. Part II," *Cardiol J,* vol. 18, no. 6, pp. 610-24, 2011.

[33] A. van Stipdonk, S. Wijers, M. Meine, and K. Vernooy, "ECG Patterns in Cardiac Resynchronization Therapy," *Journal of Atrial Fibrillation,* vol. 7, no. 6, p. 6, Apr-May 2015 2015.

[34] E. B. Engels, M. Mafi-Rad, A. M. van Stipdonk, K. Vernooy, and F. W. Prinzen, "Why QRS Duration Should Be Replaced by Better Measures of Electrical Activation to Improve Patient Selection for Cardiac Resynchronization Therapy," *J Cardiovasc Transl Res,* vol. 9, no. 4, pp. 257-65, Aug 2016.

[35] S. Ploux *et al.*, "Noninvasive electrocardiographic mapping to improve patient selection for cardiac resynchronization therapy: beyond QRS duration and left bundle branch block morphology," *J Am Coll Cardiol,* vol. 61, no. 24, pp. 2435-2443, Jun 18 2013.

[36] J. De Pooter *et al.*, "Different Methods to Measure QRS Duration in CRT Patients: Impact on the Predictive Value of QRS Duration Parameters," *Ann Noninvasive Electrocardiol,* vol. 21, no. 3, pp. 305-15, May 2016.

[37] M. De Guillebon *et al.*, "Reliability and reproducibility of QRS duration in the selection of candidates for cardiac resynchronization therapy," *J Cardiovasc Electrophysiol,* vol. 21, no. 8, pp. 890-2, Aug 1 2010.
[38] E. Bertaglia *et al.*, "Stricter criteria for left bundle branch block diagnosis do not improve response to CRT," *Pacing Clin Electrophysiol,* vol. 40, no. 7, pp. 850-856, Jul 2017.
[39] K. Emerek *et al.*, "New strict left bundle branch block criteria reflect left ventricular activation differences," *J Electrocardiol,* vol. 48, no. 5, pp. 758-62, Sep-Oct 2015.
[40] L. Galeotti, P. M. van Dam, Z. Loring, D. Chan, and D. G. Strauss, "Evaluating strict and conventional left bundle branch block criteria using electrocardiographic simulations," *Europace,* vol. 15, no. 12, pp. 1816-21, Dec 2013.
[41] E. B. Engels, E. M. Vegh, C. J. Van Deursen, K. Vernooy, J. P. Singh, and F. W. Prinzen, "T-wave area predicts response to cardiac resynchronization therapy in patients with left bundle branch block," *J Cardiovasc Electrophysiol,* vol. 26, no. 2, pp. 176-83, Feb 2015.
[42] R. Eschalier, S. Ploux, P. Ritter, M. Haissaguerre, K. A. Ellenbogen, and P. Bordachar, "Nonspecific intraventricular conduction delay: Definitions, prognosis, and implications for cardiac resynchronization therapy," *Heart Rhythm,* vol. 12, no. 5, pp. 1071-9, May 2015.
[43] K. Vernooy *et al.*, "Calculation of effective VV interval facilitates optimization of AV delay and VV interval in cardiac resynchronization therapy," *Heart Rhythm,* vol. 4, no. 1, pp. 75-82, Jan 2007.
[44] D. Gras, M. S. Gupta, E. Boulogne, L. Guzzo, and W. T. Abraham, "Optimization of AV and VV delays in the real-world CRT patient population: an international survey on current clinical practice," *Pacing Clin Electrophysiol,* vol. 32 Suppl 1, pp. S236-9, Mar 2009.
[45] D. Birnie *et al.*, "Clinical outcomes with synchronized left ventricular pacing: analysis of the adaptive CRT trial," *Heart Rhythm,* vol. 10, no. 9, pp. 1368-74, Sep 2013.
[46] A. R. Bryant, S. B. Wilton, M. P. Lai, and D. V. Exner, "Association between QRS duration and outcome with cardiac resynchronization therapy: a systematic review and meta-analysis," *J Electrocardiol,* vol. 46, no. 2, pp. 147-55, Mar-Apr 2013.
[47] M. R. Gold *et al.*, "Effect of QRS duration and morphology on cardiac resynchronization therapy outcomes in mild heart failure: results from the Resynchronization Reverses Remodeling in Systolic Left Ventricular Dysfunction (REVERSE) study," *Circulation,* vol. 126, no. 7, pp. 822-9, Aug 14 2012.
[48] M. O. Sweeney, R. J. van Bommel, M. J. Schalij, C. J. Borleffs, A. S. Hellkamp, and J. J. Bax, "Analysis of ventricular activation using surface electrocardiography to

predict left ventricular reverse volumetric remodeling during cardiac resynchronization therapy," *Circulation,* vol. 121, no. 5, pp. 626-34, Feb 9 2010.
[49] C. J. van Deursen *et al.*, "The value of the 12-lead ECG for evaluation and optimization of cardiac resynchronization therapy in daily clinical practice," *J Electrocardiol,* vol. 47, no. 2, pp. 202-11, Mar-Apr 2014.
[50] F. Ruschitzka *et al.*, "Cardiac-resynchronization therapy in heart failure with a narrow QRS complex," *N Engl J Med,* vol. 369, no. 15, pp. 1395-405, Oct 10 2013.
[51] H. Hara *et al.*, "The relationship of QRS morphology and mechanical dyssynchrony to long-term outcome following cardiac resynchronization therapy," *Eur Heart J,* vol. 33, no. 21, pp. 2680-91, Nov 2012.
[52] J. Jacobsson *et al.*, "Usefulness of the Sum Absolute QRST Integral to Predict Outcomes in Patients Receiving Cardiac Resynchronization Therapy," *Am J Cardiol,* vol. 118, no. 3, pp. 389-95, Aug 1 2016.
[53] J. DePooter *et al.*, "Biventricular Paced QRS Area Predicts Acute Hemodynamic CRT Response Better Than QRS Duration or QRS Amplitudes," *J Cardiovasc Electrophysiol,* vol. 28, no. 2, pp. 192-200, Feb 2017.
[54] C. J. van Deursen *et al.*, "Vectorcardiography as a tool for easy optimization of cardiac resynchronization therapy in canine left bundle branch block hearts," *Circ Arrhythm Electrophysiol,* vol. 5, no. 3, pp. 544-52, Jun 1 2012.
[55] C. J. van Deursen *et al.*, "Vectorcardiographic QRS area as a novel predictor of response to cardiac resynchronization therapy," *J Electrocardiol,* vol. 48, no. 1, pp. 45-52, Jan-Feb 2015.
[56] C. J. van Deursen *et al.*, "Vectorcardiography for optimization of stimulation intervals in cardiac resynchronization therapy," *J Cardiovasc Transl Res,* vol. 8, no. 2, pp. 128-37, Mar 2015.
[57] K. Ikeda, I. Kubota, I. Tonooka, K. Tsuiki, and S. Yasui, "Detection of posterior myocardial infarction by body surface mapping: a comparative study with 12 lead ECG and VCG," *J Electrocardiol,* vol. 18, no. 4, pp. 361-9, Oct 1985.
[58] R. T. van Dam, P. C. Roose, P. Arnaud, and C. Brohet, "The diagnostic performance of visual examination of BSM and of ECG/VCG in the identification of chronically infarcted left ventricular segments," in *International Symposium on Body Surface Mapping*, 2012.
[59] R. A. Douglas, N. Samesima, M. M. Filho, A. A. Pedrosa, S. A. Nishioka, and C. A. Pastore, "Global and regional ventricular repolarization study by body surface potential mapping in patients with left bundle-branch block and heart failure undergoing cardiac resynchronization therapy," *Ann Noninvasive Electrocardiol,* vol. 17, no. 2, pp. 123-9, Apr 2012.
[60] M. S. Guilem, R. Brugada, B. Thibault, A. M. Climent, and J. Millet, "Analysis of body surface potential maps in cardiac resynchronization therapy," *Computers in Cardiology,* vol. 35, pp. 93-96, 2008.

[61] R. M. Gage, A. E. Curtin, K. V. Burns, S. Ghosh, J. M. Gillberg, and A. J. Bank, "Changes in electrical dyssynchrony by body surface mapping predict left ventricular remodeling in patients with cardiac resynchronization therapy," *Heart Rhythm,* vol. 14, no. 3, March 2017.

[62] W. B. Johnson *et al.*, "Body surface mapping using an ECG belt to characterize electrical heterogeneity for different left ventricular pacing sites during cardiac resynchronization: Relationship with acute hemodynamic improvement," *Heart Rhythm,* vol. 14, no. 3, Mar 2017.

[63] C. Ramanathan, R. N. Ghanem, P. Jia, K. Ryu, and Y. Rudy, "Noninvasive electrocardiographic imaging for cardiac electrophysiology and arrhythmia," *Nat Med,* vol. 10, no. 4, pp. 422-8, Apr 2004.

[64] P. Jia, C. Ramanathan, R. N. Ghanem, K. Ryu, N. Varma, and Y. Rudy, "Electrocardiographic imaging of cardiac resynchronization therapy in heart failure: observation of variable electrophysiologic responses," *Heart Rhythm,* vol. 3, no. 3, pp. 296-310, Mar 2006.

[65] S. Ghosh *et al.*, "Early repolarization associated with sudden death: insights from noninvasive electrocardiographic imaging," *Heart Rhythm,* vol. 7, no. 4, pp. 534-7, Apr 2010.

[66] M. Medvegy, G. Duray, A. Pinter, and I. Preda, "Body surface potential mapping: historical background, present possibilities, diagnostic challenges," *Ann Noninvasive Electrocardiol,* vol. 7, no. 2, pp. 139-51, Apr 2002.

[67] C. A. Pastore *et al.*, "Body surface potential mapping investigating the ventricular activation patterns in the cardiac resynchronization of patients with left bundle-branch block and heart failure," *J Electrocardiol,* vol. 39, no. 1, pp. 93-102, Jan 2006.

[68] N. Samesima, C. A. Pastore, R. A. Douglas, M. F. Martinelli, and A. A. Pedrosa, "Improved relationship between left and right ventricular electrical activation after cardiac resynchronization therapy in heart failure patients can be quantified by body surface potential mapping," *Clinics (Sao Paulo),* vol. 68, no. 7, pp. 986-91, Jul 2013.

[69] M. P. Nash, C. P. Bradley, and D. J. Paterson, "Imaging electrocardiographic dispersion of depolarization and repolarization during ischemia: simultaneous body surface and epicardial mapping," *Circulation,* vol. 107, no. 17, pp. 2257-63, May 6 2003.

[70] M. Akahoshi *et al.*, "Body-surface distribution of changes in activation-recovery intervals before and after catheter ablation in patients with Wolff-Parkinson-White syndrome: clinical evidence for ventricular 'electrical remodeling' with prolongation of action-potential duration over a preexcited area," *Circulation,* vol. 96, no. 5, pp. 1566-74, Sep 2 1997.

[71] L. Eckardt and G. Breithardt, "Construction and interpretation of endocardial maps from basic electrophysiology to 3D mapping," in *Cardiac Mapping*, M. H.

Shenasa, G; Borggrefe, M; and Breithardt, G, Ed. 3rd ed.: Blackwell Publishing, 2009, pp. 13-26.
[72] N. Varma, S. Ploux, P. Ritter, B. Wilkoff, R. Eschalier, and P. Bordachar, "Noninvasive mapping of electrical dyssynchrony in heart failure and cardiac resynchronization therapy," *Card Electrophysiol Clin,* vol. 7, no. 1, pp. 125-34, Mar 2015.
[73] A. J. McClelland, C. G. Owens, I. B. Menown, M. Lown, and A. A. Adgey, "Comparison of the 80-lead body surface map to physician and to 12-lead electrocardiogram in detection of acute myocardial infarction," *Am J Cardiol,* vol. 92, no. 3, pp. 252-7, Aug 1 2003.
[74] J. P. Ornato *et al.*, "Body surface mapping vs 12-lead electrocardiography to detect ST-elevation myocardial infarction," *Am J Emerg Med,* vol. 27, no. 7, pp. 779-84, Sep 2009.
[75] B. J. O'Neil *et al.*, "Incremental benefit of 80-lead electrocardiogram body surface mapping over the 12-lead electrocardiogram in the detection of acute coronary syndromes in patients without ST-elevation myocardial infarction: Results from the Optimal Cardiovascular Diagnostic Evaluation Enabling Faster Treatment of Myocardial Infarction (OCCULT MI) trial," *Acad Emerg Med,* vol. 17, no. 9, pp. 932-9, Sep 2010.
[76] R. J. Oweis and B. Al-Tabbaa, "QRS detection and heart rate variability analysis: A survey," *Biomedical Science and Engineering,* vol. 2, no. 1, pp. 13-14, 2014.
[77] M. Potse, A. C. Linnenbank, and C. A. Grimbergen, "Software design for analysis of multichannel intracardial and body surface electrocardiograms," *Comput Methods Programs Biomed,* vol. 69, no. 3, pp. 225-36, Nov 2002.
[78] J. G. Kemmelings, A. C. Linnenbank, S. L. Muilwijk, A. SippensGroenewegen, A. Peper, and C. A. Grimbergen, "Automatic QRS onset and offset detection for body surface QRS integral mapping of ventricular tachycardia," *IEEE Trans Biomed Eng,* vol. 41, no. 9, pp. 830-6, Sep 1994.
[79] N. M. Arzeno, Z. D. Deng, and C. S. Poon, "Analysis of first-derivative based QRS detection algorithms," *IEEE Trans Biomed Eng,* vol. 55, no. 2 Pt 1, pp. 478-84, Feb 2008.
[80] E. J. Luz, W. R. Schwartz, G. Camara-Chavez, and D. Menotti, "ECG-based heartbeat classification for arrhythmia detection: A survey," *Comput Methods Programs Biomed,* vol. 127, pp. 144-64, Apr 2016.
[81] M. O. Sweeney, A. S. Hellkamp, R. J. van Bommel, M. J. Schalij, C. J. Borleffs, and J. J. Bax, "QRS fusion complex analysis using wave interference to predict reverse remodeling during cardiac resynchronization therapy," *Heart Rhythm,* vol. 11, no. 5, pp. 806-13, May 2014.
[82] C. Cuspidi *et al.*, "Does QRS Voltage Correction by Body Mass Index Improve the Accuracy of Electrocardiography in Detecting Left Ventricular Hypertrophy and

Predicting Cardiovascular Events in a General Population?," *The Journal of Clinical Hypertension,* vol. 18, no. 5, pp. 415-421, 2016.

[83] S. Kurisu *et al.*, "Electrocardiographic characterisitcs in the underweight and obese in accordance with the World Health Organization classification," *IJC Metabolic & Endocrine,* vol. 9, pp. 61-65, 2015.

[84] A. E. Curtin, A. J. Bank, R. M. Gage, and K. V. Burns, "Anterior and posterior electrode signals," 2017.

[85] P. Kligfield *et al.*, "Recommendations for the standardization and interpretation of the electrocardiogram: part I: the electrocardiogram and its technology a scientific statement from the American Heart Association Electrocardiography and Arrhythmias Committee, Council on Clinical Cardiology; the American College of Cardiology Foundation; and the Heart Rhythm Society endorsed by the International Society for Computerized Electrocardiology," *J Am Coll Cardiol,* vol. 49, no. 10, pp. 1109-27, Mar 13 2007.

[86] J. M. Aranda *et al.*, "QRS duration variability in patients with heart failure," *Am J Cardiol,* vol. 90, no. 3, pp. 335-7, Aug 1 2002.

[87] B. U. Kohler, C. Hennig, and R. Orglmeister, "The principles of software QRS detection," (in English), *Ieee Engineering in Medicine and Biology Magazine,* Review vol. 21, no. 1, pp. 42-57, Jan-Feb 2002.

[88] S. G. Carruthers, B. McCall, B. A. Cordell, and R. Wu, "Relationships between heart rate and PR interval during physiological and pharmacological interventions," *British Journal of Clinical Pharmacology,* vol. 23, no. 3, pp. 259-265, 1987.

[89] J. Karjalainen, M. Viitasalo, M. Mänttäri, and V. Manninen, "Relation between QT intervals and heart rates from 40 to 120 beats/min in rest electrocardiograms of men and a simple method to adjust QT interval values," *Journal of the American College of Cardiology,* vol. 23, no. 7, pp. 1547-1553, 1994/06/01/ 1994.

[90] *Recommended practice for testing and reporting performance results of ventricular arrhythmia detection algorithms.* , 1987.

[91] B. Surawicz *et al.*, "AHA/ACCF/HRS recommendations for the standardization and interpretation of the electrocardiogram: part III: intraventricular conduction disturbances: a scientific statement from the American Heart Association Electrocardiography and Arrhythmias Committee, Council on Clinical Cardiology; the American College of Cardiology Foundation; and the Heart Rhythm Society. Endorsed by the International Society for Computerized Electrocardiology," *J Am Coll Cardiol,* vol. 53, no. 11, pp. 976-81, Mar 17 2009.

[92] M. Cesari, J. Mehlsen, A. B. Mehlsen, and H. B. D. Sorensen, "A New Wavelet-Based ECG Delineator for the Evaluation of the Ventricular Innervation," *IEEE J Transl Eng Health Med,* vol. 5, p. 2000215, 2017.

[93] J. De Pooter, M. El Haddad, R. Stroobandt, M. De Buyzere, and F. Timmermans, "Accuracy of computer-calculated and manual QRS duration assessments:

Clinical implications to select candidates for cardiac resynchronization therapy," *Int J Cardiol,* vol. 236, pp. 276-282, Jun 1 2017.

[94] A. J. Bank, R. M. Gage, A. E. Curtin, K. V. Burns, J. M. Gillberg, and S. Ghosh, "Body surface activation mapping of electrical dyssynchrony in cardiac resynchronization therapy patients: Potential for optimization," *Journal of Electrocardiology,* vol. Accepted for Publication, 2017.

[95] P. Kligfield *et al.*, "Recommendations for the standardization and interpretation of the electrocardiogram: part I: The electrocardiogram and its technology: a scientific statement from the American Heart Association Electrocardiography and Arrhythmias Committee, Council on Clinical Cardiology; the American College of Cardiology Foundation; and the Heart Rhythm Society: endorsed by the International Society for Computerized Electrocardiology," *Circulation,* vol. 115, no. 10, pp. 1306-24, Mar 13 2007.

[96] A. E. Curtin, K. V. Burns, A. J. Bank, and T. I. Netoff, "QRS complex detection and measurement algorithms for multichannel ECGs in cardiac resynchronization therapy patients," *IEEE Journal of Translational Engineering in Health and Medicine,* vol. Submitted, 2018.

[97] C. Fantoni *et al.*, "Cardiac resynchronization therapy improves heart rate profile and heart rate variability of patients with moderate to severe heart failure," *J Am Coll Cardiol,* vol. 46, no. 10, pp. 1875-82, Nov 15 2005.

[98] I. Sipinkova, G. Hahn, M. Meyer, M. Tadlanek, and J. Hajek, "Effect of respiration and posture on heart rate variability," *Physiol Res,* vol. 46, no. 3, pp. 173-9, 1997.

[99] W. Zareba *et al.*, "Effectiveness of Cardiac Resynchronization Therapy by QRS Morphology in the Multicenter Automatic Defibrillator Implantation Trial-Cardiac Resynchronization Therapy (MADIT-CRT)," *Circulation,* vol. 123, no. 10, pp. 1061-72, Mar 15 2011.

[100] D. G. Strauss *et al.*, "ECG quantification of myocardial scar in cardiomyopathy patients with or without conduction defects: correlation with cardiac magnetic resonance and arrhythmogenesis," *Circ Arrhythm Electrophysiol,* vol. 1, no. 5, pp. 327-36, Dec 2008.

[101] A. J. Bank, A. E. Curtin, R. M. Gage, and K. V. Burns, "Anterior and posterior electrode signals," 2017.

[102] S. Ghosh *et al.*, "Electrophysiologic substrate and intraventricular left ventricular dyssynchrony in nonischemic heart failure patients undergoing cardiac resynchronization therapy," *Heart Rhythm,* vol. 8, no. 5, pp. 692-9, May 2011.

[103] N. Varma, P. Jia, and Y. Rudy, "Electrocardiographic imaging of patients with heart failure with left bundle branch block and response to cardiac resynchronization therapy," *J Electrocardiol,* vol. 40, no. 6 Suppl, pp. S174-8, Nov-Dec 2007.

[104] D. D. Chan *et al.*, "Comparison of the relation between left ventricular anatomy and QRS duration in patients with cardiomyopathy with versus without left bundle branch block," *Am J Cardiol,* vol. 113, no. 10, pp. 1717-22, May 15 2014.
[105] A. E. Curtin, K. V. Burns, R. M. Gage, and A. J. Bank, "Left ventricular orientation and position in an advanced heart failure population," *Translational Research in Anatomy,* vol. 7, pp. 12-19, 2017.
[106] M. R. Gold *et al.*, "The relationship between ventricular electrical delay and left ventricular remodelling with cardiac resynchronization therapy," *Eur Heart J,* vol. 32, no. 20, pp. 2516-24, Oct 2011.
[107] M. Strik *et al.*, "Transseptal conduction as an important determinant for cardiac resynchronization therapy, as revealed by extensive electrical mapping in the dyssynchronous canine heart," *Circ Arrhythm Electrophysiol,* vol. 6, no. 4, pp. 682-9, Aug 2013.
[108] N. B. Schiller *et al.*, "Left ventricular volume from paired biplane two-dimensional echocardiography," *Circulation,* vol. 60, no. 3, pp. 547-55, Sep 1979.
[109] J. van 't Sant *et al.*, "Echo response and clinical outcome in CRT patients," *Neth Heart J,* vol. 24, no. 1, pp. 47-55, Jan 2016.
[110] C. Ypenburg *et al.*, "Long-term prognosis after cardiac resynchronization therapy is related to the extent of left ventricular reverse remodeling at midterm follow-up," *J Am Coll Cardiol,* vol. 53, no. 6, pp. 483-90, Feb 10 2009.
[111] G. B. Bleeker *et al.*, "Clinical versus echocardiographic parameters to assess response to cardiac resynchronization therapy," *Am J Cardiol,* vol. 97, no. 2, pp. 260-3, Jan 15 2006.
[112] B. Herweg *et al.*, "Site-specific differences in latency intervals during biventricular pacing: impact on paced QRS morphology and echo-optimized V-V interval," *Pacing Clin Electrophysiol,* vol. 33, no. 11, pp. 1382-91, Nov 2010.
[113] J. Rickard *et al.*, "Predictors of response to cardiac resynchronization therapy: A systematic review," *Int J Cardiol,* vol. 225, pp. 345-352, Dec 15 2016.
[114] L. Liu, M. Ji, and M. Buchroithner, "Combining Partial Least Squares and the Gradient-Boosting Method for Soil Property Retrieval Using Visible Near-Infrared Shortwave Infrared Spectra," *Remoted Sensing,* vol. 9, 2017 2017.
[115] P. K. Kreeger, "Using partial least squares regression to analyze cellular response data," *Science Signaling,* vol. 6, no. 271, 2013 2013.
[116] H. Bar-Gera, "The target parameter of adjusted r-squared in fixed-design experiments," *The American Statistician,* vol. 17, no. 2, pp. 112-119, 2017.
[117] A. Barsheshet *et al.*, "Response to preventive cardiac resynchronization therapy in patients with ischaemic and nonischaemic cardiomyopathy in MADIT-CRT," *Eur Heart J,* vol. 32, no. 13, pp. 1622-30, Jul 2011.
[118] M. Y. Park *et al.*, "Characteristics of responders to cardiac resynchronization therapy: the impact of echocardiographic left ventricular volume," *Clin Cardiol,* vol. 35, no. 12, pp. 777-80, Dec 2012.

[119] B. J. Schijvenaars, G. van Herpen, and J. A. Kors, "Intraindividual variability in electrocardiograms," *J Electrocardiol,* vol. 41, no. 3, pp. 190-6, May-Jun 2008.
[120] C. Ramanathan and Y. Rudy, "Electrocardiographic imaging: I. Effect of torso inhomogeneities on body surface electrocardiographic potentials," *J Cardiovasc Electrophysiol,* vol. 12, no. 2, pp. 229-40, Feb 2001.
[121] L. S. Green, R. L. Lux, C. W. Haws, R. R. Williams, S. C. Hunt, and M. J. Burgess, "Effects of age, sex, and body habitus on QRS and ST-T potential maps of 1100 normal subjects," *Circulation,* vol. 71, no. 2, pp. 244-53, Feb 1985.
[122] R. S. MacLeod, Q. Ni, B. Punske, P. R. Ershler, B. Yilmaz, and B. Taccardi, "Effects of heart position on the body-surface electrocardiogram," *J Electrocardiol,* vol. 33 Suppl, pp. 229-37, 2000.
[123] R. Hoekema, G. J. Uijen, and A. van Oosterom, "Geometrical aspects of the interindividual variability of multilead ECG recordings," *IEEE Trans Biomed Eng,* vol. 48, no. 5, pp. 551-9, May 2001.
[124] R. Hoekema, G. J. Uijen, L. van Erning, and A. van Oosterom, "Interindividual variability of multilead electrocardiographic recordings: influence of heart position," *J Electrocardiol,* vol. 32, no. 2, pp. 137-48, Apr 1999.
[125] U. C. Nguyen *et al.*, "An in-silico analysis of the effect of heart position and orientation on the ECG morphology and vectorcardiogram parameters in patients with heart failure and intraventricular conduction defects," *J Electrocardiol,* vol. 48, no. 4, pp. 617-25, Jul-Aug 2015.
[126] J. D. Dougherty, "The relation of QRS amplitude to the frontal QRS axis and the heart-electrode distance," *J Electrocardiol,* vol. 4, no. 3, pp. 249-60, 1971.
[127] H. Engblom, E. Hedstrom, J. Palmer, G. S. Wagner, and H. Arheden, "Determination of the left ventricular long-axis orientation from a single short-axis MR image: relation to BMI and age," *Clin Physiol Funct Imaging,* vol. 24, no. 5, pp. 310-5, Sep 2004.
[128] G. Sathananthan *et al.*, "Computed tomography-guided in vivo cardiac orientation and correlation with ECG in individuals without structural heart disease and in age-matched obese and older individuals," *Clin Anat,* vol. 28, no. 4, pp. 487-93, May 2015.
[129] G. Z. Sathananthan, S; Aggarwal, G; Chik, W; Friedman, D; Thiagalingam A, "Cardiac orientation: is there a correlation between the anatomical and the electrical axis of the heart?," *Br J Cardiol,* vol. 22, no. 2, April 2015 2015.
[130] J. E. Foster *et al.*, "Determination of left ventricular long-axis orientation using MRI: changes during the respiratory and cardiac cycles in normal and diseased subjects," *Clin Physiol Funct Imaging,* vol. 25, no. 5, pp. 286-92, Sep 2005.
[131] Z. Loring, W. Zareba, S. McNitt, D. G. Strauss, G. S. Wagner, and J. P. Daubert, "ECG quantification of myocardial scar and risk stratification in MADIT-II," *Ann Noninvasive Electrocardiol,* vol. 18, no. 5, pp. 427-35, Sep 2013.

[132] J. J. McMurray *et al.*, "ESC guidelines for the diagnosis and treatment of acute and chronic heart failure 2012: The Task Force for the Diagnosis and Treatment of Acute and Chronic Heart Failure 2012 of the European Society of Cardiology. Developed in collaboration with the Heart Failure Association (HFA) of the ESC," *Eur J Heart Fail,* vol. 14, no. 8, pp. 803-69, Aug 2012.
[133] A. Kashani and S. S. Barold, "Significance of QRS complex duration in patients with heart failure," *J Am Coll Cardiol,* vol. 46, no. 12, pp. 2183-92, Dec 20 2005.
[134] J. W. Weinsaft, J. D. Kochav, A. Afroz, and P. M. Okin, "Q wave area for stratification of global left ventricular infarct size: comparison to conventional ECG assessment using Selvester QRS-score," *Coron Artery Dis,* vol. 25, no. 2, pp. 138-44, Mar 2014.
[135] M. M. Balci *et al.*, "Usefulness of notched duration to predict response to cardiac resynchronization therapy," *Scand Cardiovasc J,* vol. 49, no. 4, pp. 200-6, Aug 2015.
[136] A. Brenyo *et al.*, "QRS axis and the benefit of cardiac resynchronization therapy in patients with mildly symptomatic heart failure enrolled in MADIT-CRT," *J Cardiovasc Electrophysiol,* vol. 24, no. 4, pp. 442-8, Apr 2013.
[137] K. Dickstein *et al.*, "2010 Focused Update of ESC Guidelines on device therapy in heart failure: an update of the 2008 ESC Guidelines for the diagnosis and treatment of acute and chronic heart failure and the 2007 ESC Guidelines for cardiac and resynchronization therapy. Developed with the special contribution of the Heart Failure Association and the European Heart Rhythm Association," *Europace,* vol. 12, no. 11, pp. 1526-36, Nov 2010.
[138] J. D. Dougherty, "The relation of the frontal QRS axis to the anatomic position of the heart," *J Electrocardiol,* vol. 3, no. 3-4, pp. 267-84, 1970.
[139] J. D. Dougherty and H. W. Stoudt, "The relation of frontal QRS axis to age and body build," *J Electrocardiol,* vol. 3, no. 3-4, pp. 285-98, 1970.
[140] C. A. Schneider, W. S. Rasband, and K. W. Eliceiri, "NIH Image to ImageJ: 25 years of image analysis," *Nat Methods,* vol. 9, no. 7, pp. 671-5, Jul 2012.
[141] J. J. McMurray *et al.*, "ESC Guidelines for the diagnosis and treatment of acute and chronic heart failure 2012: The Task Force for the Diagnosis and Treatment of Acute and Chronic Heart Failure 2012 of the European Society of Cardiology. Developed in collaboration with the Heart Failure Association (HFA) of the ESC," *Eur Heart J,* vol. 33, no. 14, pp. 1787-847, Jul 2012.
[142] L. P. Laurin, V. Jobin, and F. Bellemare, "Sternum length and rib cage dimensions compared with bodily proportions in adults with cystic fibrosis," *Can Respir J,* vol. 19, no. 3, pp. 196-200, May-Jun 2012.
[143] M. Henneberg and S. J. Ulijaszek, "Body frame dimensions are related to obesity and fatness: Lean trunk size, skinfolds, and body mass index," *Am J Hum Biol,* vol. 22, no. 1, pp. 83-91, Jan-Feb 2010.

[144] S. Meek and F. Morris, "ABC of clinical electrocardiography.Introduction. I-Leads, rate, rhythm, and cardiac axis," *BMJ,* vol. 324, no. 7334, pp. 415-8, Feb 16 2002.
[145] J. D. Kochav, P. M. Okin, S. Wilson, A. Afroz, A. Renilla, and J. W. Weinsaft, "Usefulness of Q-wave area for threshold-based stratification of global left ventricular myocardial infarct size," *Am J Cardiol,* vol. 112, no. 2, pp. 174-80, Jul 15 2013.
[146] E. B. Engels, M. Mafi-Rad, A. M. van Stipdonk, K. Vernooy, and F. W. Prinzen, "Why QRS Duration Should Be Replaced by Better Measures of Electrical Activation to Improve Patient Selection for Cardiac Resynchronization Therapy," *J Cardiovasc Transl Res,* May 26 2016.
[147] R. G. Charles, "Cardiac resynchronization therapy: when and for whom?," *European Heart Journal Supplements,* vol. 4, no. Supplement D, p. 5, 2004.
[148] C. M. Lucas, G. V. Cleuren, and C. J. Kirchhof, "Selection of patients for cardiac resynchronisation therapy (CRT) in an unselected heart failure population," *Neth Heart J,* vol. 14, no. 1, pp. 14-18, Jan 2006.
[149] F. Z. Khan *et al.*, "Targeted left ventricular lead placement to guide cardiac resynchronization therapy: the TARGET study: a randomized, controlled trial," *J Am Coll Cardiol,* vol. 59, no. 17, pp. 1509-18, Apr 24 2012.
[150] A. Keys, F. Fidanza, M. J. Karvonen, N. Kimura, and H. L. Taylor, "Indices of relative weight and obesity," *J Chronic Dis,* vol. 25, no. 6, pp. 329-43, Jul 1 1972.
[151] D. L. Hayes *et al.*, "Cardiac resynchronization therapy and the relationship of percent biventricular pacing to symptoms and survival," *Heart Rhythm,* vol. 8, no. 9, pp. 1469-75, Sep 2011.